UNIVERSITY OF COPENHAGEN
FACULTY OF SCIENCE

DMI
Danish Meteorological Institute

Ph.D. thesis

Rasmus Anker Pedersen

Modelling interglacial climate

Investigating the mechanisms of a warming climate

Academic advisors:

Bo M. Vinther, Associate Professor
Centre for Ice and Climate, Niels Bohr Institute, Uni. Copenhagen

Peter L. Langen, Climate Scientist
Climate and Arctic Research, Danish Meteorological Institute

Submitted 17 May 2016

Preface

Ph.D. Thesis
Faculty of Science, University of Copenhagen

Author	Rasmus Anker Pedersen
E-mail	anker@nbi.ku.dk
Institutions	Centre for Ice and Climate, Niels Bohr Institute, University of Copenhagen Climate and Arctic Research, Danish Meteorological Institute
Supervisors	Bo M. Vinther, Centre for Ice and Climate, Niels Bohr Institute Peter L. Langen, Climate and Arctic Research, Danish Meteorological Institute

Rasmus Anker Pedersen

Acknowledgments

This thesis marks the end of three years of research carried out mainly in Copenhagen with two stays abroad in California and in Paris. Due to the shared funding of the project, my time in Copenhagen has been divided between the Centre for Ice and Climate at Uni. Copenhagen and the Climate and Arctic Research department (formerly the Danish Climate Center) at the Danish Meteorological Institute – conveniently only separated by a short bike ride.

The joint supervision I have had from Bo and Peter has made all the difference for this project. As advisers, collaborators and mentors alike they have had a crucial influence on the progress of this project and my development as a scientist. I am grateful for and impressed with their commitment to and interest in the project; their doors were always open and they have always made my work a priority.

A modelling project like this one will inevitably involve technical challenges. I owe my gratitude to Shuting Yang (DMI) for valuable support on EC-Earth, which was very important for my progress in the early part of the project. Similarly, I want to thank Qiong Zhang and Qiang Li from Stockholm University for their support and collaboration on EC-Earth paleomodelling.

My time at Stanford was very productive and ultimately resulted in my first publication. Ivana Cvijanovic deserves a lot of credit for this successful side-project; for inviting me to California and for her huge effort as combined collaborator and stand-in-supervisor. I also want to thank Ken Caldeira for inspiring discussions and for welcoming me as part of the group at DGE.

I had a second very productive stay abroad in Paris at LSCE. I want to express my gratitude to Valérie Masson-Delmotte for inviting me, introducing me to the entire department, and for taking the time out of her busy schedule to discuss my project. The inspiring discussions resulted in a long list of research ideas for me to pursue. I want to thank Aline Govin for helpful discussion on paleoclimate modelling and proxy records.

It has been a big asset for me to be a part of the two groups at DMI and Uni. Copenhagen. Especially, I want to highlight the ice2ice project which I have really appreciated being a part of. I am thankful to Bo and Jens Hesselbjerg Christensen for inviting me to take part in the meetings, discussions, and workshops.

Contents

Abstract

Past warm climate states could potentially provide information on future global warming. The past warming was driven by changed insolation rather than an increased greenhouse effect, and thus the warm climate states are expected to be different. Nonetheless, the response of the climate system involves some of the same mechanisms regardless of the source of the initial warming. This thesis aims to investigate these mechanisms through general circulation model experiments. This two-part study has a special focus on the Arctic region, and the main paleoclimate modelling experiments are supplemented by idealized experiments detailing the impact of a changing sea ice cover.

The first part focusses on the last interglacial climate (125,000 years before present) which was characterized by substantial warming at high northern latitudes due to an increased insolation during summer. The impact of the insolation changes is analyzed using an equilibrium simulation with the EC-Earth coupled climate model in high spatial resolution. Additional atmosphere-only simulations are used to separate the direct impact from the changed insolation from the secondary contribution from the related oceanic changes (i.e. sea ice and sea surface temperature changes). These simulations are forced with a combination of last interglacial sea surface temperatures and sea ice conditions and pre-industrial insolation, and vice versa.

The coupled simulation yields an annual mean global warming of approximately 0.5°C compared to pre-industrial conditions. The Arctic region shows a warming of more than 2°C in all seasons. The hybrid simulations reveal that the oceanic changes dominate the response at high northern latitudes, including the North Atlantic region and Europe, while the direct insolation impact is more dominant in the tropics. On Greenland, the simulated precipitation-weighted warming of 2.4°C at the NEEM ice core site is low compared to the ice core reconstruction, partially due to missing feedbacks related to ice sheet changes. Surface mass balance calculations with an energy balance model indicate that the oceanic conditions favor increased accumulation in the southeast, while the insolation appears to be the dominant cause of the expected ice sheet reduction.

The second part explores the atmospheric sensitivity to the location of sea ice loss using a general circulation model in a configuration that allows combination of a prescribed sea ice cover and an active mixed layer ocean. Three investigated sea ice scenarios with ice loss in different regions all exhibit substantial near-surface warming, with maximum warming occurring in winter. The three scenarios all affect the climate beyond the Arctic, especially the mid-latitude circulation which is sensitive to the location of the ice loss. The mean zonal wind and the North Atlantic Oscillation reveal a high sensitivity to the location of the ice loss.

Together, the results presented in this thesis illustrate that the changes in the Arctic sea ice cover are important for shaping both past and future warm climate states. Nonetheless, the last interglacial is not an ideal analogue for future climate changes, as the changed insolation has a large impact – especially on the Greenland ice sheet.

Resumé

Fortidens varme klimastadier kan potentielt gøre os klogere på fremtidens globale opvarmning. De historiske klimaændringer blev dog drevet af ændringer i solindstrålingen fremfor af drivhuseffekten, og fortidens og fremtidens varme klimaer er derfor ikke fuldstændigt sammenlignelige. Alligevel involverer de to typer klimaændringer nogle af de samme mekanismer, der igangsættes når klimaet opvarmes. Denne afhandling undersøger disse mekanismer baseret på klimamodelberegninger med generelle cirkulationsmodeller. Afhandlingen er et todelt studie med særligt fokus på Arktis. Den er baseret på paleoklima-eksperimenter suppleret med idealiserede eksperimenter, der undersøger effekten af ændringer i den Arktiske havis.

Den første del fokuserer på den seneste mellem-istid (Eem-tiden, for 125.000 år siden), der var karakteriseret af markant opvarmning i Arktis som konsekvens af øget solindstråling om sommeren. Effekten af den ændrede solindstråling analyseres gennem et højopløst, ligevægts-eksperiment med modellen EC-Earth. Yderligere eksperimenter med atmosfærekomponenten fra modellen bruges til at adskille den direkte effekt af solindstrålingen og den efterfølgende indirekte effekt fra havistab og opvarmning af havoverfladen. Adskillelsen opnås ved hjælp af hybrid-eksperimenter hvor klimaet forceres med en kombination af enten Eem-tidens havtemperaturer og havisdække og præ-industriel solindstråling eller de omvendte betingelser.

Eksperimenterne med den fulde model opnår en gennemsnitlig global opvarmning på ca. 0.5°C sammenlignet med det præ-industrielle kontrolklima. Arktis opvarmes med mere end 2°C hele året rundt. Hybrid-eksperimenterne indikerer at havforholdene (havis og havtemperaturer) dominerer ændringerne på høje breddegrader inklusive den Nordatlantiske region og Europa, mens solindstråling er vigtigere for ændringerne i troperne. På Grønland viser beregningerne en nedbørsvægtet opvarmning på 2.4°C ved NEEM iskerneboringen, hvilket er markant lavere end den rekonstruerede temperatur baseret på iskernedata. Beregninger af overflademassebalancen på Indlandsisen viser at de ændrede havforhold fører til øget akkumulation i sydøst, hvorimod solindstråling er den dominerende årsag øget afsmeltning.

Anden del undersøger atmosfærens respons til havistab i forskellige områder af Arktis. Undersøgelsen baseres på en atmosfærisk cirkulationsmodel i en idealiseret opsætning med fastlåst havisdække og en aktiv overfladelags-havmodel ("slab ocean"). Tre forskellige havistab-scenarier med havistab i forskellige dele af Arktis opnår alle sammen en markant overfladebaseret opvarmning, der er stærkest om vinteren. De tre scenarier påvirker alle klimaet udenfor Arktis, især over mellembreddegraderne hvor vejrsystemerne ændres forskelligt afhængig af havisens placering. Forsøgene viser at både den zonale vind og den nordatlantiske oscillation er følsomme overfor havistabets placering.

Tilsammen viser resultaterne i denne afhandling at den Arktiske havis er afgørende for både fortidens og fremtidens klimaændringer. Eem-tiden er dog ikke nogen ideel parallel til fremtidens varme klima på grund af solindstrålingens markante indflydelse på klimaet – specielt på Grønlands indlandsis.

1 Introduction and outline

This Ph.D. project aims to investigate the mechanisms in a warming climate. The expected warming impact from continued greenhouse gas emissions clearly motivates research that can improve our understanding of the climate system and lead to better projections of the future climate. One key question is whether we can learn anything from past warm climate states? These warm climate states were forced by changed insolation rather than an increased greenhouse effect; but perhaps some mechanisms are similar regardless of how the climate is warming. Using general circulation models as the main tool, this project will investigate the last interglacial and assess the processes leading to the warm climate state. A series of experiments has been designed to reveal which changes relate directly to the insolation change, and which that are rather responding to a general ambient warming. Although the last interglacial may not be an ideal future climate analogue, the analyses in this project will reveal which changes that could be relevant for a future climate. Both the last interglacial and projections of future climate exhibit substantial warming at high northern latitudes. Hence, this area is of particular interest and will be the main focus of this thesis. The paleoclimate simulations are supplemented by another suite of experiments designed to investigate a key element in both past, present, and future Arctic warming: the sea ice. The sea ice cover is obviously sensitive to warming, but how does a waning sea ice cover further impact the climate?

This thesis is a two-part study based on three journal articles: two analyzing the last interglacial climate and one investigating the impact of a changing Arctic sea ice cover. The first chapter is a scientific introduction presenting background information on paleoclimate, the last interglacial, the Arctic sea ice, and the climate models used in this project. The following three chapters are based on the three journal articles. Chapters 3 and 4 describe the simulated last interglacial climate. The first paper (Chapter 3) presents the global changes and the key mechanisms, while the second (Chapter 4) focuses on the Greenland ice sheet and comparison to ice core reconstructions. The third paper is presented in Chapter 5 which investigates the atmospheric response to reduction of the Arctic sea ice cover; in particular the sensitivity to the location of the sea ice loss. The full ensemble of model experiments is compared in Chapter 6 which highlights how the climate system responds to the different types of forcing: orbital insolation changes, sea ice loss, and CO_2 increase. The findings are summarized in Chapter 7 which presents an outlook and the final conclusion.

2 Scientific introduction

This chapter will introduce the scientific background for the research in this project. The following sections describe existing research in paleoclimate, climate modelling, and Arctic climate; especially related to sea ice. Details on the climate models employed in this project are presented in Section 2.3.

2.1 Paleoclimate and the last interglacial

2.1.1 Orbital forcing and glacial cycles

The climate of the past million years has been characterized by climatic shifts between glacial and interglacial conditions. Milankovitch theory proposes that variations in the Earth's orbit and the consequent changes in insolation is pacing the glacial-interglacial cycles. Especially the summertime insolation at high northern latitudes is believed to be important for build-up and retreat of continental ice sheets (*Hays et al.*, 1976; *Weertman*, 1976). The insolation changes are not sufficient to cause the substantial climatic changes, but the initial radiative forcing is amplified by climate feedbacks. At high latitudes, cryospheric changes (i.e. reduction of snow cover, sea ice and ice sheets) are key processes in amplifying the insolation driven warming, while several other feedback processes further promote high latitude warming; especially in the Arctic region (*Masson-Delmotte et al.*, 2006; *Miller et al.*, 2010; *Serreze and Barry*, 2011, and Section 2.2).

The orbital configuration impacts the seasonal and spatial distribution of incoming solar radiation. While the total annual insolation only exhibits minor variations, these changes still have a substantial impact on the climate. The changes in insolation arise from variations in the Earth's orbit which exhibits periodical changes in eccentricity, precession, and obliquity (*Berger*, 1978). The obliquity varies approximately between 22–25° axial tilt with a timescale of 41 thousand years (ka). The precession, i.e. the relative angle between perihelion and the vernal equinox, changes with a timescale of 21 ka. The eccentricity varies with several characteristic periods resulting in a dominant 100 ka signal in the insolation (*Crucifix et al.*, 2007). The relative variations of the precession and the eccentricity are obviously important, as the impact of the precession increases with the eccentricity. Hence, the combined impact can work to either strengthen or damp the seasonal insolation cycle. The obliquity changes the relative insolation between high and low latitudes, with largest impact at high latitudes.

In response to the varying insolation, the climate alternates between cold glacial and warmer interglacial states. The glacial-interglacial cycles are evident in proxy data from a wide range of paleoclimate archives: ice cores, marine sediment cores, and continental records (e.g. lake sediments, tree rings, corals, and speleothems). Based on the collected records, the glacial-interglacial cycle appears to have a 100 ka period over the last 800 ka (Figure 2.1; *Masson-Delmotte et al.*, 2013). The interglacials are all characterized by relatively warm conditions, reduced ice sheets, and increased sea level, but vary in duration and magnitude (*Yin and Berger*, 2012). The characteristics of each interglacial is not controlled by insolation alone, but involves non-linear responses of the climate system; especially the greenhouse effect from changing CO_2 has an important impact (*Tzedakis et al.*, 2009; *Yin and Berger*, 2012; *Herold et al.*, 2012).

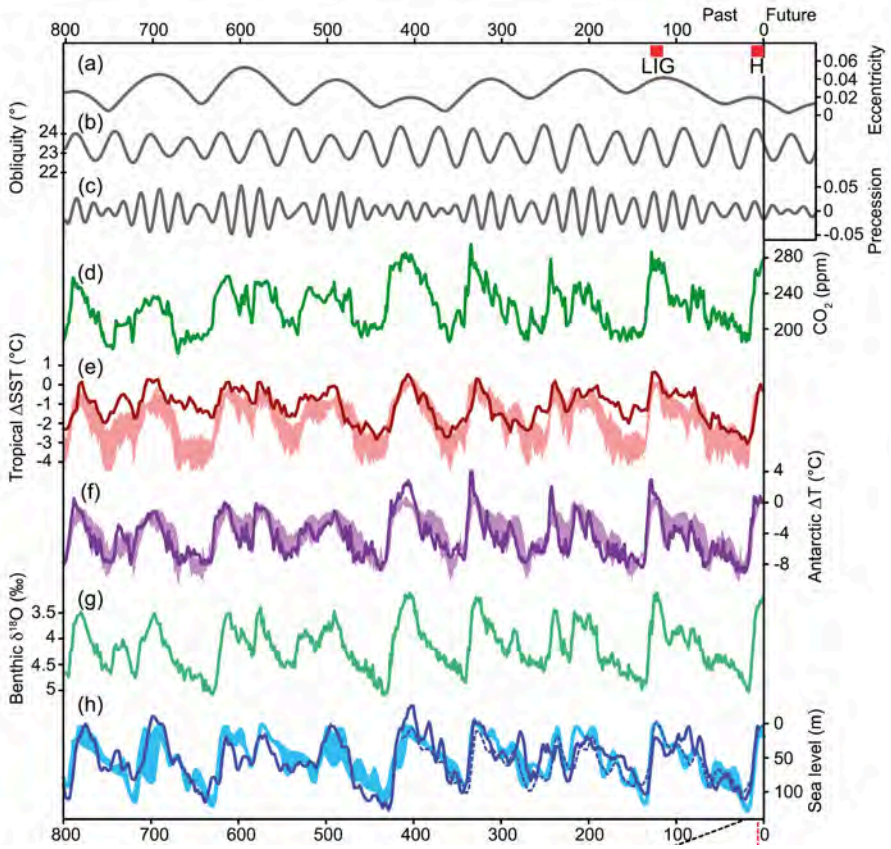

Figure 2.1: From *Masson-Delmotte et al.* (2013): Orbital parameters and proxy records over the past 800,000 years. (a) Eccentricity. (b) Obliquity. (c) Precessional parameter. (d) Atmospheric concentration of CO_2. (e) Tropical sea surface temperature stack. (f) Antarctic ice core temperature stack. (g) Stack of benthic $\delta^{18}O$, a proxy for global ice volume and deep-ocean temperature. (h) Reconstructed sea level. Lines represent orbital forcing and proxy records, shaded areas represent the range of simulations with climate models, climate–ice sheet models of intermediate complexity and an ice sheet model forced by variations of the orbital parameters and the atmospheric concentrations of the major greenhouse gases. LIG (∼130 ka) is marked with a red box in the top of the panel.

Despite the matching timescales of the orbital forcing and the glacial cycles, the Milankovitch theory cannot account for certain characteristics of the climatic history. Questions remain regarding the dominant 100 ka cycle during the recent ∼800 ka which indicates a dominant importance of eccentricity variations despite the relatively weak

associated forcing (*Imbrie et al.*, 1993; *Huybers and Wunsch*, 2005; *Lisiecki*, 2010). A related challenge is the explanation for the so-called mid-Pleistocene transition, where the glacial cycles change from a dominant 41 ka cycle consistent with obliquity variations to the current 100 ka cycle consistent with eccentricity variations (*Huybers*, 2006).

The last interglacial, also known as the Eemian or Marine Isotope Stage 5e, precedes the current Holocene interglacial by approximately 100,000 years. The Earth's orbit had higher eccentricity and axial tilt compared to present day, and northern hemisphere summer solstice occurred near the perihelion. This combination causes a substantial increase of the northern hemisphere summer insolation that, in the Milankovitch view, was the driving factor behind the termination of the penultimate glacial about 130,000 years before present.

2.1.2 The last interglacial

The last interglacial (LIG) lasted from approximately 130–116 thousand years before present (ka). The northern hemisphere summertime insolation (traditionally measured as the June mean insolation at 65°N) peaked around 126 ka, but was above Holocene levels consistently from 129–123 ka.

The insolation forcing led to a relatively warm climate state with global mean temperatures between 0–2 K warmer than the pre-industrial (*Masson-Delmotte et al.*, 2013; *Otto-Bliesner et al.*, 2013). The global mean is dominated by the substantial warming at high latitudes; the long-term average Arctic temperature was at least 2 K warmer than the pre-industrial (*Masson-Delmotte et al.*, 2013). Antarctic ice core records indicate a peak warming of about 3–5 K (*Petit et al.*, 1999; *Jouzel et al.*, 2007; *Stenni et al.*, 2010). Isotope-enabled modelling studies indicate that the temperature-isotope relationship was different during the last interglacial, suggesting that the earliest Antarctic reconstructions of 3±1.5 K warming are likely underestimated (*Sime et al.*, 2009). Generally, the proxy records indicate that the strongest temperature change is found at high northern latitudes; the Arctic region mean summertime temperature increased 4–5 K (*CAPE-Last Interglacial Project Members*, 2006). The warming pattern does, however, not appear uniform, and some locations exhibit more pronounced warming; e.g. annual mean warming of 8±4 K in northwestern Greenland (*NEEM community members*, 2013) and up to 10 K in northern Siberia (*Velichko et al.*, 2008; *Kim et al.*, 2010).

A few comprehensive multi-proxy global data sets have been compiled based on varying criteria (*Turney and Jones*, 2010; *McKay et al.*, 2011; *Capron et al.*, 2014). *Turney and Jones* (2010) compiled 263 proxy records from ice cores, marine cores, and terrestrial sources aiming to quantify the last interglacial temperature change. This compilation suggests a global annual mean warming of 1.9±0.1 K, with the caveat that the data set has biases related to uneven spatial coverage of the records. The strongest warming is found at high latitudes, with some Arctic and sub-Arctic records indicating warming of at least 10 K. Due to the challenges in dating the various records, the data set builds on the assumption that the LIG warming was broadly synchronous, meaning that the records reflect the maximum reconstructed temperatures during the last interglacial period. The more recent compilation by *McKay et al.* (2011) is based on 76 proxy reconstruction of sea surface temperatures (SSTs) supplemented by 94 LIG SST estimates from the CLIMAP project (*CLIMAP Project Members*, 1984). Similar to *Turney and Jones* (2010), this

compilation was based on the warmest LIG estimate from each record (using a 5,000-year mean centered on the peak reconstructed warming). The data set suggests a sea surface warming of 0.7±0.6 K (compared to late Holocene), indicating a contrast between stronger continental and more modest ocean warming (when comparing to the estimate from *Turney and Jones* (2010) which incorporates terrestrial records).

Capron et al. (2014) aimed to improve on the previous data sets by creating a consistently dated data set. Consequently, their data is smaller with a more limited spatial coverage; it is based on 47 records from marine sediment cores (North Atlantic and Southern Ocean) combined with ice cores from Greenland and Antarctica. The data compilation offers temperature reconstructions for four time slices during LIG: 115, 120, 125, and 130 ka. Thus, compared to the previous compilations, this data set takes into account the varying temperature evolution in different regions. Previous studies indicate a large spread in the timing of maximum LIG warming (*Bakker et al.*, 2013; *Loutre et al.*, 2014; *Govin et al.*, 2015) illustrating the need for more accurate dating of records from the last interglacial (as dicussed by *Capron et al.*, 2014; *Govin et al.*, 2015). *Bakker and Renssen* (2014) suggest that the 'synchronous warming assumption' behind the *Turney and Jones* (2010) and *McKay et al.* (2011) data sets may explain part of the observed mismatch between proxy data and climate model simulations (e.g. *Masson-Delmotte et al.*, 2013; *Otto-Bliesner et al.*, 2013).

Smaller regional data compilations supplement the larger compilations (with some overlapping records); e.g. compilations by *Velichko et al.* (2008) and *Kim et al.* (2010) both covering Asia. The two compilations suggest warming and general precipitation increase over Eurasia (especially in the Arctic and sub-Arctic regions).

Sea level

A substantial retreat of the ice sheets occurred coincident with the warming. Current estimates based on coral reef proxies and other geological sea level indicators suggest 6–9 m sea level increase relative to present day (*Kopp et al.*, 2009; *Dutton and Lambeck*, 2012; *Kopp et al.*, 2013; *Dutton et al.*, 2015). There is high confidence that the sea level increase did not exceed 10 m, and comparison of the existing estimates indicates that 6 m is the most likely increase (*Masson-Delmotte et al.*, 2013). *Kopp et al.* (2013) suggest two separate peaks in sea level, indicating that the ice sheet retreat slowed down after an initial rapid reduction and then re-accelerated before reaching LIG minimum (cf. Figure 2.2). Around 125 ka sea level peaked and stabilized, indicating that the ice sheets had reached their minimum extent. *Kopp et al.* (2013) do not offer any detailed interpretation of the two intra-LIG peaks, but perhaps further investigation can reveal whether this pattern is related to different timing of sea level contributions from the Northern and Southern Hemisphere ice sheets.

Ice sheets

The estimated sea level rise of 6–9 m indicates that both Greenland and the Antarctic ice sheet have been reduced compared to their current extent. While other glaciers and smaller ice caps might have provided a minor contribution, the majority of the sea

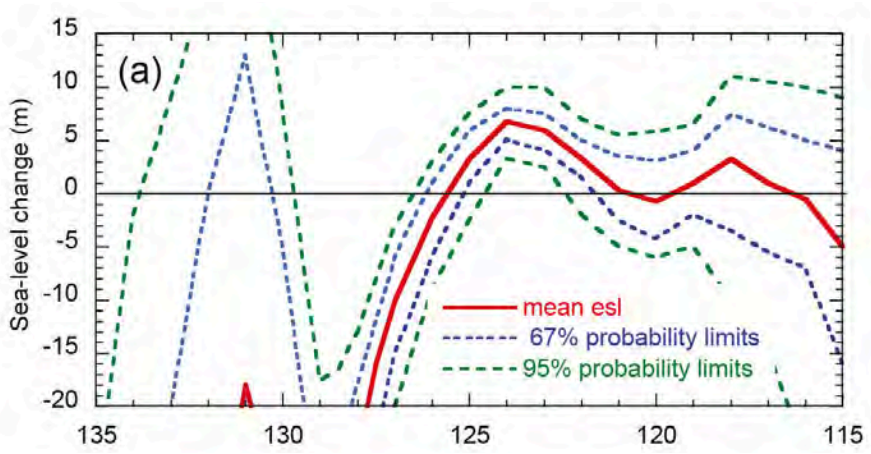

Figure 2.2: From *Masson-Delmotte et al.* (2013), data from *Kopp et al.* (2013): Sea level during the Last Interglacial (LIG) period. Proxy-derived estimate of global mean sea level anomaly: Mean sea level anomaly (red line), 67% confidence limits (blue dashed lines) and 95% confidence limits (green dashed lines). The chronology is based on open-system U/Th dates.

level increase must originate from ice sheets in Greenland, West Antarctica, and/or the lower elevation parts of East Antarctica. The ice sheet extents are, unfortunately, very poorly constrained, as the deep ice cores from Greenland and Antarctica provide the only fix-points for ice sheet reconstructions.

For Greenland, several LIG reconstructions exist; the remaining challenge is that the existing studies result in a very diverse set of ice sheet configurations. As described in *Pedersen et al.* (2016c) (Section 4.1 below) the ensemble of ice sheet reconstructions suggest retreat in southwest (*Helsen et al.*, 2013), retreat in north- and southwest with a separate South Dome ice cap (*Robinson et al.*, 2011), retreat in southwest and north-northeast (*Born and Nisancioglu*, 2012; *Quiquet et al.*, 2013; *Stone et al.*, 2013), and complete loss of the South Dome (*Cuffey and Marshall*, 2000; *Lhomme et al.*, 2005). Figure 2.3 shows four selected recent reconstructions (*Robinson et al.*, 2011; *Helsen et al.*, 2013; *Born and Nisancioglu*, 2012; *Stone et al.*, 2013) illustrating the inter-model span.

Only very few constraints exist that can be used to assess these reconstructions. The deep Greenland ice cores that contain Eemian ice are obvious fix-points. These ice cores are NEEM (77.45°N, 51.06°W; *NEEM community members*, 2013), NGRIP (75.10°N, 42.32°W; *NGRIP members*, 2004), GRIP (72.5°N, 37.3°W; *GRIP members*, 1993) and GISP2 (72.58°N, 38.48°W; *Grootes et al.*, 1993). Additionally, basal parts of the Renland (71.3°N, 26.7°W; *Johnsen et al.*, 1992) and Camp Century (77.2°N, 61.1°W) ice cores contain ice from the Eemian (*Johnsen et al.*, 2001). The DYE-3 ice core further south (65.2°N, 43.8°W; *Dansgaard et al.*, 1982) has distorted layers making it difficult to assess the deepest part of the core (*Johnsen et al.*, 2001), but the basal part contains ice older than the Eemian (*Willerslev et al.*, 2007). Ocean sediment cores further indicate the presence of ice in southern Greenland during the Eemian (*Colville et al.*, 2011). Other than presence of ice dating back to the Eemian, the ice cores can also indicate past elevation changes. Based on the air content in the bubbles trapped in the ice, the NEEM

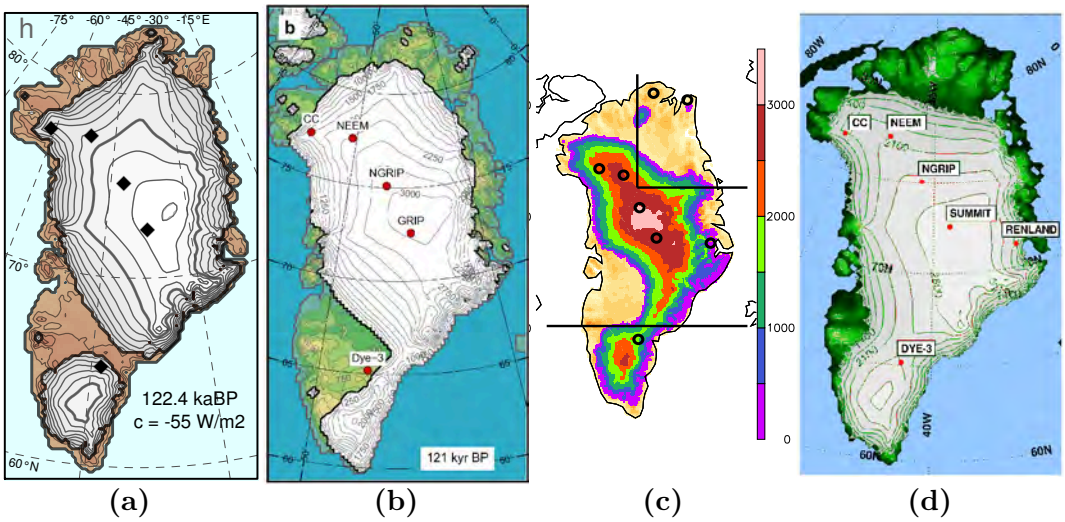

Figure 2.3: Four selected ice sheet reconstructions for the LIG: (a) *Robinson et al.* (2011), (b) *Helsen et al.* (2013), (c) *Born and Nisancioglu* (2012), (d) *Stone et al.* (2013).

ice core indicates limited elevation changes at the ice core site (540±300 m higher at than the present elevation at 128 ka; *NEEM community members*, 2013).

Together, the ice sheet reconstructions and the constraints from the deep ice cores yield a potential GrIS sea level contribution of 1.4–4.3 m (*Masson-Delmotte et al.*, 2013). The sea level rise from Greenland combined with the contributions from smaller glaciers (maximum 0.4 m from melt of all current glaciers; *Vaughan et al.*, 2013) and ocean thermal expansion (estimated 0.4±0.3 m; *McKay et al.*, 2011) is thus only sufficient to explain the low end of the reconstructed sea level range. Consequently, any additional sea level increase must be related to mass loss from the Antarctic ice sheet. Unfortunately, existing research does not provide any reliable reconstruction of the Antarctic ice sheet volume (*Masson-Delmotte et al.*, 2013). Several studies have speculated on a potential contribution from the West Antarctic ice sheet (WAIS), which could be sensitive to sea level rise (i.e. from GrIS) and shallow ocean warming near the ice shelves (*Overpeck et al.*, 2006). While large uncertainties remain regarding the stability of WAIS during LIG, its disintegration could contribute up to 5 m global sea level rise (*Mercer*, 1978), and could cause additional local warming over Antarctica (*Overpeck et al.*, 2006; *Holden et al.*, 2010; *Otto-Bliesner et al.*, 2013).

Vegetation

Vegetation feedbacks were likely amplifying the LIG warming. Multiple sources indicate the LIG climate favored substantial vegetation changes compared to the pre-industrial. Proxy records from the Arctic region indicate a general northward shift in the vegetation types: The Arctic and sub-Arctic tundra was replaced by boreal and deciduous forest which regionally extended to the coast of the Arctic Ocean (*Lozhkin and Anderson*, 1995; *Edwards et al.*, 2003). Climate-vegetation models of varying complexity find the same tendency (*Harrison et al.*, 1995; *Schurgers et al.*, 2007; *Nikolova et al.*, 2013), along with an increased Arctic warming related to the expanded vegetation (*Crucifix and Loutre*, 2002; *Schurgers et al.*, 2007). The increased warming can be explained by the albedo

impact of the changed vegetation. Replacing tundra or bare ground with forest leads to a decreased albedo that favors increased local warming throughout the year (*Bonan et al.*, 1992). Especially relevant for the Arctic region, snow covered forest has a lower albedo compared to snow covered ground or lower vegetation (*Betts and Ball*, 1997). *Swann et al.* (2010) further find that broad-leaf forest increases the greenhouse effect through increased transpiration of water vapor. While this could further impact the Arctic region, *Schurgers et al.* (2007) conclude that the climatic impact of the vegetation mainly is related to albedo changes.

Vegetation changes also have a potentially important impact in the tropical region. Strengthened African monsoon has been shown to drive an expansion of the Sahel region vegetation northward into the Saharan desert (*Schurgers et al.*, 2007; *Fischer and Jungclaus*, 2010). *Fischer and Jungclaus* (2010) find that the related albedo reduction only has a limited impact due to the increased cloudiness in the region. The dominant effect is rather increased transpiration which strengthens the hydrological cycle and thus initiates a positive vegetation feedback.

Evidently, the vegetation feedbacks are potentially important for the LIG climate at both high and low latitudes. *Lunt et al.* (2013) conclude that the current gap between models and proxy data could be reduced by include active vegetation response in the classical atmosphere-ocean general circulation model (GCM) experiments.

Monsoon

The monsoonal regions have been proven sensitive to orbital insolation forcing in both modelling studies and proxy records. Marine sediment records from Western Africa (*Gingele et al.*, 1998; *Govin et al.*, 2014) and the Mediterranean (*Rossignol-Strick*, 1985) are affected by river outflow and indicate an increased African monsoon during the LIG. Models of varying complexity agree on a LIG summertime monsoon intensification over Northern Africa (the Sahel region south of Sahara) as well is over India and Southeast Asia (*de Noblet et al.*, 1996; *Montoya et al.*, 2000; *Braconnot et al.*, 2008). The monsoon response has been studied in detail both in these paleoclimate modelling studies using LIG forcing and in modelling studies with more conceptual insolation forcing (e.g. *Bosmans et al.*, 2015). Together, these studies have identified a mechanism responsible for the monsoon intensification; as also reviewed by *Pedersen et al.* (2016b) in Section 3.3. The monsoon increase is driven by increased warming of the continents (by insolation during summer) which increases ocean-land thermal and pressure gradients (*Braconnot et al.*, 2008; *Bosmans et al.*, 2015). The increased gradients and strengthened thermal low systems over land drive increased winds and moisture transport from the ocean to the continent. The moisture sources for precipitation increase are increased inland moisture transport and local recycling (from evaporation); the latter being a minor contribution. A consequence of the intensified monsoon is that the continental temperatures are expected to decrease due to increased cloud cover and evaporation (*de Noblet et al.*, 1996; *Montoya et al.*, 2000; *Bosmans et al.*, 2015). This monsoon related cooling is also evident in the multi-model mean from *Lunt et al.* (2013).

Paleoclimate model experiments

The last interglacial period has been subject to several previous modelling studies. The LIG has previously been proposed as a parallel to a potential future warm climate. Continued research has, however, led to the current conclusion that the LIG is a poor future climate analogue due to the nature of the forcing: The spatially uniform forcing from increased greenhouse gas concentrations cannot be compared directly to the geographically uneven orbital insolation forcing. As discussed by *Pedersen et al.* (2016b) (cf. Section 3.1), there are similarities in the temperature responses, especially a pronounced high latitude warming from the so-called Arctic amplification of near-surface warming (*Serreze and Barry*, 2011). More importantly, the availability of paleoclimate information means that simulations of the last interglacial are an opportunity to evaluate model performance outside of near-present day conditions, potentially leading to improved projections of future warming (*Otto-Bliesner et al.*, 2006; *Braconnot et al.*, 2012; *Otto-Bliesner et al.*, 2013). For this reason, the last interglacial is part of the most recent set of PMIP experiments aiming to evaluate model performance based on paleoclimate experiments and proxy data archives (PMIP3, The Paleoclimate Modelling Intercomparison Project; *Braconnot et al.*, 2012; *PMIP3*, 2010).

Models of varying complexity have been employed for paleoclimate simulations. EMICs (Earth-System Models of Intermediate Complexity) have the advantage of being computationally inexpensive and thus allow multi-millennium transient simulations. These simple model types can thus be used to assess the temporal evolution of the climate, e.g. as done by *Bakker et al.* (2013) for the temperature evolution through the LIG. An alternate approach in paleoclimate modelling is using more complex general circulation or Earth system models. The more comprehensive models can provide more information on the circulation, dynamics and climate mechanisms, but require more computational resources. Consequently, the majority of GCM paleo-experiments are equilibrium simulations focusing on a single time slice (*snap shot* simulations). *Lunt et al.* (2013) presented a multi-model ensemble based on 16 recent LIG equilibrium simulations (mainly GCMs), which was also the basis for the LIG model assessment in the most recent IPCC report (*Masson-Delmotte et al.*, 2013). Figure 2.4, from the AR5 IPCC report, compares the multi-model mean to the proxy data compilations by *Turney and Jones* (2010) and *McKay et al.* (2011), and reveals considerable differences between the model mean and the reconstructed temperatures. With the caveat that the model simulations represent 128–125 ka and the datasets, as noted above, simply represent maximum LIG warming at each location, this comparison indicates shortcomings in the models and/or the experiment designs.

The multi-model mean indicates very low annual mean global warming (0.0 ± 0.5 K). The only robust features across the models are Arctic warming and cooling in the African and Indian monsoonal regions. The seasonal and regional patterns show qualitative agreement with the proxy records, but underestimate the magnitude of the changes (in agreement with the findings by *Braconnot et al.*, 2012; *Otto-Bliesner et al.*, 2013). The dominant seasonal changes are Northern Hemisphere (NH) mid- to high latitude warming during summer (June-July-August, JJA) and global cooling during NH winter (December-January-February, DJF).

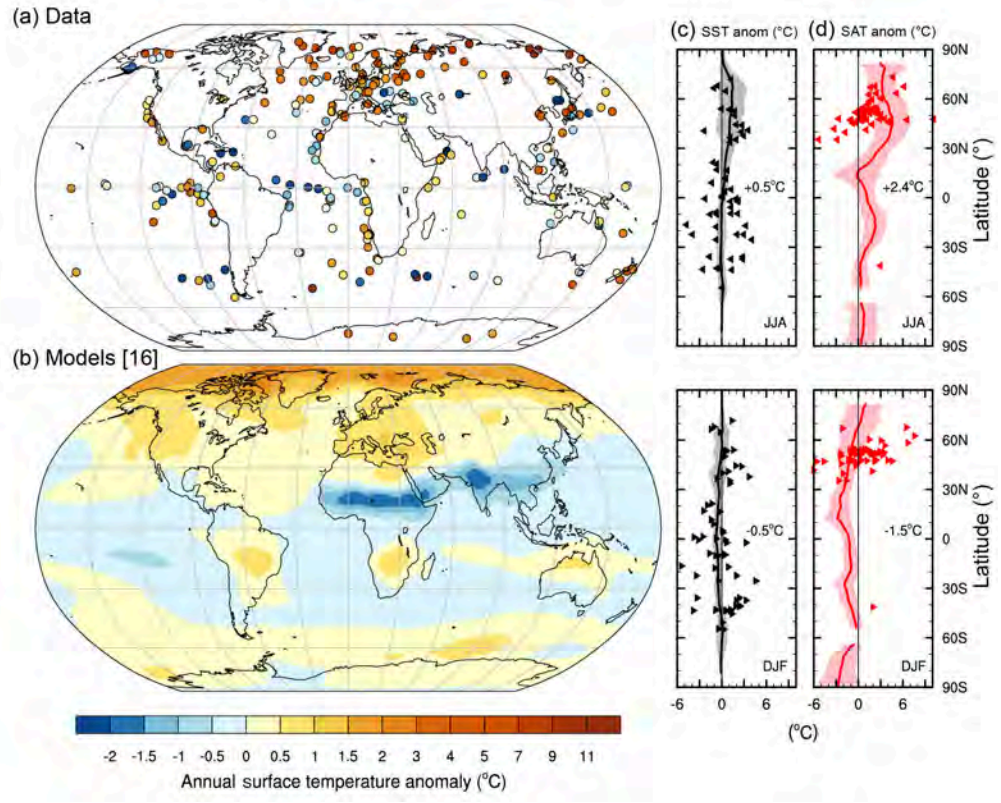

Figure 2.4: From *Masson-Delmotte et al.* (2013), based on *Lunt et al.* (2013), *Turney and Jones* (2010) and *McKay et al.* (2011): Changes in surface temperature for the Last Interglacial (LIG) as reconstructed from data and simulated by an ensemble of climate model experiments. (a) Proxy data syntheses of annual surface temperature anomalies as published by *Turney and Jones* (2010) and *McKay et al.* (2011). (b) Multi-model average of annual surface air temperature anomalies simulated for the LIG computed with respect to pre- industrial from (*Lunt et al.*, 2013). (c) Seasonal SST anomalies. Multi-model zonal averages are shown as solid line with shaded bands indicating 2 standard deviations. Plotted values are the respective seasonal multi-mean global average. Symbols are individual proxy records of seasonal SST anomalies from *McKay et al.* (2011). (d) Seasonal terrestrial surface temperature anomalies (SAT). As in (c) but with symbols representing terrestrial proxy records as compiled from published literature (Table 5.A.5 in *Masson-Delmotte et al.*, 2013).

Due to missing uncertainty estimates for the proxy compilation, *Lunt et al.* (2013) cannot thoroughly assess the model-data mismatch, but instead suggest a list of potential actions to improve the model estimates and model-data intercomparison:

(1) *Inclusion of more realistic boundary conditions.* The "classical" PMIP style simulations could be improved by incorporation of changed ice sheets and vegetation.

(2) *Use of state-of-the-art models.* The models estimates in the *Lunt et al.* (2013) ensemble could be improved by introducing higher resolution, improved dynamics, more complex parameterizations, and additional "elements" of the Earth system.

(3) *More transient simulations.* These could reveal the evolution of the climate through the interglacial, and provide a better basis for comparison with well-dated, high-resolution proxy records.

(4) *Proxy data of seasonal conditions.* The annual mean response during the LIG is much weaker compared to the seasonal changes. Proxy data representing seasonal conditions may be a better basis for model-data comparison.

(5) *Uncertainty estimates for the proxy records.* Uncertainty estimates on the reconstructed temperatures would improve the value in model-data comparisons.

A secondary point from *Lunt et al.* (2013) is an apparent difference between the EMIC and GCM simulations; the annual mean temperature anomalies exhibit very different patterns. While the EMICs simulate stronger Arctic warming, the GCMs have a more complex response and simulate a stronger monsoon-related cooling over Northern Africa and India. The differences in the monsoonal region highlight the impact of the simplified atmospheric representation in the EMICs, especially related to the treatment of clouds. The authors do not discuss in detail potential reasons for the temperature difference in the Arctic, but we speculate that the representation of clouds could contribute to the difference; previous studies have shown that cloud changes play a central role in a warming Arctic (e.g. *Vavrus et al.*, 2008; *Boucher et al.*, 2013). This further motivates the use of more complex models for paleoclimate experiments.

This project follows some of the recommendations from *Lunt et al.* (2013). Our experiments are performed in an unprecedented high spatial resolution (cf. item (2) above), and we incorporate the proxy compilation from *Capron et al.* (2014) which consist of well-dated, seasonal proxy records with uncertainty estimates (cf. item (4) and (5) above).

2.2 The Arctic sea ice

This introductory section will review the role of the Arctic sea ice in the climate system. The relevance of studying the climatic changes related to Arctic sea ice have been illustrated via previous studies of both past, present, and future climate states. This section will cover the mechanisms related to change in the Arctic sea ice cover, and discuss both the local and remote impacts of sea ice changes.

The sea ice has two important effects: (1) the *albedo* effect and (2) the *insulation* effect (Vaughan et al. 2013; Vihma 2014). (1) describes the much lower surface albedo of sea ice compared to open ocean. The albedo of sea ice varies through the seasons, but bare white ice and snow-covered ice have albedos of 0.65 and 0.8–0.9, respectively (*Perovich et al.*, 2002). Hence, the sea ice considerably increases the amount of reflected solar radiation compared to the darker ocean surface. (2) describes insulating properties of the sea ice inhibiting heat and moisture fluxes between the ocean and the atmosphere. The sea ice thus changes the characteristics of the climate near the Arctic Ocean making the region drier and colder; especially during winter.

The sea ice is obviously sensitive to temperature changes, and both of these properties further increases this sensitivity. Changes in the sea ice cover initiates a positive feedback mechanism known as the surface (or ice) albedo feedback: sea ice melt decreases the surface albedo causing increased absorption and thereby warming and melting. This positive feedback similarly enhances the opposite process with initial cooling and sea ice

growth. The albedo feedback is acting during summer; the impact is obviously limited during the polar night.

A similar positive feedback is related to the insulation effect. Initial loss of sea ice favors additional warming due to increased heat flux from the ocean (e.g. *Screen and Simmonds*, 2010a). Opposite the albedo feedback, this effect is dominant during winter, when the temperature gradient between atmosphere and ocean is at its maximum. During summer, the lower atmosphere and the ocean have comparable temperatures and thus only a limited heat exchange.

These two feedbacks illustrate the potential central role of the sea ice cover in promoting Arctic warming; the concept known as Arctic amplification (*Serreze et al.*, 2009; *Screen and Simmonds*, 2010b; *Serreze and Barry*, 2011). Although traditionally ascribed to the albedo feedback alone (originally by *Arrhenius*, 1896), recent studies have illustrated several contributing factors to Arctic amplification (e.g. *Serreze and Barry*, 2011). These include changes in surface heat fluxes related to sea ice (*Serreze et al.*, 2009; *Screen and Simmonds*, 2010b), atmospheric heat transport (*Graversen et al.*, 2008; *Alexeev et al.*, 2005; *Screen et al.*, 2012), ocean heat transport (*Holland and Bitz*, 2003; *Polyakov et al.*, 2010), cloud cover (*Francis and Hunter*, 2007; *Abbot et al.*, 2009; *Graversen and Wang*, 2009), and aerosols (i.e. both the albedo effect of soot on snow and the direct/indirect effects of airborne aerosols; *Hansen and Nazarenko*, 2004; *Shindell and Faluvegi*, 2009).

2.2.1 Sea ice and paleoclimate

The concept of Arctic amplification is known from past, current, and projections of future climate states (*Masson-Delmotte et al.*, 2006; *Miller et al.*, 2010; *Serreze and Barry*, 2011). In past climate states forced by orbital insolation forcing the Arctic sea ice not only promotes Arctic warming, but also acts to change the seasonal imprint of the insolation anomalies. This project focuses on the last interglacial, where high northern latitudes were forced by increased summertime insolation balanced by an earlier onset of the polar night during the fall. If the climate system was responding *linearly* to this forcing, we would thus only observe warming during summer and cooling during fall. The sea ice, however, is one element of the climate system that provides a "memory effect" (*Tuenter et al.*, 2005; *Yin and Berger*, 2012; *Otto-Bliesner et al.*, 2013). The summertime insolation anomaly drives increased melt during summer which, despite the cooling anomalies during fall, is manifested as a year-round reduction of the sea ice extent. The reduced ice cover leads to wintertime warming driven by the insulation effect, i.e. the increased heat flux from the ocean surface. The heat flux is further strengthened due to increased absorption during summer leading to upper-ocean warming. While this mechanism is well-established, model comparisons by *Otto-Bliesner et al.* (2013) and *Nikolova et al.* (2013) indicate that the strength of this memory effect vary among models, and depend on the sea ice sensitivity of the particular model. Consequently, the sea ice could give rise to inter-model differences in simulations of the LIG; especially related to Arctic winter warming. This leads *Otto-Bliesner et al.* (2013) to conclude that "*sea ice is important for understanding model polar responses*", which further motivates research of the climatic impact of sea ice changes.

2.2.2 Effects of Arctic sea ice loss

The recent reduction of the Arctic sea ice cover (*Vaughan et al.*, 2013) has motivated an increasing number of studies focusing on the Arctic sea ice (cf. recent review papers by *Budikova*, 2009; *Bader et al.*, 2011; *Vihma*, 2014). Besides investigating the reasons for the sea ice loss (*Polyakov et al.*, 2012; *Stroeve et al.*, 2012b), several studies are concerned with the impacts of this sea ice loss. The latter will be a key focus throughout this project, as the climatic mechanisms related to sea ice retreat are relevant for both past and potential future warm climates.

The mechanisms described above illustrate the importance of sea ice changes for the local Arctic climate. Interestingly, the sea ice changes also appear to exert an impact beyond the polar region. The simplest larger scale impact is horizontal advection of heat from the regions of ice loss (*Serreze et al.*, 2009, 2011). This will only impact a limited geographical region and likely exert no significant changes beyond the Arctic region. Large-scale circulation impacts have, however, been associated with sea ice loss, and several studies suggest links between the Arctic sea ice and mid-latitude climate changes (*Bader et al.*, 2011; *Vihma*, 2014).

The large-scale impact of sea ice loss has been illustrated through studies of the North Atlantic Oscillation (NAO). The NAO describes the pressure pattern over the North Atlantic region with prevailing low pressure in the north near Iceland and high pressure in the south near the Iberian Peninsula and the Azores (e.g. *Hurrell et al.*, 2003). The pattern is especially pronounced during winter, and is the dominant mode of variability in the region (as illustrated e.g. by an Empirical orthogonal function (EOF) analysis; cf. Section 5.3). The relative strength of the high and low pressure is closely related to the storm tracks and the circulation that impacts European and Asian conditions. The relative strength is traditionally illustrated by the NAO index, calculated as the north-south pressure difference normalized by the climatological value (*Hurrell and National Center for Atmospheric Research Staff (Eds.)*, 2015). Several studies have investigated the link between sea ice loss and the NAO using both observations, reanalysis data, and GCM experiments (*Alexander et al.*, 2004; *Deser et al.*, 2004; *Magnusdottir et al.*, 2004; *Kvamstø et al.*, 2004; *Seierstad and Bader*, 2008; *Strong and Magnusdottir*, 2010; *Outten and Esau*, 2012; *Jaiser et al.*, 2012; *Peings and Magnusdottir*, 2014). Despite varying conclusions, the majority of these studies indicate that sea ice loss favors and a negative NAO response, i.e. a decreased north-south pressure gradient (as summarized by *Vihma*, 2014).

The link to the NAO illustrates that the Arctic sea ice can affect mid-latitude climate. In a simplistic view, the mid-latitude flow is driven by the equator-to-pole gradient of the geopotential height surfaces, as illustrated by the thermal wind relation (*Holton and Hakim*, 2013):

$$u_T = -\frac{1}{f}\frac{\partial}{\partial y}\left(\Phi_{\text{top}} - \Phi_{\text{bottom}}\right) \tag{2.1}$$

where u_T is the zonal wind, f the Coriolis parameter, y the latitude, and Φ the geopotential height of the given pressure-surfaces. Hence, the zonal wind is controlled by the equator-to-pole gradient of the geopotential height (e.g. the height between the 1000 (bottom) and 500 hPa (top) pressure levels).

The Arctic warming from sea ice loss increases the high-latitude geopotential height (e.g. *Overland and Wang*, 2010), and could thus decrease mid-latitude zonal flow. GCM experiments suggest that such a reduction of the zonal flow could be associated with increased meandering of the mid-latitude storm tracks (*Liu et al.*, 2012; *Francis and Vavrus*, 2012; *Peings and Magnusdottir*, 2014; *Francis and Vavrus*, 2015). *Francis and Vavrus* (2012) suggest that the increased meandering may lead to slower eastward propagation of weather systems and thus more persistent mid-latitude weather. This finding is, however, still subject to scientific debate and investigation (*Screen and Simmonds*, 2013; *Barnes*, 2013; *Coumou et al.*, 2014; *Wallace et al.*, 2014). Recent findings support a link between the wavier planetary waves and extreme weather conditions, but illustrate the complexity of this mechanism: The meandering does not favor all types of persistent weather, but different types of persistent conditions (i.e. heat waves, cold waves, droughts, and wet extremes) occur in different mid-latitude regions (*Screen and Simmonds*, 2014; *Screen et al.*, 2015).

Another complicating factor in the assessment of the linkages between the sea ice and the large-scale circulation is that the circulation response appears sensitive to the location of the ice loss (*Petoukhov and Semenov*, 2010; *Rinke et al.*, 2013). Especially the observed sea ice decline in the Barents-Kara Sea region has been identified as important for the atmospheric circulation, and the occurrence of cold winters in Eurasia (*Petoukhov and Semenov*, 2010; *Yang and Christensen*, 2012; *Tang et al.*, 2013; *Mori et al.*, 2014; *Overland et al.*, 2015). We will further explore the sensitivity of the atmospheric circulation to the location of sea ice loss in Chapter 5.

2.3 General Circulation Models

2.3.1 Paleoclimate experiments: EC-Earth

The model employed for the paleoclimate experiments in this project is the EC-Earth version 3.1. This is the latest version, the last intermediate release before the expected CMIP6 (Climate Model Intercomparison Project 6) version. EC-Earth is an earth system model (*Hazeleger et al.*, 2010, 2012) with the primary components:

- Integrated Forecasting System atmospheric model (IFS, cycle 36r4, *European Centre for Medium-Range Weather Forecasts*, 2010)
- NEMO ocean model (version 3.3.1, *Madec*, 2011)
- LIM3 sea ice model (*Vancoppenolle et al.*, 2009)
- H-TESSEL land surface model (*Balsamo et al.*, 2009)

The IFS atmospheric model has a spectral resolution of T159. All physical processes are computed on the associated reduced Gaussian grid with 1.125° horizontal resolution (longitudinal resolution is reduced towards the poles to maintain approximately the same grid cell area globally). The model has 62 layers in the vertical ranging from the surface to 5 hPa. The model employs a semi-lagrangian advection scheme allowing efficient computations with 1-hour time steps (e.g. *Hazeleger et al.*, 2012). Through the coupler IFS sees eight different surface types (tiles) in each grid-cells reflecting the ocean, sea ice, or various land surfaces. The land surface model H-TESSEL has four active soil layers

extending to ∼3 m depth, and calculates run-off based on pre-defined river basins. The run-off does not incorporate delayed river transport, but is distributed instantaneously into ocean points nearby the outlets of major rivers. A similar treatment is applied over the ice sheets, where any snow exceeding a total depth of 10 m (water equivalent) is removed and serves as run-off into the ocean. This is thus a simple representation of the freshwater flux from ice sheet calving, and avoids stockpiling of snow on the interior ice sheets. An important note related to the ice sheets and the snow cover, is that EC-Earth does not have an explicit glacier surface type. Consequently, if the ice sheets lose their snow cover (e.g. in the ablation zones or in warm climate simulations) the bare surface can, in an unphysical manner, warm beyond the freezing (thawing) point of ice. Hence, if the "ice sheet surface" is revealed this could initiate unrealistically high sensible heat fluxes from the surface to atmosphere (cf. further discussion in sections 4.3.2 and 4.5).

The NEMO ocean model is employed in a 1° horizontal resolution with 46 levels. The thickness of the layers increases with depth from 10 m to 300 m, and the bottom of the deepest layer is at 5,500 m. The grid is a so-called ORCA grid with a tri-pole configuration, which avoids a North Pole singularity with poles in Siberia, Northern Canada, and at the South Pole (e.g. *Sterl et al.*, 2012). The associated sea ice model (LIM3) runs on the same grid. LIM3 has 5 layers through the sea ice and is employed in its simple setup without ice thickness subcategories (as model tuning has not yet been performed for the more advanced subcategory mode).

As EC-Earth v3.1 is a recent intermediate version, only a limited number of scientific studies have been based on this particular version. Substantial performance analysis and assessment has, however, been carried out by the EC-Earth consortium in the tuning process of the model (*Davini et al.*, 2014). Compared to the widely used CMIP5 version (v2.3) both the atmospheric and oceanic models have been updated, and thus the new version required a substantial tuning effort. As documented by *Mauritsen et al.* (2012), tuning is an integral part of configuring climate models by making adjustments to optimize the model representation of well-known, well-observed climate variables (e.g. temperature, precipitation, sea ice cover). The priority is usually on surface air temperatures, e.g. due to the widespread impact on other climatic variables and the widespread observational coverage (*Davini et al.*, 2014; *Mauritsen et al.*, 2012). Tuning is, hence, based on near-present conditions due to the availability of observations. Assessment of paleoclimate simulations relative to proxy records are therefore an important secondary test bed to ensure that the model applies outside near-present conditions (as discussed by e.g. *Braconnot et al.*, 2012; *Otto-Bliesner et al.*, 2006, 2013; *Flato et al.*, 2013).

The previous EC-Earth version performed well in the CMIP5 group (*Flato et al.*, 2013), and the tuning group's assessment reveals a similar performance for the new version (*Davini et al.*, 2014). There is, however, remaining regional biases that may impact the results of v3.1 simulations. It is important to note that the bias assessment is based on comparison of observations and equilibrium climate simulations with perpetual year 2000 boundary conditions. Hence, the bias plots are essentially comparing the transient climate of the real world to a model representation of an equivalent equilibrium climate; these two climate states could have substantial differences even with a perfect model representation. *Davini et al.* (2014) compare EC-Earth v.3.1 to the gridded observational dataset CRU (*Mitchell and Jones*, 2005; *New et al.*, 1999). Selected relevant findings include:

Surface air temperature:

Illustrated in Figure 2.5. The overall pattern reveals a warm bias in the Arctic and a general cold bias in the tropics. The Arctic does, however, reveal some regional differences: A substantial warm bias in the in Eastern Siberia is contrasted by cold bias over most of Greenland (strongest near the southeast coast).

Sea ice:

A positive bias generally in the sea ice concentration (both Arctic and Antarctic). Largest differences are in the southernmost areas of the Arctic sea ice cover. The ice thickness is not assessed by *Davini et al.* (2014), but previous version of EC-Earth have tended to overestimate ice thickness (*Hazeleger et al.*, 2012; *Sterl et al.*, 2012). The contrast of relatively warm (regionally) conditions at high latitudes and overestimated sea ice area and thickness suggest that there is likely (at least) two model issues affecting the polar regions; perhaps one related to ocean-sea ice interaction and one affecting Arctic atmospheric conditions.

AMOC:

A maximum AMOC strength between 18–20 Sv, which is in agreement with the recent observational estimate of 18.7 Sv (*Cunningham et al.*, 2007). In this EC-Earth version, the AMOC is associated with two regions of deep convection; one in the Labrador Sea and the other in the Greenland-Iceland-Norway Seas, south of Svalbard (*Davini et al.*, 2015).

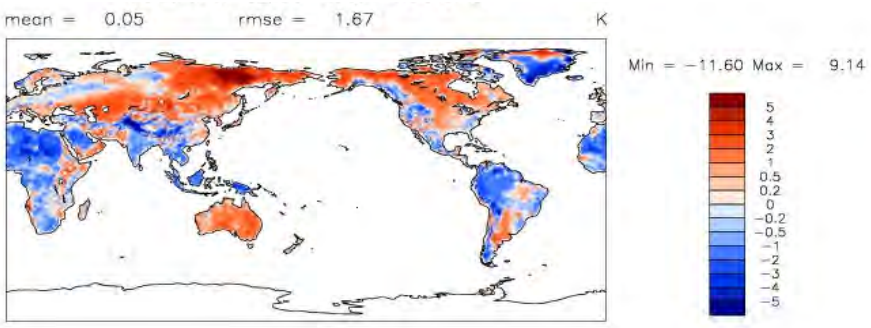

Figure 2.5: From *Davini et al.* (2014). Bias assessment for EC-Earth compared to the CRU dataset: Annual mean near-surface air temperature difference $T_{\text{EC-Earth}} - T_{\text{CRU}}$.

EC-Earth is based on the weather foresting system of ECMWF, and is thus not designed as a traditional climate model. One consequence is that the insolation is fixed in the model to present-day conditions. An early task in this project has, thus, been to expand the model with module calculated varying insolation based on orbital parameters. Such a module has been implemented using code modifications developed at Stockholm University (*Muschitiello et al.*, 2015; *Zhang*, 2013) based on the equations by *Berger* (1978). As outlined in Section 2.1 the orbit is defined by the eccentricity (e), the obliquity (ϵ) and the precession (i.e. $\widetilde{\omega}$, the longitude of perihelion + 180°). The insolation at the top of the atmosphere depends on all three parameters, and is calculated as (*Berger*, 1978):

$$S = \frac{86.4 S_0}{\pi \left(\frac{r}{a}\right)^2} \left(H_0 \sin(\phi) \sin(\epsilon) \sin(\lambda) + \cos(\phi) \cos(\epsilon) \sin(\lambda) \sin(H_0)\right) \tag{2.2}$$

where S_0 is the solar constant, r the Earth-Sun distance, a the semi-major axis of the orbit, H_0 the hour-angle at sunrise/sunset, ϕ the geographical latitude, ϵ the obliquity, and λ the true longitude (which depends on e and $\widetilde{\omega}$). Interactive calculation of the insolation has been implemented in EC-Earth using the structure from NCAR Community Atmosphere Model (*Collins et al.*, 2004) facilitating paleoclimate experiments presented in Chapter 3 and 4.

2.3.2 Sea ice experiments: CESM

A second GCM is employed for a series of idealized experiments investigating the atmospheric response to sea ice loss (Chapter 5). These climate model experiments are performed in the National Center for Atmospheric Research's Community Earth System Model (CESM). We employ CESM version 1.0.4 (*Gent et al.*, 2011) consisting of:

- Community Atmosphere Model version 4 (CAM4; *Neale et al.*, 2010, 2013)
- Community Land Model version 4 (CLM4; *Lawrence et al.*, 2011)
- Los Alamos Sea Ice Model version 4 (CICE; *Bailey et al.*, 2010; *Hunke and Lipscomb*, 2008)
- Los Alamos Parallel Ocean Program Model version 2 (POP2; *Smith et al.*, 2010)

For this project, the full setup has only been used to simulate a pre-industrial control climate (the same control simulation used by *Caldeira and Cvijanovic*, 2014; *Cvijanovic and Caldeira*, 2015). The primary experiments are performed in a slab ocean setup (SOM, slab ocean model), where a thermodynamical mixed layer ocean replaces the full depth ocean (*Bitz et al.*, 2012; *Danabasoglu and Gent*, 2009; *Neale et al.*, 2010). The SOM is designed to approximate the behavior of the full ocean model, and interactively calculates sea surface temperatures using a set of climatological oceanic fields from a fully coupled simulation (*Bailey et al.*, 2011). As the slab ocean is a well-mixed layer with no ocean circulation, heat transport by ocean currents are represented through the so-called Q-flux describing the ocean heat convergence. The Q-flux is calculated as the implied heat convergence based on (*Bailey et al.*, 2011; *Bitz et al.*, 2012):

$$\rho_0 \; c_p \; h_{\mathrm{mix}} \frac{\partial T_{\mathrm{mix}}}{\partial t} = F_{\mathrm{net,sfc}} + Q \tag{2.3}$$

where ρ_0 is the density of seawater, c_p the ocean heat capacity, h_{mix} the mixed-layer depth, T_{mix} the mixed-layer temperature (identical to the SST per definition), $F_{\mathrm{net,sfc}}$ the net surface heat flux, and Q is the implied horizontal and vertical flux of heat into/out of the local mixed-layer column. Note that the $F_{\mathrm{net,sfc}}$ includes energy exchange from the atmosphere-ocean interaction, from ocean-ice processes and the sensible latent heat from snow (falling into the ocean) and run-off (which includes "ice-calving").

Danabasoglu and Gent (2009) assess the older and more simple SOM of CCSM3, and find that it provides a good estimate of the climate sensitivity of the full coupled model. It is, however, important to note that the simple SOM with a fixed Q-flux field cannot capture any thermohaline or wind-driven ocean circulation responses (*Caldeira and Cvijanovic*, 2014; *Deser et al.*, 2016; *Pedersen et al.*, 2016a).

In the current model version, the slab ocean setup includes the active sea ice model, and thus the SOM also require input of climatological salinity and ocean currents (similarly obtained from a coupled control simulation). However, as our experiments are designed to investigate idealized sea ice reductions, the CICE model which otherwise would be incorporated in the slab ocean setup has been replaced by a simple data-ocean (i.e. AMIP-style) fixed sea ice prescription. As described by *Pedersen et al.* (2016a) (Section 5.2), we have constructed a new hybrid configuration combining the slab ocean and prescribed ice setups previously used by *Caldeira and Cvijanovic* (2014) and *Cvijanovic and Caldeira* (2015). Our hybrid setup makes it possible to prescribe any sea ice configuration regardless of the simulated climate state. First, the sea ice concentration is prescribed similarly to classical a data-ocean setup. The prescribed ice conditions are maintained by resetting the sea ice thickness in every time step, and hence not allowing any melt. Secondly, sea ice growth is disabled by allowing the sea surface temperatures (i.e. the temperature of the ocean mixed layer) to cool below the freezing point (−1.8°C) without initiating ice formation. Figure 2.6 presents a sketch of the setup.

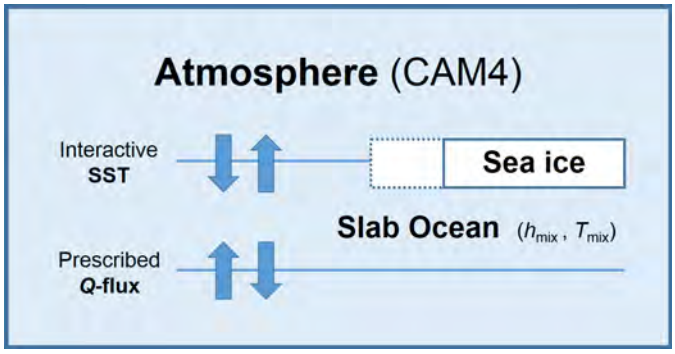

Figure 2.6: Sketch of hybrid CESM slab-ocean setup with prescribed sea ice conditions.

The sea ice fields are specified using the data-ocean routine in CESM. Hence, input fields of sea ice concentration are supplied as mid-monthly values that are interpolated in the model to vary with every time step. The ice thickness fixed at 1 m in the Northern Hemisphere (2 m in the Southern). This thickness is sufficient to effectively insulate the atmosphere from the ocean and thus inhibit any heat exchange.

As discussed by *Pedersen et al.* (2016a) (Section 5.2), it may seem "unphysical" to allow sub-freezing temperatures in the ocean. It is important to realize that this is a conservative choice compared to limiting the temperatures to the freezing point (while still disabling new ice formation). Allowing the ocean to cool below freezing limits the temperature gradient and consequently the heat flux between ocean and atmosphere. The result is a more limited heat flux increase in regions where new sea ice would otherwise form to decrease inhibit the heat exchange.

This setup is an improvement on the traditional GCM setups used to assess the atmospheric response to sea ice loss. The vast majority of such studies use specified, fixed sea ice and sea surface temperature conditions; either observed or based on future projections (e.g. *Alexander et al.*, 2004; *Blüthgen et al.*, 2012; *Deser et al.*, 2004, 2010; *Kumar et al.*, 2010; *Seierstad and Bader*, 2008). As discussed by *Screen et al.* (2013), these experiments must choose to either employ coherent fields of SST and sea ice conditions

or combine reduced sea ice conditions with unchanged SSTs. The former has the advantage of realistic temperature gradients everywhere, but does not describe the isolated impact of sea ice loss: Other factors contributing to global SST changes will also impact the projected climate state. The latter solution has the benefit of isolating the impact of the ice loss, but offers a challenge related to the SSTs in the areas of sea ice loss. If unchanged from the control state these will be at the freezing point. This will apply even during summer when SSTs should, as a direct consequence of the sea ice loss, warm due to increased absorption (albedo effect). To account for this effect, *Screen et al.* (2013) (and subsequent studies by the same authors) create hybrid forcing fields by introducing increased SSTs only in areas of sea ice change. They suggest that this setup "*enables the response to sea ice changes to be isolated*".

Even with the inclusion of increasing SSTs near sea ice loss, the fixed SST configuration will still inhibit more remote responses that could be related directly to the sea ice changes. Previous studies have identified several high-to-low latitude atmospheric teleconnections that depend on SST changes (*Chiang and Bitz*, 2005; *Chiang et al.*, 2008; *Cvijanovic and Chiang*, 2013). Additionally, we speculate that the fixed SST largely inhibit potential atmospheric changes. The inclusion of the slab ocean in our hybrid setup means that SSTs are interactively calculated globally allowing for atmospheric circulation changes and teleconnections that depend on atmosphere-ocean interaction. Furthermore, our setup has the ability to (completely) isolate the impact of sea ice loss: The prescribed sea ice loss is the only forcing induced in our experiments.

Deser et al. (2015, 2016) also discuss the importance of ocean-atmosphere interaction for the atmospheric response to sea ice loss. These studies introduce sea ice reductions in slab and full ocean GCM setups artificially enhancing the downwards longwave fluxes in the Arctic. Hence, the full dynamics of the sea ice model are still active. The caveats, compared to our setup, is that this approach does not allow full control over the sea ice conditions. Furthermore, the modifications of the fluxes will exert an additional warming effect in the Arctic that is the preceding cause of the sea ice loss rather than the subsequent impact. Our hybrid setup is further discussed in Chapter 5 which is based on *Pedersen et al.* (2016a).

3 The last interglacial: Comparing direct and indirect impacts of insolation changes

This chapter is based on *Pedersen et al.* (2016b), which assesses the last interglacial climate using an equilibrium, time-slice GCM simulation. With a particular focus on the changes in the Arctic region, we have chosen to focus on the mid-interglacial climate at 125 ka. While the obliquity peaks near 130 ka, the precession impact means that the high northern latitude summertime insolation peaks near 126 ka (considering the June mean insolation at 65°N). 125 ka is thus near the peak forcing at high northern latitudes and is near the precession optimum; i.e. the insolation increase coincides with summer solstice. We thus expect 125 ka to be near peak Arctic warming; the NEEM ice core (*NEEM community members*, 2013) indicates peak Greenland warming between 128–124 ka. Furthermore, 125 ka is beyond the initial interglacial period where the climate was dominated by the changing ice sheets and ocean conditions (i.e. gradual warming due to ocean thermal inertia and potential circulation changes related to sea ice retreat and freshwater input from melting ice sheets). Sea level studies (*Kopp et al.*, 2013) indicate sea level peaked near 125 ka, suggesting that the ice sheets were stabilizing. Thus, we expect a limited impact of ice sheet changes and freshwater ocean forcing at this time, making it more reasonable to exclude these changes from our model simulations.

The article *Pedersen et al.* (2016b) is included in full extent below with a few minor edits compared to the submitted version. Consequently, parts of the scientific introduction (Chapter 2) is repeated below to ensure a consistent presentation of the study. Following the conclusion from the paper, three subsequent sections offer supplementary analyses and more elaborate discussion of selected parts of the study.

3.1 Introduction

The last interglacial (LIG; also known as the Eemian or MIS5e) lasted from 129 – 116 thousand years before present (ka) and is the most recent period with temperatures higher than present day. Changes in the orbital configuration and thus the insolation resulted in global warming of up to 2°C, with more pronounced warming at high latitudes (*CAPE-Last Interglacial Project Members*, 2006; *Masson-Delmotte et al.*, 2013). Due to the nature of the forcing, the last interglacial is not a perfect analogue for future

greenhouse gas driven warming. Regionally, however, the LIG warming could be comparable to a future, warmer climate state. Future greenhouse gas warming is expected to result in polar amplification of the surface temperature response (*Serreze and Barry*, 2011), which could resemble the pronounced high-latitude temperature response during LIG; especially over the Arctic region (*Masson-Delmotte et al.*, 2011). The availability of paleoclimate information furthermore means that climate model simulations of the last interglacial are an opportunity to evaluate model performance outside of near-present day conditions, potentially leading to improved projections of future warming (*Otto-Bliesner et al.*, 2006; *Braconnot et al.*, 2012; *Otto-Bliesner et al.*, 2013).

The LIG warming over the polar regions caused a reduction of the ice sheets, and a consequent sea level rise of 6 – 9 m (*Kopp et al.*, 2009; *Dutton and Lambeck*, 2012; *Dutton et al.*, 2015). While both the Greenland (GrIS) and Antarctic ice sheets must have contributed to this sea level increase, existing studies present a wide range of ice sheet reconstructions. While the estimated contribution from GrIS of 1.4 – 4.3 m implies a considerable contribution from Antarctica, existing model and observational data is currently insufficient for a reliable quantification of the Antarctic ice sheet changes (*Masson-Delmotte et al.*, 2013).

Several studies have investigated the last interglacial using climate models of varying complexity. Transient simulations usually rely on earth system models of intermediate complexity (*Bakker et al.*, 2013, 2014), while general circulation models (GCMs) primarily are employed for equilibrium, snapshot simulations (*Fischer and Jungclaus*, 2010; *Born et al.*, 2010; *Govin et al.*, 2012; *Lunt et al.*, 2013; *Nikolova et al.*, 2013; *Otto-Bliesner et al.*, 2013; *Langebroek and Nisancioglu*, 2014). Recent model assessments find very low global annual mean warming during LIG, contrasting the proxy reconstruction estimate of 1 – 2 K warming (*Masson-Delmotte et al.*, 2013; *Otto-Bliesner et al.*, 2013). The latest IPCC report estimates a multi-model annual mean surface warming of 0.0 ± 0.5 K (*Masson-Delmotte et al.*, 2013), while *Lunt et al.* (2013) find warming in the Arctic and cooling in the African and Indian monsoon regions as the only robust annual mean results in their intercomparison of 14 models. Seasonally, the models consistently simulate warming over Northern Hemisphere continents during summer (June-July-August; JJA) and global cooling (except in the Arctic) during winter (December-January-February, DJF) (*Lunt et al.*, 2013; *Nikolova et al.*, 2013; *Otto-Bliesner et al.*, 2013; *Langebroek and Nisancioglu*, 2014). While these patterns agree qualitatively with proxy reconstructions, the models generally underestimate the magnitude of the changes (*Braconnot et al.*, 2012; *Masson-Delmotte et al.*, 2013; *Lunt et al.*, 2013; *Otto-Bliesner et al.*, 2013). Several models have the strongest warming occurring in the North Atlantic region as a consequence of retreating sea ice and changes in the ocean circulation (*Fischer and Jungclaus*, 2010; *Lunt et al.*, 2013; *Nikolova et al.*, 2013; *Otto-Bliesner et al.*, 2013).

Continued improvements of GCMs and increased availability and quality of proxy records (*Capron et al.*, 2014; *Govin et al.*, 2015) give reason for continued investigation of the last interglacial. Using the state-of-the-art EC-Earth climate model, we have designed a series of experiments to investigate the last interglacial climate and the mechanisms behind the warming. Specifically, we will assess how the indirect impact of the changed ocean conditions compares to the direct insolation response, and how the relative contributions vary regionally. We focus on the peak Northern Hemisphere warming of the last interglacial, and the experiments are single snapshot, equilibrium simulations forced

with repeating 125 ka boundary conditions. Our experiments are performed in high spatial resolution compared to similar paleoclimate experiments. The highest atmospheric model resolution in the *Lunt et al.* (2013) multi-model ensemble is T85 (corresponding to 1.4° spatial resolution), whereas our experiments have a T159 spectral resolution (approximately 1.1° spatial resolution).

We describe the experiments and the climate model configuration in Section 3.2. In Section 3.3, we present the results of the simulations and assess the direct and indirect impacts of the insolation changes. The results are discussed and compared to proxy records in Section 3.4. Conclusions are presented in Section 3.5.

3.2 Methods

3.2.1 Model configuration

The model used for this study is the EC-Earth global climate model in the most recent version 3.1 (*Hazeleger et al.*, 2010, 2012). EC-Earth consists of the IFS atmospheric model (cycle 36r4, *European Centre for Medium-Range Weather Forecasts*, 2010) and the NEMO ocean model (version 3.3.1, *Madec*, 2011) including the LIM3 sea ice model (*Vancoppenolle et al.*, 2009). The atmospheric model has a T159 spectral resolution (roughly 1.125° × 1.125° horizontal resolution) with 62 layers in the vertical. The NEMO ocean model is running on a tripolar ORCA grid with a horizontal resolution of approximately 1 degree and has 46 levels.

In order to allow paleoclimate simulation, the model has been expanded with an option to modify the insolation according to any given orbital configuration. The insolation is internally calculated following *Berger* (1978) using the same code modification as *Muschitiello et al.* (2015).

3.2.2 Experimental design

The main experiment is a snapshot simulation of the last interglacial period at 125 ka. The experiment is designed following the Paleoclimate Modelling Intercomparison Project PMIP3 protocol (*PMIP3*, 2010; *Braconnot et al.*, 2011, 2012). We focus on 125 ka, when high northern latitude temperatures are near peak LIG warming (*NEEM community members*, 2013; *Bakker et al.*, 2013) and the sea level stabilizing (*Masson-Delmotte et al.*, 2013; *Kopp et al.*, 2013) indicating that ice sheet retreat and related freshwater flux into the ocean is diminishing. In line with the PMIP3 125 ka experiment, the simulation is only forced by insolation changes and changes in the atmospheric gas composition, while the ice sheets and vegetation are kept unchanged. The last interglacial climate is compared to a pre-industrial control simulation, forced by insolation and atmospheric components from 1850. The atmospheric composition and orbital conditions for the last interglacial (LIG) and pre-industrial (PI) experiments are presented in Table 3.1. Figure 3.1 shows the resulting difference in insolation between PI and LIG.

Exp.	Ecc.	Obliq.	Prec.	CO_2 [ppm]	CH_4 [ppb]	N_2O [ppb]
LIG	0.040013	23.798°	307.14°	276	640	263
PI	0.016764	23.459°	100.33°	285	791	275

Table 3.1: Orbital parameters and atmospheric composition of the coupled simulations. Precession is given as $\widetilde{\omega} + 180°$; $\widetilde{\omega}$ denotes the angle of perihelion relative to the vernal equinox (*Berger*, 1978). The LIG experiment is following the PMIP3 last interglacial experiment design suggestions (125 ka experiment, *PMIP3*, 2010)

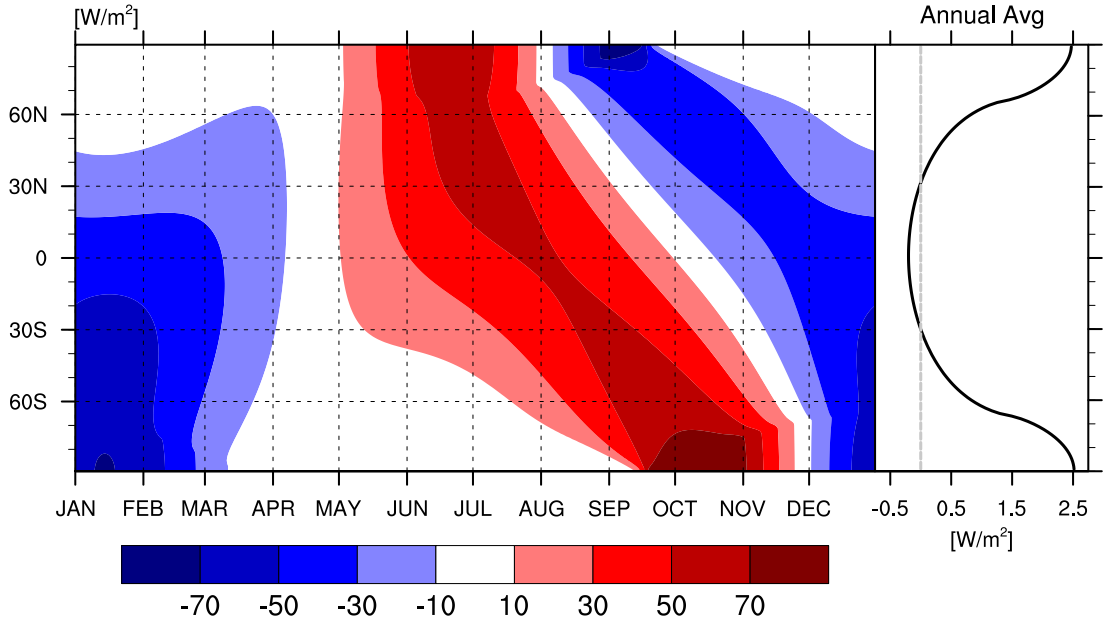

Figure 3.1: Insolation anomalies [W m^{-2}] in LIG compared to PI. Left panel displays zonal anomalies through the year, right panel the zonal annual mean. Time labels on the left panel mark the beginning of each month.

Both simulations have been spun-up to a quasi-equilibrium state. The pre-industrial simulation has a total length of 850 years, and the LIG simulation has been run for a total of 480 years from a present-day state. Our analyses are based on climatologies over the last 100 years from each simulation. Statistical significance of changes is assessed using a two-sided Student's t test (*von Storch and Zwiers*, 2001).

To further investigate the dynamics behind the last interglacial warming, we have designed a series of simulations in an atmosphere-only version of the model (AGCM) based on the two coupled model experiments. The atmospheric model is unchanged, but the ocean model is replaced by prescribed sea surface boundary conditions (sea surface temperatures and sea ice). With these experiments, we aim to disentangle and compare the direct impact of the insolation changes and the secondary impact arising from changed sea surface temperature and sea ice conditions. Accordingly, two hybrid experiments have been designed based on the results from the coupled simulations. The first ("iL+oP") is forced by LIG insolation (and GHGs) and PI SST and sea ice conditions, while the other ("iP+oL") conversely is forced by PI insolation and LIG SST and sea ice conditions. These simulations allow for an assessment of the impact of the

insolation change without the contribution from the oceanic changes, and vice versa. To ensure consistency in the comparison, the pre-industrial and last interglacial climates states are re-simulated in the atmosphere-only setup. These simulations ("iP+oP" and "iL+oL") are forced by the same insolation and GHG values as PI and LIG combined with the climatological SSTs and sea ice conditions obtained in the respective coupled simulation. One caveat is that while the sea ice extent is prescribed to the climatology from the coupled experiments, the sea ice thickness is fixed to 1.5 m everywhere in all AGCM experiments.

Table 3.2 presents an overview of the AGCM simulations. The AGCM simulations all have a total length of 60 years, where the first 10 years are regarded as spin-up. The AGCM simulations exhibit less internal variability compared to the coupled simulations, and 50 years is thus sufficient to get widespread statistically significant changes.

Experiment	**Insolation and GHGs**	**SSTs and sea ice**
iP+oP	PI	PI
iL+oL	LIG	LIG
iL+oP	LIG	PI
iP+oL	PI	LIG

Table 3.2: Boundary conditions for the AGCM experiments. In the experiment names, the letter following "i" indicates the insolation conditions, while the letter following "o" indicates the oceanic conditions: "P" is PI and "L" is Eemian (Last Interglacial).

All the results are presented in monthly and seasonal means following a fixed present-day calendar, although a calendar defining the seasons based on the orbital configuration could be more suitable (*Joussaume and Braconnot*, 1997).

3.3 Results

3.3.1 Coupled experiments

The changed insolation in the LIG gives rise to a global annual mean warming of 0.5 K. The annual mean warming is thus relatively high compared to the recent multi-model mean estimate of 0.0 ± 0.5 K mean annual warming (*Masson-Delmotte et al.*, 2013). Figure 3.2 nonetheless illustrates that the spatial pattern of the simulated warming resembles the multi-model mean from *Lunt et al.* (2013) (cf. Figure 2.4). The annual cycle of the insolation anomalies means that the seasonal insolation cycle is enhanced in the Northern Hemisphere (increase during summer (JJA)) and reduced in the Southern Hemisphere (reduction during summer (DJF)). The most prominent seasonal warming is found during Northern Hemisphere summer (JJA) showing 1.3 K global mean warming (cf. regional warming anomalies in Figure 3.3). The Northern Hemisphere annual mean warming is 0.7 K, while the Southern Hemisphere mean is 0.2 K. The Arctic region (60–90°N) experiences a substantial year-round warming with an annual mean of 2.4 K and seasonal mean warming ranging from 1.8 K in spring (March-April-May; MAM) to 2.9 K during summer (JJA). Figure 3.3 further reveals that the polar regions exhibit

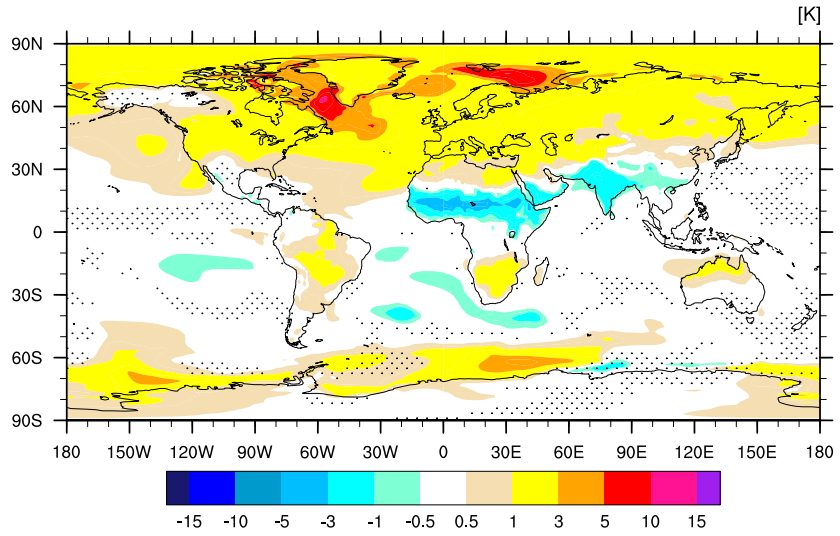

Figure 3.2: Annual mean near-surface air temperature anomalies LIG – PI [K]. Shading denotes changes that are not significant at the 95 % confidence level. Note the irregular spacing of the color bar.

substantially larger standard deviations compared to the global, hemispheric, and tropic means. The primary reason is that the area of the selected polar regions is significantly smaller, and thus larger fluctuations are to be expected. Interestingly, both polar regions exhibit the lowest standard deviations during summer (JJA in the Arctic and DJF in Antarctic) suggesting more stable conditions. The is likely the impact of melting snow and ice: With ice (i.e. snow, sea ice or land ice) in the vicinity the temperature will confined near the freezing (thawing) point as all excess energy will be consumed for ice melt rather than increasing temperatures.

The seasonal mean near-surface air temperature anomalies are presented in Figure 3.4 alongside the zonal mean insolation changes. Comparison of the insolation forcing and the temperature response reveals that the overall response over the continents follows the annual cycle of the insolation anomalies. Nevertheless, some regions stand out with temperature response that cannot be attributed to a direct warming (cooling) from increased (decreased) insolation: High northern latitudes (especially Northern Asia and Greenland) and Europe exhibit warming, and the African and Indian monsoon regions exhibit cooling throughout the year. Consequently, we will give special attention to the responses over the polar regions, the North Atlantic region, and the tropics.

The polar regions

Both polar regions experience substantial forcing from the LIG insolation changes, albeit naturally with different seasonal timing of the changes. 3.1 reveals that the Arctic experiences a positive insolation anomaly which peaks near Northern Hemisphere summer solstice countered by a negative anomaly in the fall, i.e. an earlier onset of the polar night. The Antarctic experiences relatively similar insolation anomalies, but the insolation increase is during austral spring and the decrease during austral summer. From a

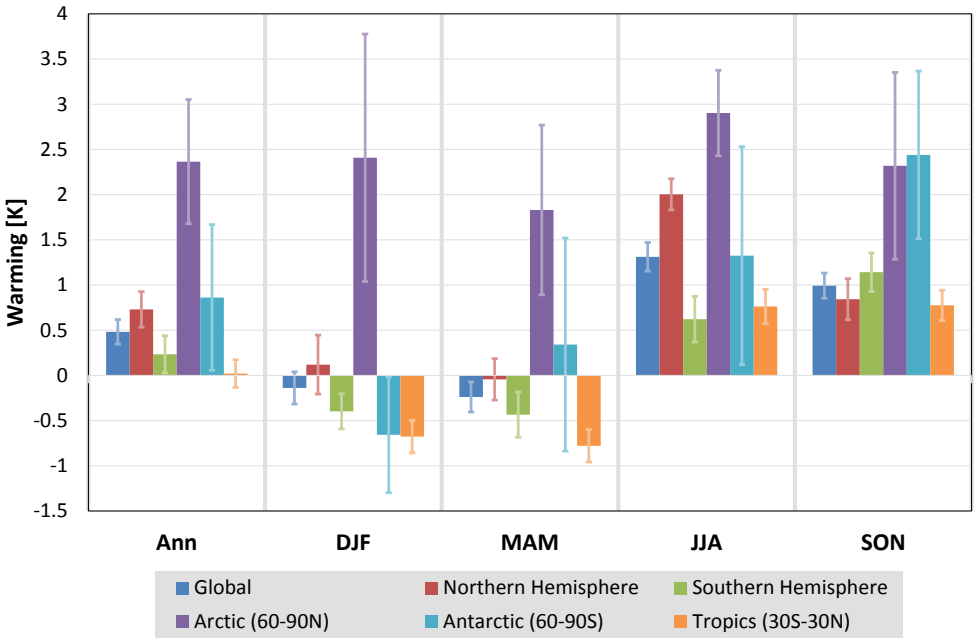

Figure 3.3: Regional annual (Ann) and seasonal mean near-surface air temperature anomalies LIG – PI [K]. The regional means are calculated using area-weighting. Selected regions are [from left to right]: Global (blue), Northern Hemisphere (red), Southern Hemisphere (green), Arctic (60–90°N; purple), Antarctic (60–90°S; light blue), and tropics (30°S–30°N; orange). Error bars indicate the range $\pm\sigma$ (standard deviation).

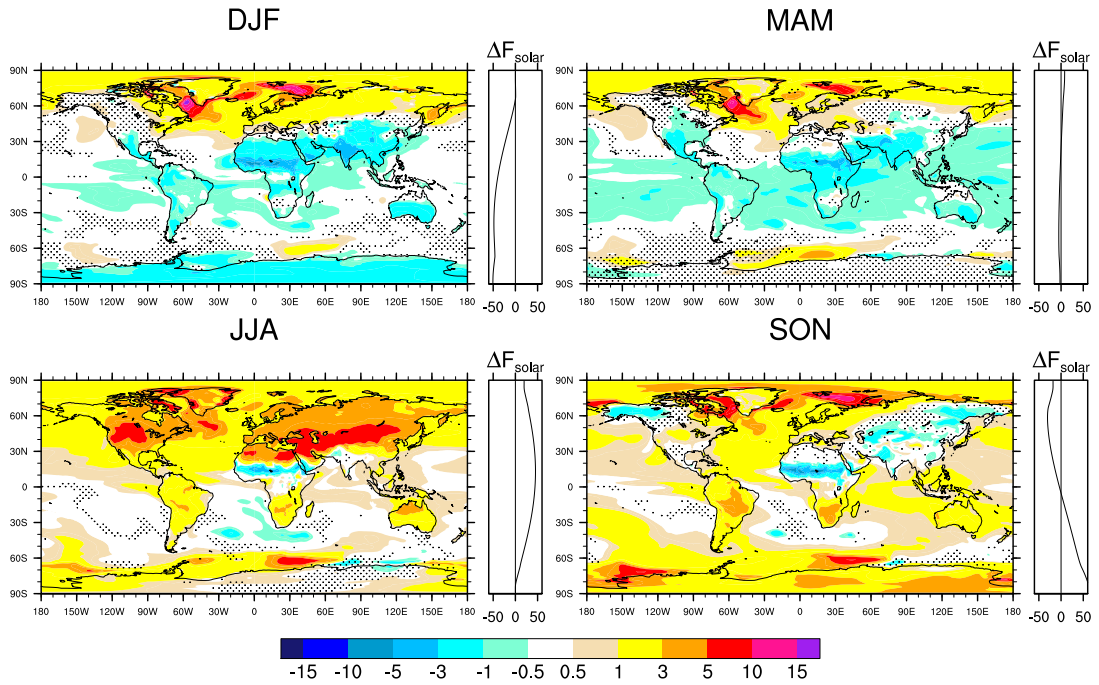

Figure 3.4: Seasonal mean near-surface air temperature anomalies LIG – PI [K]. Shading denotes changes that are not significant at the 95 % confidence level. The attached panels show the seasonal insolation anomalies [W m^{-2}]. Note the irregular spacing of the color bar.

cryospheric perspective, the insolation in the Arctic gives increased potential for summer melt and an earlier onset of the freezing period. In the same view, the Antarctic has decreased potential for summer melt, but an earlier onset of the melt period.

In accordance with the seasonal insolation differences, the sea ice response is varying between the two hemispheres (Figure 3.5). The total Antarctic sea ice extent (i.e. the area bounded by the 15 % concentration contour) is reduced throughout the year, but exhibits only a limited decrease in late austral summer and fall. The Arctic sea ice extent exhibits a very uniform decrease throughout the year (a reduction of approximately $2{\cdot}10^6$ km^2), but with a slightly larger decrease during late summer and early fall (July-September). The sea ice concentration in the central Arctic remains almost unchanged; the reduced extent is primarily due to a northward retreat of the sea ice edge.

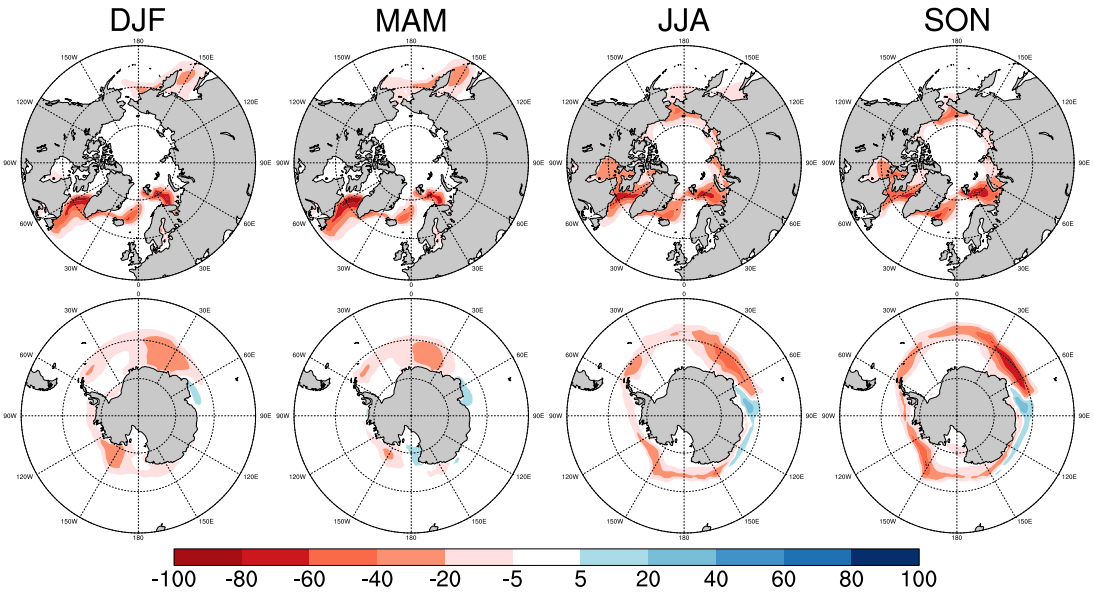

Figure 3.5: LIG seasonal sea ice concentration anomalies compared to PI [%]: Arctic (top row) and Antarctic (bottom row). Only anomalies larger than 5 % concentration change are shown.

From the warming over the high northern latitudes and Europe (Figure 3.4), it is evident that the summertime increase overwhelms the impact of the insolation reduction during fall: Despite the reduced insolation, substantial warming is seen across high northern latitudes during fall (September-October-November; SON). The continuation of warming after the summertime insolation increase is related to the increased melt of sea ice. The loss of sea ice impacts the surface energy budget by lowering the surface albedo and reducing the insulating layer between the ocean and the atmosphere (*Stroeve et al.*, 2012b). During summer, the increased insolation strengthens the impact of the surface albedo feedback, further increasing the amount of additional heat uptake by the ocean. In fall and winter, the sea ice reduction allows increased heat transfer from the ocean to the overlying atmosphere, and the heat flux is further strengthened by the anomalously warm ocean surface. The LIG experiment reveals a substantial increase of the turbulent heat flux upwards from the ocean surface during fall (SON) and winter (DJF), which peaks in the areas of sea ice loss (not shown). This combined effect of the warmer ocean and loss of sea ice causes the sustained warming through fall and winter [as

found by previous studies of Arctic sea ice loss (*Vihma*, 2014; *Pedersen et al.*, 2016a)]. *Tuenter et al.* (2005) and *Otto-Bliesner et al.* (2013) have previously shown how increased summer insolation invokes a year-round sea ice loss that contributes to Arctic warming throughout the year.

Reduction of the sea ice thickness could also lead to increased heat flux from the ocean through reduced insulation effect (*Gerdes*, 2006). However, while the sea ice thickness is substantially decreased in the Arctic in LIG, the heat flux over the sea ice covered areas is largely unchanged. Despite the large thinning, the sea ice thickness in the central Arctic remains about 2 – 4 m in LIG (4 – 6 m in PI) and thus still efficiently insulates the ocean from the atmosphere.

In the Antarctic, the mean temperature change follows the annual cycle of the insolation anomalies (Figure 3.4). Over the continent, temperatures decrease about 1 – 3 K during summer (DJF), and increase by a similar magnitude (regionally more than 3 K) during spring (SON). The Southern Ocean and Antarctic coastal seas show warming in selected regions throughout the year. The warming coincides geographically with regions of sea ice loss in all seasons except summer (cf. Figures 3.4 and 3.5) and is, again, accompanied by increases in the upward turbulent heat fluxes from the surface (not shown). The sea ice related warming does, however, only appear to have a limited impact over the Antarctic continent.

The North Atlantic region

Substantial warming is evident in the North Atlantic region throughout the year. Part of this warming is related to the northward retreat of the sea ice edge (Figure 3.5) described above, and increased absorption of incoming sunlight during summer. Additionally, the maximum strength of the Atlantic Meridional Overturning Circulation (AMOC) is increased in LIG compared to PI, increasing the heat transport toward the North Atlantic; especially in the colder seasons when deep convection is active. The maximum annual mean overturning strength increases by 37 % from 15.8 Sv in PI to 21.6 Sv in LIG (with standard deviations 1.03 and 1.27 Sv, respectively). This increase is in line with the increase of approximately 30 % found in previous, similar GCM simulations of 125 ka (*Govin et al.*, 2012; *Langebroek and Nisancioglu*, 2014).

The AMOC increase is related to increased sinking in the North Atlantic region. Using the mixed layer depth as a proxy for deep water formation, Figure 3.6 indicates that the main AMOC changes are driven by the activation of convection in the Labrador Sea, where no convection occurs in PI, and an increased sinking in the Greenland Sea (south of Svalbard). Besides the changes in the Labrador Sea, the locations of deep water formation appear unchanged, but we observe an expansion of the convection areas following the northward retreat of the sea ice edge (as indicated by the mixed layer depths). The deep water formation appears to be active from December to April with no substantial differences in the timing between PI and LIG (the northernmost areas have deepening of the mixed layer depth starting from November and ending in May).

The northward sea ice retreat in LIG also suggests decreased sea ice formation in the North Atlantic region. While the cold season sea ice formation could facilitate salinity

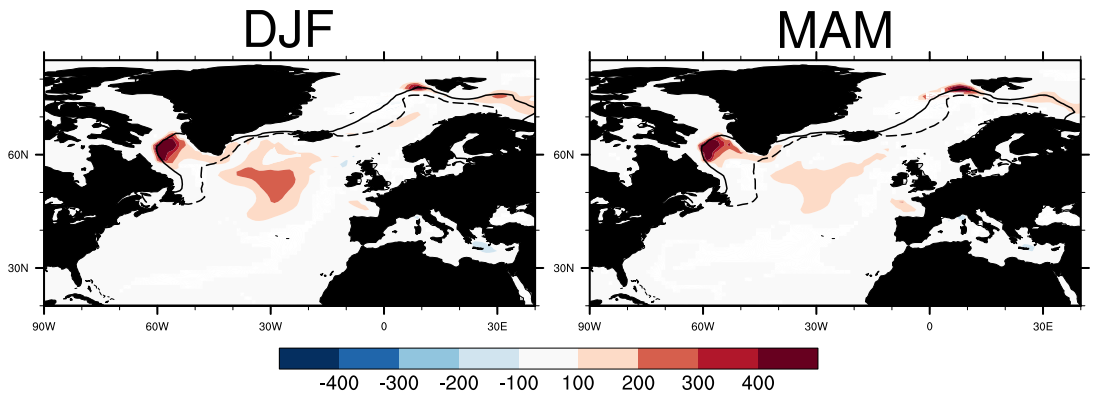

Figure 3.6: Seasonal mean mixed layer depth anomalies LIG – PI [m] for winter (DJF) and spring (MAM), when convection is active. Black contours indicate sea ice extent (15 % concentration contour): PI (dashed) and LIG (solid). Displayed changes are statistically significant at the 95 % level.

increase from brine rejection, the sea ice cover also inhibits convection by insulating the ocean from the atmosphere preventing the heat loss that drives the convection (*Blaschek et al.*, 2014). The latter effect is important in the LIG experiment where convection is activated in the Labrador Sea, where it was inhibited by sea ice in the PI experiment.

We observe a general increase of the sea surface salinity (SSS) in the LIG experiment (cf. Figure 3.13(b) in Section 3.6) that is also consistent with the increased AMOC strength; the SSS in the North Atlantic affects the water density and thereby the convection (*Kuhlbrodt et al.*, 2007). One factor affecting SSS in the North Atlantic is the sea ice export southward from the Arctic Ocean. In the LIG simulation the ice edge in the North Atlantic has retreated northward, and the changed sea ice drift indicates that the southward sea ice export through the Fram Strait and along the Greenland east coast is substantially decreased (especially in summer and fall). Sea ice export through the Fram Strait constitutes a substantial freshwater export southward from the Arctic Ocean (*Serreze et al.*, 2006), and previous studies have illustrated that the sea ice export affects the salinity in the North Atlantic, and thus the convection and AMOC strength (*Born et al.*, 2010; *Govin et al.*, 2012).

The tropics

The tropics (30°S – 30°N) experience an annual mean insolation reduction, but exhibit an almost unchanged annual mean temperature (0.02 K increase, cf. Figure 3.3). Some tropical regions exhibit substantial cooling even in seasons without reduced insolation (cf. Figure 3.4), namely the sub-Saharan/Sahel region in Africa and, to lesser extent, India and parts of southeast Asia. The cooling effect is due to changes in cloudiness and precipitation related to the monsoonal systems.

The North African monsoon has previously been shown to be sensitive to insolation changes (*de Noblet et al.*, 1996; *Braconnot et al.*, 2008; *Govin et al.*, 2014; *Bosmans et al.*, 2015). Specifically, the strength of the summer monsoon is increasing with anomalous high northern hemisphere summertime insolation (e.g. during LIG). The proposed mechanism (*Braconnot et al.*, 2008; *Bosmans et al.*, 2015) is that warming of the con-

tinents (by insolation during summer) increases ocean-land thermal and pressure gradients. The increased gradients and strengthened thermal low systems over land drive increased winds and moisture transport from the ocean to the continent. The precipitation increase is set up by a combination of increased moisture transport and local recycling (from evaporation); the latter being a minor contribution. The consequence is that the continental temperatures are expected to decrease due to increased cloud cover and evaporation (*de Noblet et al.*, 1996; *Montoya et al.*, 2000; *Bosmans et al.*, 2015). *Bosmans et al.* (2015) investigate the links between insolation changes and the North African monsoon using the previous version of the EC-Earth model. Looking at the summer (JJA) means, the authors conclude that both low precession (summer solstice near perihelion) and high obliquity strengthens the monsoon by inducing a low pressure anomaly over Northern Africa which increases winds and moisture transport from the tropical Atlantic.

Consistent with the previous studies, the summertime (JJA) precipitation (Figure 3.7) is increased substantially over the Indian and North African monsoon regions in LIG. The precipitation increase coincides with increased cloud cover (not shown) and cooling (Figure 3.4), consistent with an increased strength of the summer monsoonal systems. The total cloud fraction is increased by more than 0.2 in a broad band over the African continent covering approximately 5–25°N, and the cloud increase is seen throughout the atmospheric column (i.e. both high, mid, and low clouds are increased). The atmospheric circulation anomaly (not shown) is very similar to the response outlined by *Bosmans et al.* (2015): Sea level pressure is substantially decreased over Northern Africa, and the anomalous circulation increases the flow from the tropical Atlantic towards the interior continent south of Sahara.

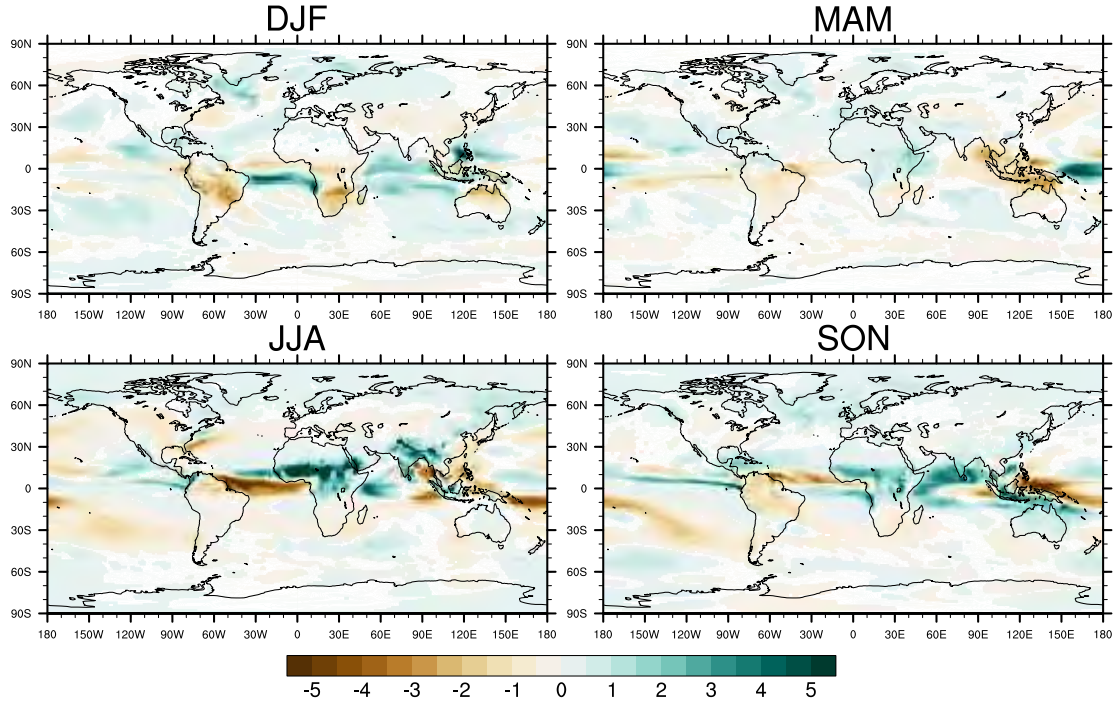

Figure 3.7: LIG seasonal mean total precipitation (sum of convective and large scale precipitation) anomalies [mm pr. day]. Displayed changes are statistically significant at the 95 % level.

The circulation anomaly is only evident during summer (JJA), while the precipitation increase remains through the fall (SON). Some of the changes related to the summer monsoon even appear to persist throughout the year: near-surface cooling, increased surface evaporation, and increased cloud cover are dominant in the region all year, albeit in varying meridional extents. The increased cloud cover means that the downwelling shortwave radiation at the surface is decreased throughout the year, regardless of the insolation anomaly (not shown). Thus, the monsoonal changes appear to affect the hydrological cycle in the region and thus the impact the climate the entire year.

3.3.2 Separation of contributions

The series of AGCM simulations is designed to investigate the mechanisms behind the simulated changes, and compare the direct and indirect effects of the insolation anomalies. Figure 3.8 displays the seasonal mean near-surface air temperature anomalies relative to iP+oP (PI conditions) in the three simulations (cf. Table 2): iL+oL (LIG conditions), iL+oP (LIG insolation, PI SST and sea ice), and iP+oL (PI insolation, LIG SST and sea ice). As desired, the temperature anomaly in iL+oL closely resembles the anomaly from the coupled experiment (compare with Figure 3.4) over ocean as well as continents. The response in iL+oP is obviously limited to the continents (and sea ice covered areas), as the near-surface air temperature over the ocean is largely determined by the prescribed SSTs. Conversely, the iP+oL experiment reveals that the changed oceanic conditions have impacts across all continents even with unchanged insolation.

The continental warming during the insolation maximum in Northern Hemisphere summer (JJA) is dominated by the direct impact of the insolation. The oceanic changes do, however, contribute to temperature increase over high northern latitudes and over Europe. The oceanic conditions appear to dominate the response over the same regions during fall and winter, where widespread warming occurs despite the lower insolation. Part of this all-year warming in the high northern latitudes, especially in the North Atlantic region including Greenland and Europe, can be ascribed to the AMOC increase and a seasonal memory of sea ice retreat [as described by *Otto-Bliesner et al.* (2013)]. In these regions, the oceanic changes more than outweigh the direct impact of the fall (SON) insolation decrease.

Over Antarctica, the reduced insolation dominates the austral summer (DJF) temperatures that decrease over the entire continent. The warming from the oceanic changes spreads over most of the continent during both winter (JJA) and spring (SON). The strongest impact is during winter, with warming of more than 1 K over the majority of East Antarctica and about 0.5 K over West Antarctica. During spring (SON) the increased insolation causes warming over the entire continent, while the oceanic changes primarily impacts the near-coastal regions in the vicinity of the sea ice loss in the Ross Sea (150°E–90°W) and east of the Weddell Sea (20°W–60°E).

Figure 3.8 indicates high resemblance between the temperature response over the tropical region in iL+oL and iL+oP (insolation only). The contribution from the oceanic changes in iP+oL is warming Northern Africa through most of the year (except MAM), while also contributing to cooling over the Sahel region (except DJF). During SON the

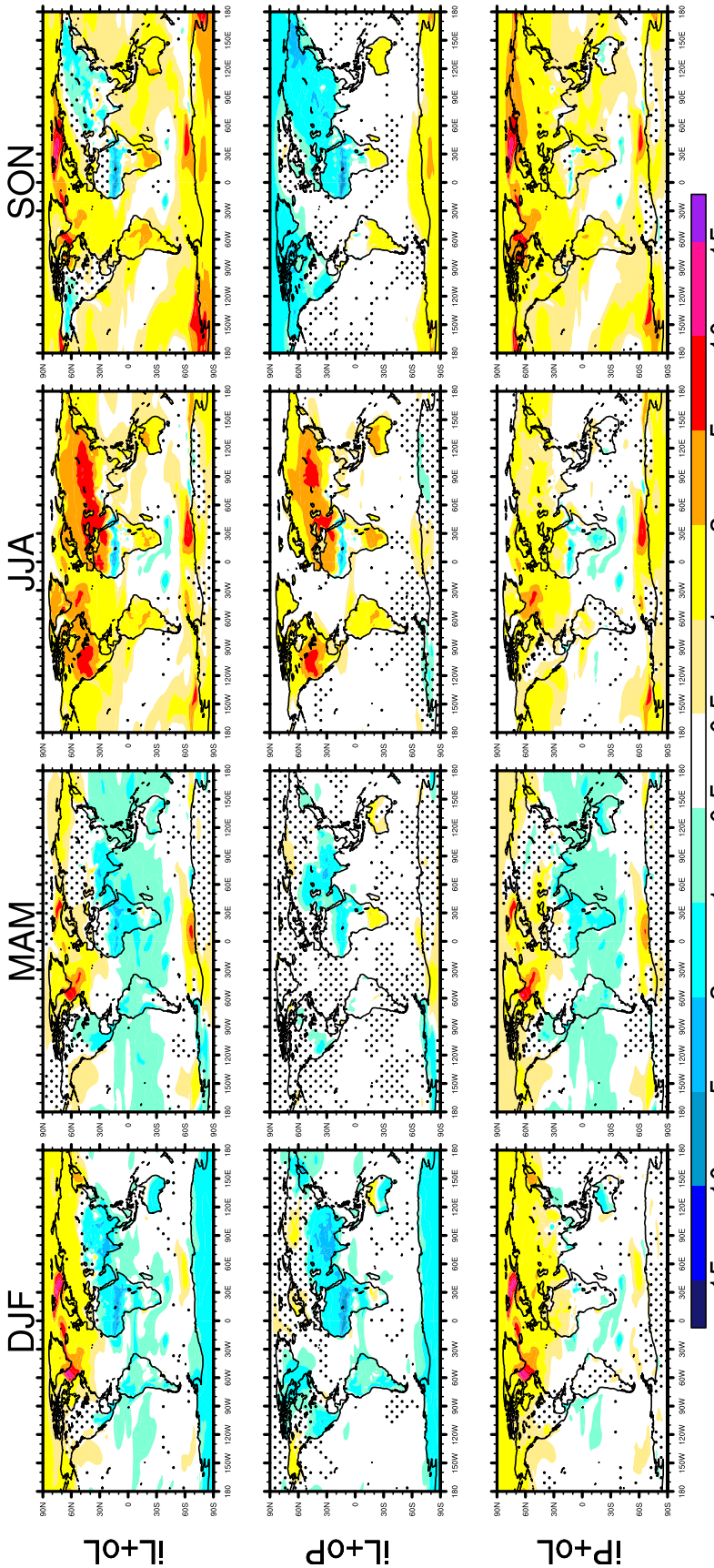

Figure 3.8: Seasonal mean warming [K] in the AGCM experiments: iL+oL (LIG conditions; top row), iL+oP (LIG insolation, PI SSTs; middle row), and iP+oL (PI insolation, LIG SSTs; bottom row). All anomalies are relative to iP+oP (PI insolation, PI SSTs). Black shading marks anomalies that are not statistically significant at the 95 % confidence level. Note the irregular spacing of the color bar.

oceanic changes in iP+oL lead to significant warming over all continents, except Northern Australia and, again, the Sahel region in Africa.

The precipitation changes reveal that both insolation and the related oceanic changes cause substantial changes in tropical precipitation patterns. Figure 3.9 shows the precipitation changes in JJA, where the seasonal anomalies over the continents are largest. As for the temperature anomalies, the precipitation anomalies in iL+oL resemble the response in the coupled simulation. The hybrid simulations reveal that while the affected areas are similar in iL+oP and iP+oL, the changes show large contrasts. Over the Indian Ocean, the insolation changes in iL+oP cause wetter conditions over the continent (India and Southeast Asia) at the expense of the near-coastal waters in the Indian and Pacific Oceans. The iP+oL simulation exhibits precipitation increase over the same ocean regions (especially in the Indian Ocean) while no substantial changes are seen over the continent. Similar results are found in this region by previous studies of the Mid-Holocene, where the oceanic changes even were found to limit the continental precipitation increase driven by insolation changes (*Liu et al.*, 2004; *Braconnot et al.*, 2007). Substantial evaporation changes over the Indian Ocean (not shown) contribute to the varying precipitation changes between iL+oP and iP+oL: The insolation change in iL+oP reduces the JJA mean evaporation in the region, while it is increased in iP+oL coincident with the higher SSTs.

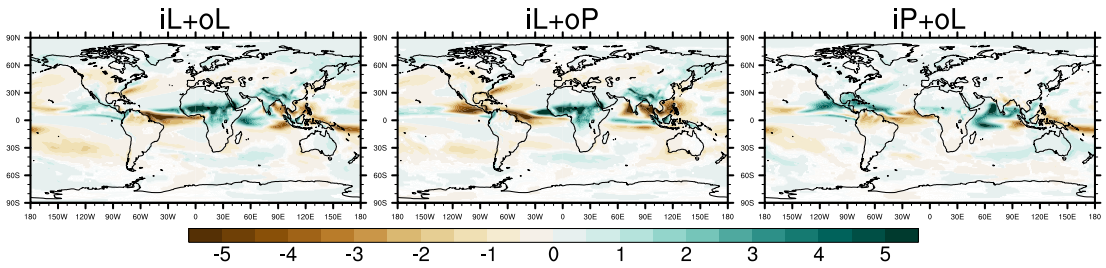

Figure 3.9: JJA mean total (convective and large-scale) precipitation anomalies [mm pr. day] relative to iP+oP: iL+oL (left), iL+oP (center), and iP+oL (right). Displayed changes are statistically significant at the 95 % confidence level.

On both the Pacific and Atlantic sides of Central America, contrasting changes are seen in iL+oP and iP+oL: The insolation changes cause decreased rainfall, while the oceanic changes alone cause a substantial increase. The result from iL+oL indicates that the combined response is close to the sum of the two, with only a slight increase on the Pacific side. In the Atlantic, similar contrasting changes are evident off the North American coast (co-located with the North Atlantic current), where the drier conditions from iL+oP dominate in iL+oL. In the tropical Atlantic both iL+oP and iP+oL show a belt of drier conditions from South America to Africa, but iL+oP also has a substantial precipitation increase off the African coast.

The strengthening of the Northern African monsoon discussed previously appears to be related directly to the insolation changes in iL+oP rather than the oceanic changes in iP+oL. Nevertheless, the oceanic changes in iP+oL do seem to contribute to the increased precipitation, albeit in smaller extent and magnitude. This is in line with the mechanism described above (suggested by *Braconnot et al.*, 2008; *Bosmans et al.*, 2015). Figure 3.10 presents the circulation changes in terms of mean sea level pressure

and 10 m winds, and reveals high resemblance between the full response in iL+oL and iL+oP. As described above, the insolation changes set up a low pressure anomaly over Northern Africa, which increases the flow and thus the moisture transport from the tropical Atlantic across the continent. These experiments indicate that the changes in Atlantic SSTs do not play a major role in shaping the monsoon response.

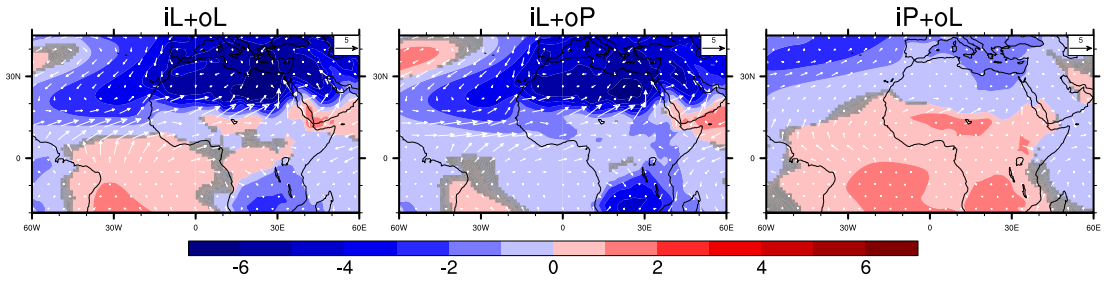

Figure 3.10: JJA mean sea level pressure anomalies [hPa] relative to iP+oP: iL+oL (left), iL+oP (center), and iP+oL (right). White arrows indicate wind (10 m) anomalies (unit vector is 5 m s^{-1}). Grey shading marks sea level pressure anomalies that are not statistically significant at the 95 % confidence level.

3.4 Comparison to proxy records

Capron et al. (2014) have compiled a collection of proxy records covering the last interglacial. While being based on a smaller number of records, it benefits from having a coherent temporal framework compared to previous compilations (*Turney and Jones*, 2010; *McKay et al.*, 2011) which assume a worldwide synchronous peak warmth. Several studies have indicated that the timing of the last interglacial warming varies substantially across the globe (*Govin et al.*, 2012; *Bakker et al.*, 2013), and that the assumption behind the data compilations contributes to the observed model-data mismatch (*Bakker and Renssen*, 2014). Thus, we have preferred this dataset for model-data comparison due to the consistent dating.

In order to compare our simulated anomalies to the proxy data reconstructions, the data from *Capron et al.* (2014) must be recalculated to account for the difference between the present-day reference climate used for the compilation (obtained from the 1998 World Ocean Atlas; WOA98) and the pre-industrial reference climate preferred here. Following the recommendations by Capron et al., we have accounted for this discrepancy by using the mean of the first 30 years of the HadISST dataset (1870-1899; *Rayner et al.*, 2003) as representative of the pre-industrial. The difference between the HadISST pre-industrial estimate and the WOA98 data has been added the proxy-derived changes.

Figure 3.11 compares simulated SST changes to the proxy data compiled by *Capron et al.* (2014). The simulated summertime (here defined as July-August-September mean [JAS] to be consistent with the proxy data) conditions in the North Atlantic exhibit more widespread warming than suggested by the proxy data. Several proxy records even suggest cooling, contrasting the overall warming in our simulations. These are found near the Norwegian Sea and in the area south of Greenland. The contrast is largest in the latter, where our simulations suggest substantial warming locally more

than 5 K. The warming during summer is resulting from increased insolation during the earlier summer (in May, June, and July; cf. Figure 3.1), increased shortwave absorption due to sea ice loss, and the AMOC increase.

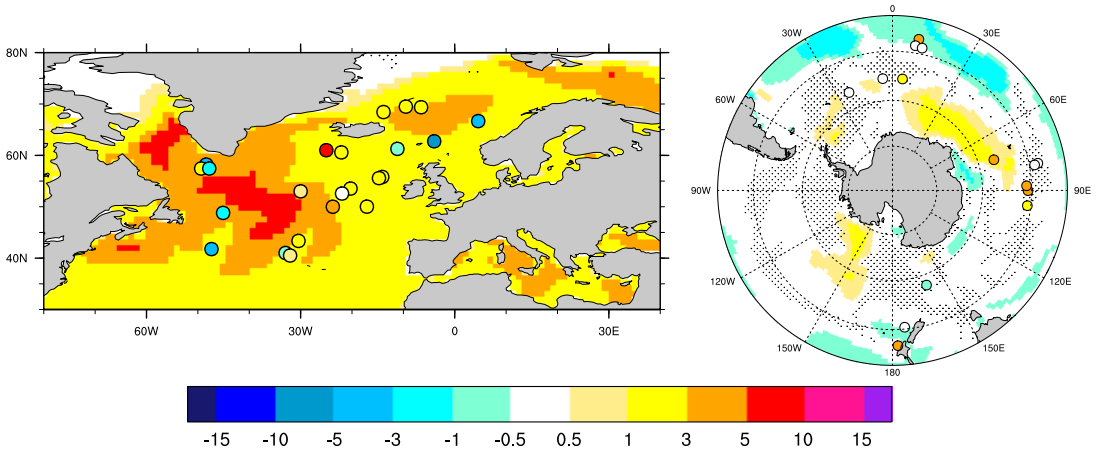

Figure 3.11: LIG SST anomalies [K] compared to temperature reconstructions compiled by *Capron et al.* (2014). Left: North Atlantic region summer (JAS) anomalies; Right: Antarctic region summer (JFM) anomalies. Black shading denotes anomalies that are not significant at the 95 % confidence level. Note the irregular color bar. Location of overlapping records near 58°N, 48°W has been shifted slightly to make all records visible.

Correlation estimates indicate that the AMOC increase contributes to widespread warming in the region, especially near the peak warming in the central North Atlantic. Linear regression coefficients between the annual mean maximum AMOC strength and the JAS SSTs in the LIG simulation (see details in Section 3.6) indicate that the region south of Greenland could warm up to 0.5 K/Sv. Based on this estimate the AMOC increase in LIG could correspond to a local increase in JJA SST of up to 3 K. The AMOC increase could, however, be overestimated, as meltwater from the expected reduction of the Greenland ice sheet would work to weaken the AMOC. In GCM simulations of the LIG (126 ka), *Govin et al.* (2012) show that the addition of meltwater from Greenland could even weaken the AMOC below the pre-industrial state. As the authors discuss, this finding is, however, an estimate of the highest potential effect of the GrIS meltwater, as the flux of 0.17 Sv is relatively high compared to the expected GrIS melt at 126 ka. Recent estimates suggest a meltwater flux of approximately 12.7 mSv at 125 ka (*van de Berg et al.*, 2011; *Blaschek et al.*, 2014). Nonetheless, previous model experiments suggest that even lower-range freshwater forcings could lead to a decreased AMOC strength (*Blaschek et al.*, 2014). The expected impact is, however, uncertain because the AMOC response is highly non-linear and has been shown to have a high sensitivity to the background climate (*Ganopolski and Rahmstorf*, 2001; *Swingedouw et al.*, 2009) and to vary between ocean models (*Stouffer et al.*, 2006; *Swingedouw et al.*, 2013).

Despite the regional differences, the majority of the proxy records suggest warming and shows fair agreement with the simulations. The magnitude of warming is within the same range as the simulated anomalies, and the highest reconstructed warming matches the highest simulated temperature anomalies. While there is substantial variability among different climate models (*Lunt et al.*, 2013), there appears to be overall agreement on

widespread warming in the North Atlantic regions; as illustrated by the multi-model annual mean presented in the latest IPCC report (*Masson-Delmotte et al.*, 2013).

The relatively large range between the proxies in the North Atlantic and Nordic Seas thus appear to be inconsistent with most modeling estimates, but previous studies have suggested that changes in the ocean circulation could explain these contrasting temperature trends (*Bauch et al.*, 2012). *Langebroek and Nisancioglu* (2014) find regional cooling without addition of freshwater (using the NorESM model). Their simulations exhibit cooling during summer both in the central North Atlantic, related to an expansion of the subpolar gyre, and in the Norwegian Sea, due to reduced inflow of warm Atlantic water into the Nordic Seas. Hence, both the lack of freshwater forcing and the characteristics of the ocean model potentially contribute to the regional model-data mismatch in the North Atlantic.

In the Southern Hemisphere during austral summer (defined as January-February-March [JFM] to be consistent with the proxy records) the proxy records with the highest warming lie beyond the range simulated in the region. The grouping of warm proxy reconstructions near the Davis Sea could be related to sea ice changes resembling the simulated warming west of these records. None of the proxies seem to agree with the cooling areas simulated in the northern part of the domain in Figure 3.11. The insolation is decreased near Antarctica during austral summer and cannot directly explain the warming suggested by both proxies and simulations. Our simulations indicate that sea ice changes, originating from increased melt during the insolation increase in spring (SON), is a potential source of warming. Some of the proxy records suggesting warming are, however, likely located too far north to be directly related to sea ice changes.

As these experiments are idealized simulations, the limitations should be considered when interpreting the results. Noteworthy caveats are that the ice sheets and the vegetation are kept constant in our experiments. In line with the estimated 6 – 9 meters sea level height increase (*Kopp et al.*, 2009; *Dutton and Lambeck*, 2012; *Masson-Delmotte et al.*, 2013; *Dutton et al.*, 2015), the ice sheets must have been reduced compared to the present extent. The reconstruction of the Greenland and Antarctic ice sheets do, however, reveal large variability between different studies (*Masson-Delmotte et al.*, 2013). Depending on the exact changes, the reduced ice sheets could impact climate locally and potentially affect the large scale atmospheric circulation and thereby also the ocean circulation (*Lunt et al.*, 2004; *Petersen et al.*, 2004; *Davini et al.*, 2015). *Merz et al.* (2014b), however, find a very stable response of the large-scale circulation in their AGCM simulations with a variety of last interglacial Greenland ice sheet reconstructions.

Another effect of the expected melting of continental ice sheets is an increased freshwater flux into the adjacent oceans. As discussed, freshwater forcing could impact ocean circulation and thus modify the climate response; especially in regions that are sensitive to changes in the overturning circulation (i.e. the North Atlantic region).

In the warmer climate during the last interglacial, several studies indicate substantial changes of the vegetation: Poleward migration of the vegetation in the Northern Hemisphere and increased vegetation in the monsoonal regions are found in both proxy data and model simulations (*Harrison et al.*, 1995; *Lozhkin and Anderson*, 1995; *Edwards et al.*, 2003; *Schurgers et al.*, 2007; *Nikolova et al.*, 2013). At high northern latitudes, the expected vegetation changes could favor additional warming by increasing the green-

house effect (*Swann et al.*, 2010) and lowering the surface albedo in snow covered areas (*Betts and Ball*, 1997).

3.5 Conclusion

The EC-Earth coupled GCM simulation of the last interglacial climate exhibits an annual mean near-surface warming of 0.5 K compared to pre-industrial conditions. Our simulations at higher resolution thus exhibit an annual mean change in the high end of the ensemble of previous LIG simulations (*Masson-Delmotte et al.*, 2013; *Lunt et al.*, 2013). In agreement with previous studies, the temperature change over the continents follow the annual cycle of the insolation changes, but we find important regional exceptions: (1) the monsoonal regions in Africa and India exhibit cooling throughout the year, and (2) Greenland, Europe, and the Northern part of Asia exhibit warming throughout the year.

The simulated temperature shows fair agreement with the marine proxy records from *Capron et al.* (2014). While the exact geographical distribution is different, the magnitude of warming in the different regions matches that of the proxy records. One key exception is the reconstructed cooling in parts of the North Atlantic; our simulations suggest dominant warming throughout the region. These discrepancies could be related to the potential overestimate of the AMOC due to lack of freshwater forcing from ice sheet meltwater. Alternatively, this particular ocean model may misrepresent the circulation changes behind the warming.

The results of the AGCM experiments illustrate the importance of the oceanic changes (sea ice and sea surface temperature changes) for the year-round warming over high northern latitudes and Europe. Comparing the two hybrid simulations, the oceanic conditions dominate the response at high latitudes, while the direct insolation impact dominates at lower latitudes.

Our results indicate that warming patterns in both the North Atlantic and the Southern Ocean are closely related to sea ice changes. Sea ice patterns different from this particular model realization would thus change the warming patterns accordingly. As maximum warming appears to coincide with regions of sea ice loss, our simulations would suggest that sea ice changes occurred near the proxy data locations with stronger warming.

The North African and Indian summer monsoons are intensified during LIG, and consequent increases in cloud cover and evaporation contribute to year-round cooling in both regions; even during times of increased insolation. The AGCM experiments show the importance of the insolation change over land relative to the oceanic changes. Our experiments demonstrate that the monsoon intensification is related to large-scale circulation anomalies similar to results from previous studies (*Braconnot et al.*, 2008; *Bosmans et al.*, 2015). The hybrid AGCM experiments (iL+oP and iP+oL) yield contrasting precipitation changes in the tropics; the combined response in iL+oL closely resembles the sum of the two.

3.6 Supplementary analysis: Arctic sea ice and ocean circulation response

The following section presents additional details on the ocean response in the fully coupled EC-Earth experiment (LIG). As discussed above, the pronounced differences between the ocean state in LIG and PI is likely affected by model biases. This encourages a closer look at potential causes and impacts of the ocean circulation changes.

The lack of Labrador Sea deep convection in the PI pre-industrial climate is likely due to model biases. This analysis cannot reveal whether the overestimated sea ice extent (*Davini et al.*, 2014) is preventing the convection, or if the lack of convection is contributing to cooling and sea ice growth in the region. While active since the early part of the current interglacial (*Hillaire-Marcel et al.*, 2001; *Solignac et al.*, 2004), it is less certain whether the Labrador deep convection was active during the Eemian. Proxy data from marine sediment cores can be used to reconstruct the circulation patterns, but unfortunately there is some conflicting findings in this region. *Hillaire-Marcel et al.* (2001) question whether the Labrador Sea convection was active during the last interglacial, but *Rasmussen et al.* (2003) conclude the convection was active throughout the peak of the Eemian and that the circulation was comparable to modern conditions. A third study by *Winsor et al.* (2012) find signs of reduced convection strength; at least during the early LIG.

The Arctic sea ice in the PI simulation is not only expanded locally in the Labrador Sea, but has an overall large extent and volume. The ice thickness, presented as seasonal means in Figure 3.12(a), is reaching 5–7 m in the central Arctic. While the sea ice thickness is poorly constrained before the modern epoch, submarine data from the middle of the 20th century suggests that the ice thickness did not exceed 4 m (*Kwok and Rothrock*, 2009). Hence, the model is likely simulating an excessive sea ice thickness in PI. In their analysis of the sea ice thickness in the CMIP5 model ensemble, *Stroeve et al.* (2014) show that the sea ice thickness in (the previous version of) EC-Earth is in the high end of the CMIP5 ensemble.

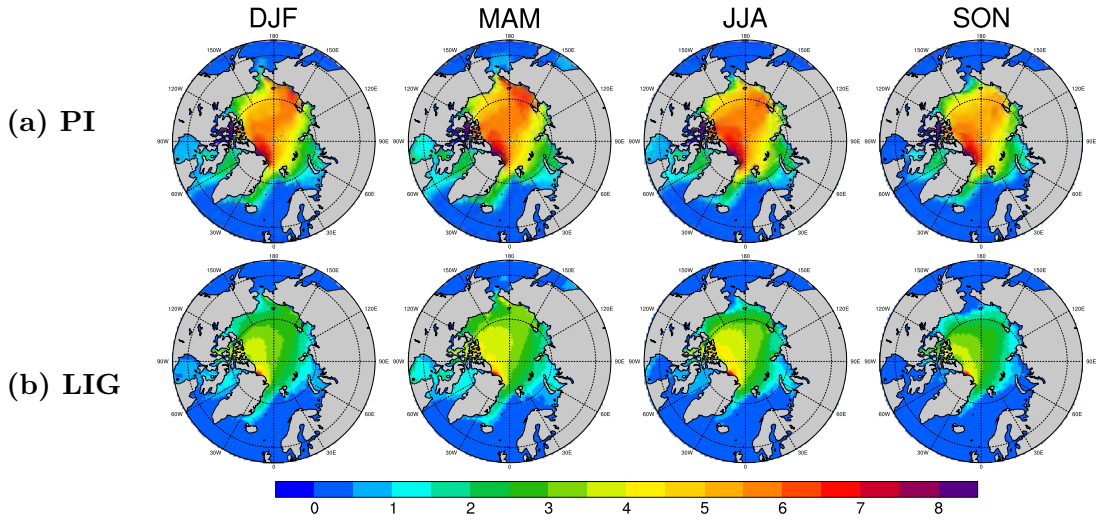

Figure 3.12: Arctic sea ice thickness [m] in (a) PI and (b) LIG.

Although reduced by several meters, the largest LIG sea ice thickness in the central Arctic remains up to 4 m. Thus, this simulation suggests that Eemian Arctic sea ice thickness was slightly larger than present-day conditions: Current observations suggest that the sea ice thickness only exceeds 3 m in region north of Greenland and the Canadian archipelago (e.g. ICEsat, IceBridge, and Cryosat; cf. *Stroeve et al.*, 2014). In their analysis of the CMIP3 model ensemble, *Holland et al.* (2010) find that the models with initially thicker sea ice generally retain a larger summer sea ice extent in projections through the 21st century. The model ensemble further indicates a stabilizing effect of thick sea ice regions. Thus, the relatively high sea ice thickness produced by EC-Earth could cause the Arctic sea ice cover to be more persistent to the Eemian forcing, potentially limiting the simulated sea ice retreat. The large thickness also means that the sea ice cover is more stable from a dynamical point of view: a thicker ice cover is less sensitive to reduction and compaction driven by changed winds and currents (*Maslanik et al.*, 2007).

The knowledge of the Arctic sea ice cover during the last interglacial is unfortunately very limited. Marine sediment cores can be used to reconstruct local sea ice conditions, but so far this has only been possible with a few Arctic cores. *Nørgaard-Pedersen et al.* (2007) analyze a marine sediment record from the central Arctic Ocean (84.5°N, 74°W, north of Greenland and the Canadian archipelago). While this region is currently characterized by the thickest, oldest ice in the Arctic, the paleo-reconstruction indicates reduced sea ice concentration during the Eemian. The record cannot reveal whether the reduction is a general regional sea ice reduction or a local, polynya-like feature. *Adler et al.* (2009) study a marine sediment record from the opposite site of the Arctic Ocean (79°N, 172°W, north of Siberia/Alaska) and find similar indications of low sea ice concentration; potentially reflecting seasonally ice free conditions. Compared to these proxy records, our simulations suggest a much higher sea ice concentration in the central Arctic. In fact, the sea ice concentration remains above 90 % throughout the year in the vicinity of the two marine sediment cores (not shown). Furthermore, these regions also exhibit a relatively high sea ice thickness (cf. Figure 3.12).

The simulated LIG Arctic sea ice extent has the most pronounced reduction in the North Atlantic region, where the sea ice edge is shifted northwards throughout the year (Figure 3.5). The sea ice response can impact the ocean circulation in two ways. First, sea ice formation causes brine rejection which increases local salinity where the ice is forming. With the warming, the sea ice formation shifts northward potentially changing the salinity distributions. A second effect is that the retreat is accompanied by a reduction of the sea ice export into the North Atlantic. Figure 3.13(a) depicts the sea ice drift anomalies in LIG compared to PI, and indicates decreased export along the Greenland east coast through most of the year.

As the sea ice export constitutes a freshwater input to the North Atlantic (*Serreze et al.*, 2006), the reduced transport is expected to cause increased sea surface salinity (SSS) in the region. Although some North Atlantic regions have a decreased salinity input from sea ice formation, the effect of the decreased export appears dominant: Figure 3.13(b) reveals a widespread SSS increase. The salinity increase could affect ocean circulation in the region, in particular the convection in the deepwater formation areas in the Labrador and Nordic Seas. It is, however, important to note the positive feedback mechanism acting between the convection and the North Atlantic salinity (originally proposed by

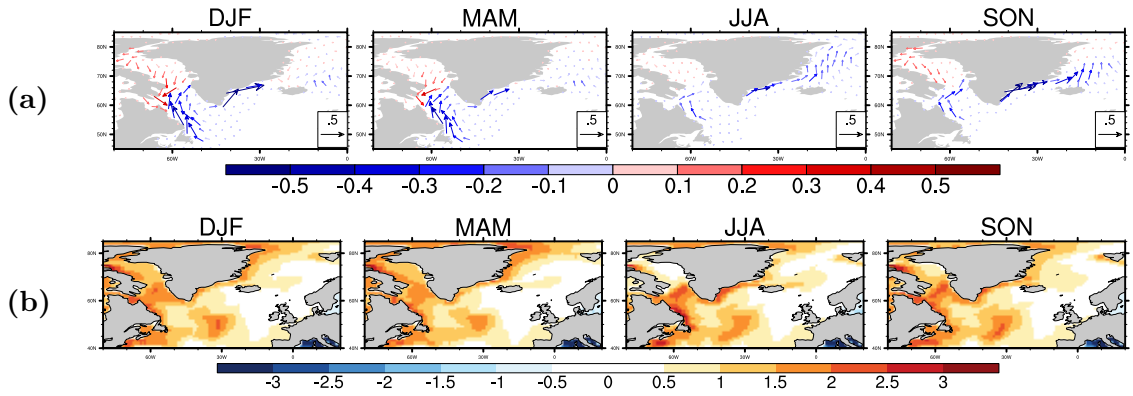

Figure 3.13: Seasonal mean (a) sea ice drift [km hr^{-1}] and (b) sea surface salinity [psu] anomalies in LIG compared to PI.

Stommel, 1961): The sea surface salinity affects the convection, which itself drives the circulation that brings saline water into the region. Hence, the increased AMOC would also favor increased salinity in the North Atlantic region, making it difficult to assess the causality pattern.

Previous studies have reported how the reduced sea ice export during the Eemian is linked to the North Atlantic ocean circulation. *Born et al.* (2010) and *Govin et al.* (2012) both simulate increased North Atlantic salinity related to decreased sea ice export. Similar to our results, they observe increased convection and increased strength of the sub-polar gyre that both contribute an increased AMOC. As illustrated by previous studies, the Labrador Sea convection and the sub-polar gyre strength are linked and act as a positive feedback in response to sea-ice-related buoyancy changes (e.g. *Born et al.*, 2010). Other modelling studies of the Eemian, however, find an unchanged or decreased AMOC at 125 ka (*Khodri et al.*, 2003; *Otterå and Drange*, 2004; *Gröger et al.*, 2007), again illustrating that the AMOC behavior varies substantially between GCMs. Figures 3.14 and 3.15 compares the AMOC strengths in our experiments PI and LIG, illustrating the substantial increase in LIG (annual mean maximum strength is increased by 37%, as noted in Section 3.3).

Unfortunately, neither proxy data nor previous modelling efforts can provide any certain conclusions on the AMOC and deep convection strength during the Eemian that we can use to assess the simulated response. This motivates further assessment of the impact of the simulated AMOC increase; a motivation which is strengthened by the potential deep convection bias in the control climate (PI). Thus, we seek to assess how the AMOC response impacts the North Atlantic SSTs that are the basis for our model-data comparison (Section 3.4).

Based on the full LIG ensemble, we have calculated the correlation between the annual mean maximum AMOC strength and the North Atlantic SST in each grid point; the result is shown in Figure 3.16. The correlation estimate for each grid cell is based on Pearson linear cross-correlation calculated as (e.g. *von Storch and Zwiers*, 2001):

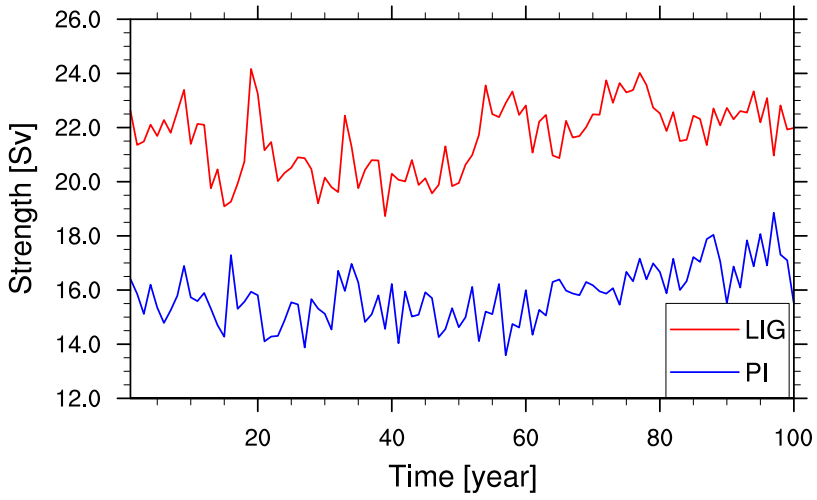

Figure 3.14: Annual maximum AMOC strength [Sv] in PI (blue) and LIG (red) for the full 100-year ensembles.

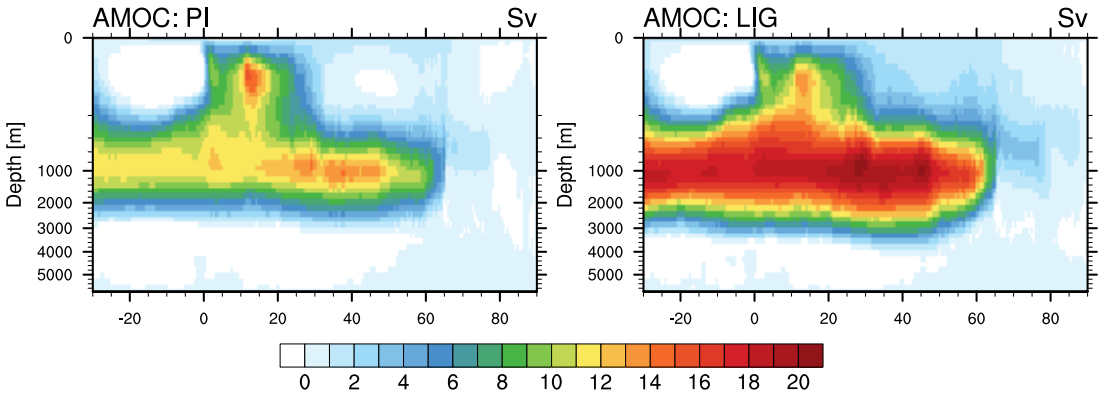

Figure 3.15: Annual mean AMOC [Sv] calculated using streamfunctions: PI (left) and LIG (right).

$$c_{\mathrm{SST,AMOC}} = \frac{\sum_t \left(T_{\mathrm{SST}}(t) - \mu_{\mathrm{SST}}\right)\left(\psi_{\mathrm{AMOC,max}}(t) - \mu_{\mathrm{AMOC,max}}\right)}{\sigma_{\mathrm{SST}} \quad \sigma_{\mathrm{AMOC,max}}} \tag{3.1}$$

where c is the correlation coefficient, t the time step, T_{SST} the SST, $\psi_{\mathrm{AMOC,max}}$ the AMOC strength, and μ and σ denotes the mean and standard deviation of the two time series.

Figure 3.16 depicts a large region south of Greenland and minor regions in the Baffin Bay and the Nordic Seas with correlations around 0.5. Interpreting these highest values as an indicator of warming associated with the increased AMOC strength, we now attempt to quantify the impact of the AMOC by calculating least-squares linear regression coefficients between the maximum AMOC time series and the JAS SST time series. This yields estimates regression coefficients with units [K Sv^{-1}] for each grid cell as shown in Figure 3.16.

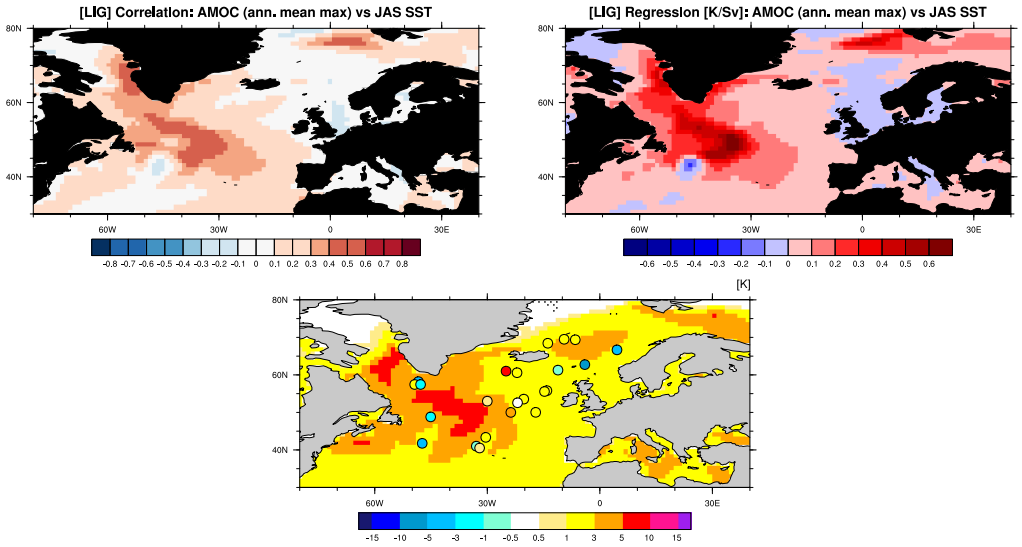

Figure 3.16: Correlation (top, left) and regression (top, right) between annual mean maximum AMOC strength and North Atlantic summertime (JAS) SST in LIG. Bottom: JAS SST anomalies in LIG compared to PI and temperature reconstructions from *Capron et al.* (2014) (identical to Figure 3.11).

As mentioned in Section 3.4 the areas of high correlation yield regression coefficient around 0.5 K Sv^{-1}, equivalent to local increases in JJA SST of up to 3 K. If the AMOC increase should be disregarded as a model artifact, these estimates thus indicate that the warming in the central North Atlantic and the Labrador Sea/Baffin Bay areas could be reduced by up to 3 K, making the North Atlantic warming slightly more uniform. Assuming that we can account for the isolated the impact of the AMOC increase in this manner, our model results would still suggest widespread North Atlantic warming. This estimate indicates that even without an AMOC increase, the model would not replicate any of the regional cooling patterns suggested by some proxy records. This particular model appears not to favor the ocean circulation anomalies that cause the contrasting temperature trends in the North Atlantic regions suggested by some proxy records and modelling studies (*Bauch et al.*, 2012; *Capron et al.*, 2014; *Langebroek and Nisancioglu*, 2014).

3.7 Isolated impact of sea ice loss

While we already separated the direct impact from insolation and the indirect impact of changed sea surface conditions, it would be interesting to further disentangle the different sources ocean-related warming. Thus, we will investigate the isolated impact of sea ice loss in the context of these last interglacial experiments. Here, we will in a simpler manner illustrate the role of the LIG sea ice loss – and the challenges related to isolating its impact in GCM experiments.

For this purpose, we have designed a third hybrid experiment in the AGCM setup ("iP+oP-ice") forced by pre-industrial insolation and pre-industrial SSTs combined with Eemian sea ice concentrations. As a conservative approach, the SSTs are kept at the freezing point (−1.8°C) where the sea ice is removed. In similar AGCM studies of sea ice loss, there is an ongoing debate on how to design the SST fields to best capture the full

warming impact of sea ice loss (cf. Section 2.2). As further discussed in Chapter 5, we argue that traditional AGCM studies can, in fact, not completely isolate the response to sea ice loss. The AGCM iP+oP-ice simulation described here illustrates some of the issues related to these traditional setups with fixed SSTs.

Figure 3.17 compares the near-surface temperature anomalies in iP+oL and iP+oP-ice, revealing that the sea ice changes primarily drive a substantial local warming response.

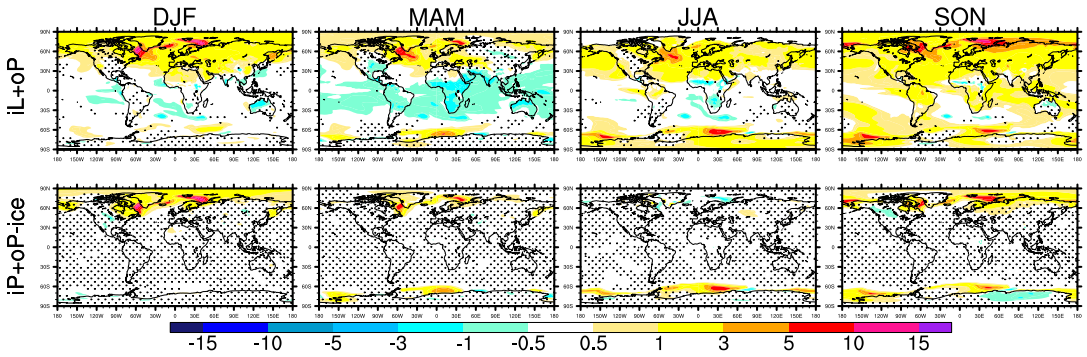

Figure 3.17: Seasonal mean near-surface warming in iP+oL (top) adn iP+oP-ice (bottom) compared to iP+oP. Black dotted shading indicates changes are not statistically significant at the 95 % level.

The temperature response is largely limited to the areas of sea ice loss, i.e. confined to the marginal areas (cf. Figure 3.5). An exception occurs during fall and winter where a more widespread Arctic warming is simulated. As the ice thickness is fixed in these simulations and no substantial concentration changes occur in the Arctic Ocean, the widespread warming indicates that warming is advected from the ice loss regions. This is also manifested in the warming over Greenland. During winter (DJF) iP+oP-ice indicates that a substantial contribution to Greenland warming is related directly to the sea ice retreat (further discussed in Section 4.6).

During summer (JJA in the Arctic, DJF in the Antarctic) there is no temperature response to the sea ice loss in iP+oP-ice. This is a direct consequence of the experiment design. In summer, the most dominant impact of sea ice loss is an albedo feedback that favors increased absorption of solar radiation that drives accelerated melt. As the SST is fixed, this effect is not captured in this setup. The impact of sea ice loss in this setup is most pronounced during winter, where the cold sea ice surface is replaced by the relatively warmer ocean surface.

Large-scale atmospheric circulation changes are, however, largely absent in iP+oP-ice (not shown). This is also reflected in the general lack of warming beyond the regions of sea ice loss (Figure 3.17). We expect that the sea ice loss in itself could cause circulation changes that would lead to a more widespread geographical impact. These changes are, however, likely inhibited by the fixed SST conditions; Chapter 5 presents a more detailed discussion of this issue.

4 Greenland warming during the last interglacial: the relative importance of insolation and oceanic changes

Building on the previous one, this chapter presents a closer look at Greenland in the LIG simulations. The AGCM experiments are analyzed with special focus on the potential changes to the ice sheet mass balance and the ice core records. By separating the impacts of the insolation and the ambient warming, this study assesses whether the Eemian climate could serve as an analogue for future changes over the Greenland ice sheet.

This chapter is based on *Pedersen et al.* (2016c) which is included in its full extent. Again, parts of the scientific introduction is repeated to ensure a consistent presentation of the study. Supplementary sections are added at the end of the chapter, presenting additional details on the changes on the ice sheet surface and the atmospheric circulation near Greenland.

4.1 Introduction

The last interglacial, the Eemian, was characterized by higher than present temperatures in the Arctic region driven by increased summertime insolation at high northern latitudes (*CAPE-Last Interglacial Project Members*, 2006; *Masson-Delmotte et al.*, 2013). The recent NEEM ice core from northwestern Greenland covers the last interglacial period and indicates substantial warming from 129–114 thousand years before present (ka) peaking at 8±4 K above the mean of the last millennium (*NEEM community members*, 2013). This temperature estimate is based on stable water isotopes, specifically δ^{18}O, using the temperature–isotope relation from the present interglacial (*Vinther et al.*, 2009). A recent, alternate reconstruction based on isotopic air composition (δ^{15}N) from the same ice core yields a very similar estimate of 7–11 K, with 8 K as the most likely estimate (*Landais et al.*, 2016). General circulation models, however, generally simulate a much more limited warming (*Braconnot et al.*, 2012; *Lunt et al.*, 2013; *Masson-Delmotte et al.*,

2013; *Otto-Bliesner et al.*, 2013), motivating further investigation of the mechanisms behind the Eemian warming in Greenland.

During the Eemian, the global sea level was increased 6–9 m above present (*Dutton and Lambeck*, 2012; *Dutton et al.*, 2015; *Kopp et al.*, 2009), indicating a substantial reduction of the continental ice sheets. Several studies have presented ice sheet model reconstructions of the Greenland ice sheet (GrIS), but the reconstructions vary substantially in both magnitude and spatial distribution of the ice sheet changes. Regarding the magnitude, the ensemble of reconstructions suggests a likely range of sea level contribution from GrIS of 1.4–4.3 m (*Masson-Delmotte et al.*, 2013). Spatially, the potential changes as suggested by the various models are retreat in southwest (*Helsen et al.*, 2013), retreat in north- and southwest with a separate South Dome ice cap (*Robinson et al.*, 2011), retreat in southwest and north-northeast (*Born and Nisancioglu*, 2012; *Quiquet et al.*, 2013; *Stone et al.*, 2013), and complete loss of the South Dome (*Cuffey and Marshall*, 2000; *Lhomme et al.*, 2005). Only very few constraints exist that can be used to assess these reconstructions. The deep Greenland ice cores that contain Eemian ice are obvious fix-points. These are NEEM (77.45°N, 51.06°W; *NEEM community members*, 2013), NGRIP (75.10°N, 42.32°W; *NGRIP members*, 2004), GRIP (72.5°N, 37.3°W; *GRIP members*, 1993) and GISP2 (72.58°N, 38.48°W; *Grootes et al.*, 1993). Additionally, basal parts of the Renland (71.3°N, 26.7°W) and Camp Century (77.2°N 61.1°W) ice cores contain ice from the Eemian (*Johnsen et al.*, 2001). The DYE-3 ice core further south (65.2°N, 43.8°W; *Dansgaard et al.*, 1982) has distorted layers making it difficult to assess the deepest part of the core (*Johnsen et al.*, 2001), but the basal part contains ice older than the Eemian (*Willerslev et al.*, 2007). Ocean sediment cores further indicate the presence of ice in southern Greenland during the Eemian (*Colville et al.*, 2011).

Due to the lapse rate (i.e. decreasing temperature with atmospheric height), elevation changes will impact the surface temperature on GrIS. While the ice core air content only suggests limited elevation changes at the NEEM site (45±350 m higher than present ice sheet elevation), the NEEM ice core temperature reconstruction has been corrected using the surface elevation change estimate from the ice core air content (*NEEM community members*, 2013). Besides the direct impact of the elevation change, changes in the GrIS topography could also impact the large scale circulation (*Hakuba et al.*, 2012; *Lunt et al.*, 2004; *Petersen et al.*, 2004), as well as the local conditions on Greenland (*Merz et al.*, 2014a) and the ice core record through changed precipitation patterns (*Merz et al.*, 2014b).

The conversion from δ^{18}O to temperature may be a contributing factor to mismatches between model simulations and δ^{18}O temperature reconstructions: The δ^{18}O–temperature relationship is sensitive to precipitation intermittency, evaporation conditions, and atmospheric transport, and thus varies spatially and historically (*Jouzel et al.*, 1997; *Masson-Delmotte et al.*, 2011). Hence, sea surface warming and reduced sea ice extent might thus affect the δ^{18}O record, as illustrated by isotope-enabled climate model simulations (*Sime et al.*, 2013). The NEEM δ^{18}O temperature estimate is based on the average Holocene δ^{18}O–temperature relationship from other central Greenland ice cores (*Vinther et al.*, 2009), but the actual relationship might be different due to the shifted location or the climatic changes during the Eemian.

One important factor to consider when interpreting ice core records is the precipitation seasonality. The ice core record reflects the snow deposition on the surface, and thus

only records climatic information during snowfall events (*Steig et al.*, 1994). The precipitation seasonality thus creates a bias towards seasons with more snow deposition, and changes in the seasonality may induce changes in the ice core record even with an unchanged temperature (*Persson et al.*, 2011). As an example, model simulations indicate that the present day climate in northwestern Greenland is biased towards summer due to precipitation seasonality (*Steen-Larsen et al.*, 2011). Thus, when comparing model simulations to ice core records it is useful to consider the precipitation-weighted temperature to obtain a fair comparison. The precipitation-weighted temperature (T_{pw}) can be calculated as:

$$T_{pw} = \frac{\sum_{j=1}^{N} T_j p_j}{\sum_{j=1}^{N} p_j} \tag{4.1}$$

where N denotes the total number of time samples, and T_j and p_j is the temperature and precipitation during the jth time sample. In our study, the weighting is based on monthly means of near surface air temperature and total precipitation.

Using a series of general circulation model (GCM) experiments, we assess the GrIS warming during the Eemian. Specifically, we aim to compare the direct impact of the insolation change and the indirect effect of retreating sea ice and increasing sea surface temperatures (SSTs). We investigate how the simulated changes could affect the GrIS surface mass balance and the ice core record, and whether the insolation or the oceanic changes dominate the total response.

The experiments and the employed models are described in Section 4.2. Results are presented and discussed in Section 4.3, followed by conclusions in Section 4.4.

4.2 Methods

4.2.1 Model configuration

The model used for this study is the EC-Earth global climate model in the most recent version 3.1 (*Hazeleger et al.*, 2010, 2012). We employ the atmosphere-only configuration based on the IFS atmospheric model (cycle 36r4, *European Centre for Medium-Range Weather Forecasts*, 2010) in a T159 spectral resolution with an associated Gaussian grid of roughly 1.125° × 1.125° horizontal resolution and 62 layers in the vertical. In order to allow paleoclimate simulation, the model has been expanded with an option to modify the insolation according to any given orbital configuration. The insolation is internally calculated following *Berger* (1978) using the same code modification as *Muschitiello et al.* (2015).

The prescribed sea surface boundary conditions (sea surface temperature and sea ice concentration) are obtained from two simulations with the fully-coupled EC-Earth system: an Eemian experiment forced with 125 ka conditions (i.e. insolation and greenhouse gas concentrations; GHGs) and a pre-industrial control experiment. The coupled experiments are described and presented in *Pedersen et al.* (2016b).

Due to the diverse ice sheet reconstructions, we have kept the ice sheets fixed at present day extents in all of our simulations. Vegetation is similarly kept at present day val-

ues, and consequently our experiments do not include any additional feedbacks from vegetation or ice sheet geometry (as discussed in *Pedersen et al.*, 2016b).

4.2.2 Surface mass balance calculations

To investigate the impacts of the simulated climate changes on the GrIS surface mass balance, we performed off-line calculations with the subsurface scheme of the HIRHAM5 regional climate model (updated from *Langen et al.*, 2015)). The subsurface model was here run on the Gaussian grid associated with the EC-Earth experiments and forced at 6 hour intervals with incoming shortwave and downward longwave radiation, latent and sensible heat fluxes, along with rain, snow and evaporation/sublimation taken directly from the EC-Earth output. The subsurface model was updated slightly compared to that described by *Langen et al.* (2015); most notably it employs 25 layers with a total depth of 70 m water equivalent and includes temperature- and pressure-dependent densification of snow and firn (following *Vionnet et al.*, 2012). It accounts for heat diffusion, vertical water transport and refreezing. Each layer can hold liquid water corresponding to 2 % of the snow pore space volume and excess water percolates downward to the next layer. When a layer density exceeds the pore close off density (830 kg m^{-3}), water percolating down from above is added to a slush layer and runs off exponentially with an exponential time scale depending on surface slope (*Lefebre et al.*, 2003; *Zuo and Oerlemans*, 1996). Until it runs off, the slush layer water is available for superimposed ice formation onto the underlying ice layer at a rate that assumes a linear temperature profile in that layer.

4.2.3 Experimental design

We have designed four experiments to investigate how the last interglacial insolation changes impacted the climatic conditions on Greenland (cf. Table 4.1). An experiment with Eemian (125 ka) conditions ("iL+oL") is compared to a pre-industrial control climate state ("iP+oP"). The simulations are forced with GHGs and insolation from the respective periods along with prescribed sea surface temperatures (SST) and sea ice concentration (SIC) obtained from fully coupled model experiments with identical GHGs and insolation. Ice sheets and vegetation are kept at pre-industrial conditions in both experiments. Aiming to disentangle the direct impact of the insolation changes and the secondary impact of changed sea surface conditions (SST and SIC), we have designed two hybrid experiments: The first experiment is forced by Eemian insolation and pre-industrial sea surface conditions ("iL+oP") and the second is conversely forced by pre-industrial insolation and Eemian sea surface conditions ("iP+oL").

During the Eemian at 125 ka the Northern Hemisphere summer solstice occurs near perihelion and the obliquity is increased compared to present day. The changed orbit causes an insolation increase over Greenland during summer compensated by a decrease during autumn, i.e. an earlier onset of the polar night (cf. Figure 4.1).

The changed insolation leads to sea ice retreat and increasing SSTs across high northern latitudes (see detailed description in *Pedersen et al.*, 2016b)). Figure 4.2 depicts the sea ice retreat and the SST anomalies from the coupled simulations, indicating the

Experiment	Insolation and GHGs	SSTs and sea ice
iP+oP	Pre-industrial	Pre-industrial
iL+oL	Eemian	Eemian
iL+oP	Eemian	Pre-industrial
iP+oL	Pre-industrial	Eemian

Table 4.1: Boundary conditions for the experiments. In the experiment names, the letter following "i" indicates the insolation conditions, while the letter following "o" indicates the oceanic conditions: "P" is PI and "L" is Eemian (Last Interglacial).

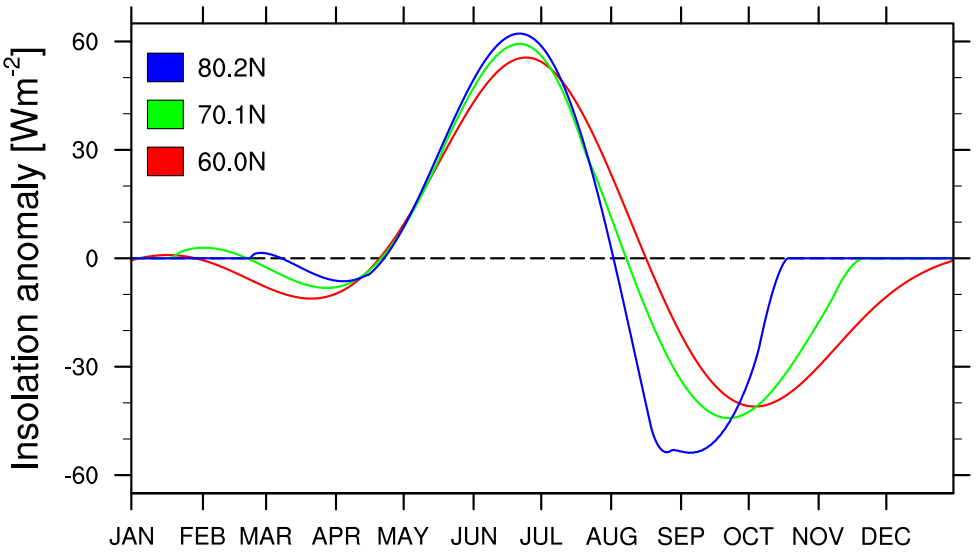

Figure 4.1: Insolation anomalies [Wm^{-2}] in Eemian relative to PI. The selected latitudes represent southern (60°N, red), middle (70°N, green), and northern (80°N, blue) Greenland. Tick marks indicate the beginning of each month.

differences between the sea surface boundary conditions. The sea ice reduction is primarily manifested as a northward retreat of the ice edge (as illustrated by the sea ice extent contours in Figure 4.2); the sea ice concentration in the central Arctic is largely unchanged (not shown).

All simulations have a total length of 60 years of which the 10 first years are disregarded as spin-up. Statistical significance of changes is assessed using a two-sided Student's t test (*von Storch and Zwiers*, 2001), taking into account the serial autocorrelation of the time series.

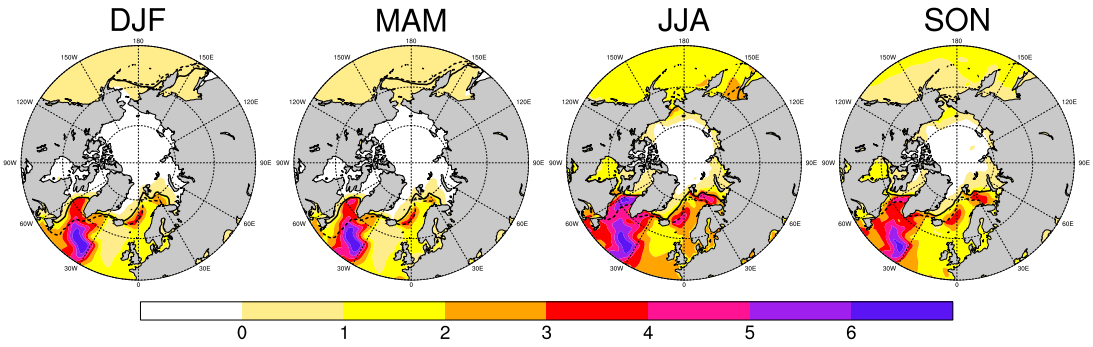

Figure 4.2: Seasonal mean SST anomalies [K] in Eemian relative to PI boundary conditions. Black contours indicate the sea ice extent (i.e. the 15 % concentration contour): PI (dashed) and Eemian (solid).

4.3 Results and Discussion

As described by *Pedersen et al.* (2016b), the anomalies between the Eemian and the pre-industrial in the atmosphere-only model configuration closely resemble those of the fully coupled experiments. Figure 4.3 shows that entire Greenland warms in all seasons in the full Eemian experiment, iL+oL. The peak warming is generally found in the coastal regions, but the central, high altitude Summit region warms more than 2 K in both summer (June-July-August; JJA) and winter (December-January-February; DJF). During summer, strong warming patches are collocated with loss of snow cover (not shown). Increased shortwave absorption and a consequent larger sensible heat flux from the surface indicates that surface albedo changes are contributing to these local warming peaks.

The hybrid simulations, iP+oL and iL+oP, exhibit very different annual cycles of warming. Following the insolation changes, iL+oP only shows warming during summer covering the entire Greenland, whereas fall (September-October-November; SON) and winter exhibit cooling; the winter cooling is limited to the southwestern part of Greenland. A small area in northwestern Greenland is warming through winter and spring (March-April-May; MAM). Again, this warming coincides with loss of snow cover, and increased sensible heat release from the surface. Continental snow cover changes can thus extend the summertime warming to the colder seasons with reduced insolation, but the iL+oP experiment indicates that this memory effect only plays a minor role for GrIS as a whole.

The oceanic changes in iP+oL cause warming over entire Greenland, peaking in the colder seasons fall and winter. Warming due to sea ice loss peaks during winter, following increased turbulent heat flux from the ocean surface where the insulating sea ice layer is lost [in agreement with previous studies of sea ice loss (*Pedersen et al.*, 2016a; *Vihma*, 2014)]. Previous studies show that the GrIS near surface temperature is sensitive to sea ice changes in its vicinity (*Pedersen et al.*, 2016a), and that ice loss in the Nordic Seas could have a larger impact than ice loss in the Labrador Sea due to an atmospheric circulation response (*Merz et al.*, 2016). Additional SST increase from ocean circulation changes and increased summertime shortwave absorption (*Pedersen et al.*, 2016b) expands the regions with positive turbulent heat flux anomalies beyond the areas of sea ice

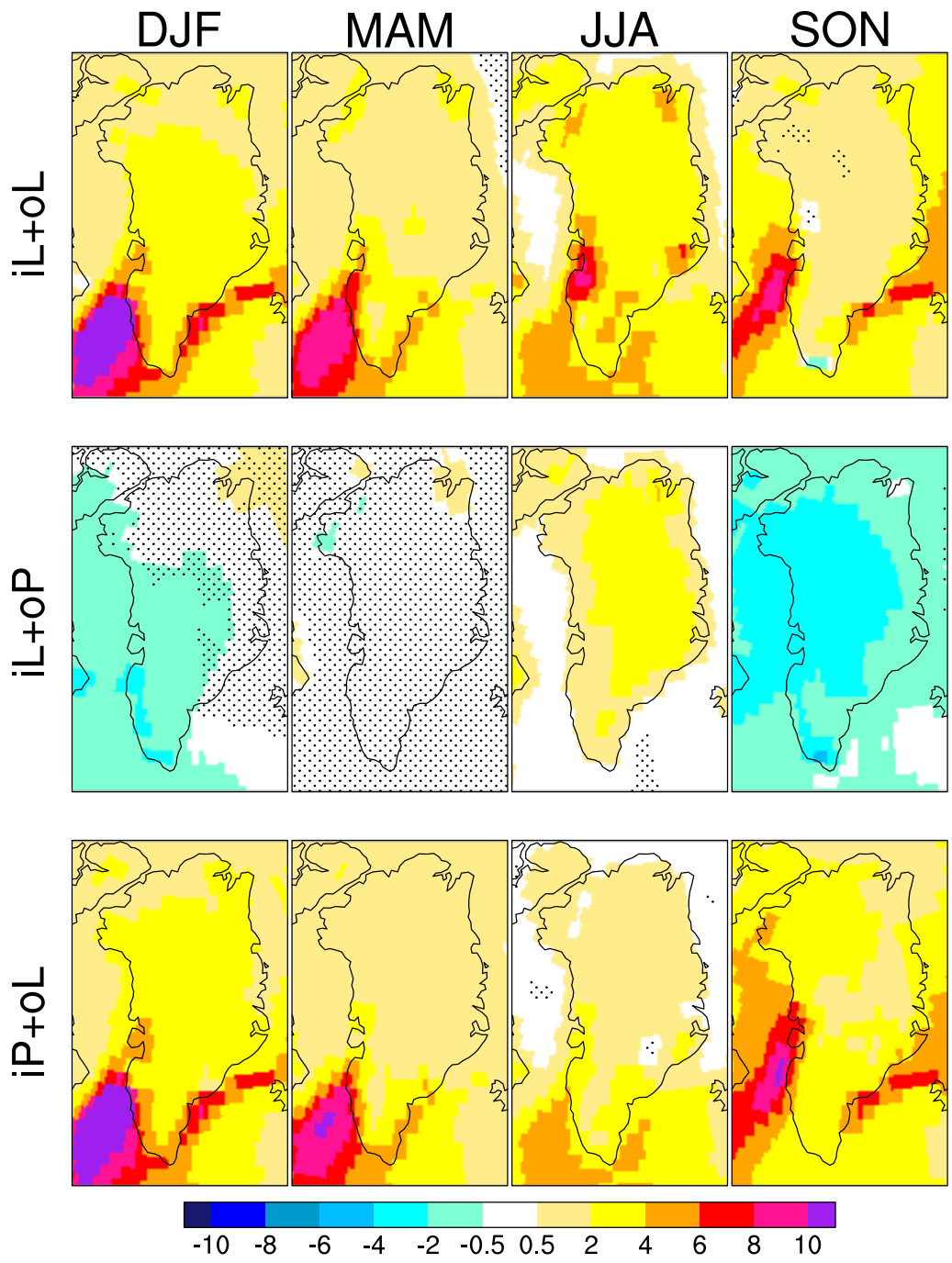

Figure 4.3: Seasonal mean near-surface temperature anomalies [K] compared to iP+oP in the three experiments: iL+oL (top), iL+oP (middle), and iP+oL (bottom). Only changes larger than ±0.5 K are shown. Black dotted shading marks anomalies that are not statistically significant at the 95 % level.

loss (not shown). The total impact of the oceanic changes thus counters the direct impact of the insolation during fall and winter, resulting in the all-year warming observed in iL+oL, which closely resembles the sum of the iP+oL and iL+oP.

Similar to the temperature, the snowfall over GrIS also exhibits varying sensitivity to the insolation and the oceanic changes (cf. Figure 4.4). The simulated responses reveal that the ice sheet topography is important for the precipitation changes: Figure 4.4 reveals several examples of contrasting snowfall changes on the east and western side of the ice divide. In iL+oL, the southern Greenland snowfall is increased throughout the year. The west coast appears drier during summer due to an increasing fraction of the precipitation falling as rain; the total precipitation is increased along the coast (not shown). The entire interior ice sheet receives more snow during summer, while the eastern (western) part have increased snowfall during fall (spring). The hybrid experiments reveal that the snowfall increase primarily is driven by the oceanic changes (cf. iP+oL). iL+oL and iP+oL have high resemblance, especially winter and spring, while the insolation appears to contribute to the snowfall increase over the interior ice sheet during summer. The fall pattern in iL+oL on the other hand indicates non-linear behavior, in that iL+oL does not resemble the sum of the two hybrid experiments: the strong increase on the western GrIS is only seen in iL+oL.

4.3.1 Precipitation-weighted temperature

The precipitation changes in Figure 4.4 suggest that the northwestern GrIS near the NEEM ice core location is affected by changed precipitation seasonality in all three simulations: the insolation in iL+oP causes increased summer snowfall and drier conditions in fall, the oceanic changes in iP+oL cause increased snowfall throughout the year, and the combination in iL+oL leads to increased snowfall during spring and summer. To assess how these changes might affect the ice core record, the precipitation-weighted annual mean temperature has been calculated following Equation (4.1); Figure 4.5 compares the annual mean temperature change and the precipitation-weighted mean.

The precipitation-weighted mean temperature (T_{pw}) in iL+oL is relatively similar to the annual mean (T_{ann}). One exception is the northwestern GrIS, where T_{pw} is higher suggesting a strong bias towards summer in the precipitation seasonality. The widespread, general precipitation increase driven by the changed oceanic conditions in iP+oL only causes minor differences between the annual and the precipitation-weighted means: The precipitation-weighting primarily affects the near-coastal regions. Conversely, iL+oP exhibits a large difference between T_{ann} and T_{pw}. The combination of wetter summer conditions and drier conditions during winter and fall in western Greenland, increases T_{pw} in a large region covering the central, west, and northwest GrIS. By comparing the hybrid simulations to the response in iL+oL, it appears that the insolation changes are responsible for the changed precipitation seasonality that causes the increased T_{pw} in the northwestern GrIS.

Due to the flow of the ice, the deposition site of the Eemian ice from the NEEM ice core is further upstream than the drilling location (approximately 76.4°N, 44.8°W, 205±20 km upstream; *NEEM community members*, 2013)). To ensure fair comparison, we consider the simulated conditions over this point (dNEEM) when comparing model results and ice core records (note, however, that the upstream correction is within two grid cells). Table 4.2 presents the annual mean and precipitation-weighted temperatures for dNEEM, revealing a varying impact between the three simulations. The iL+oL estimate is largely

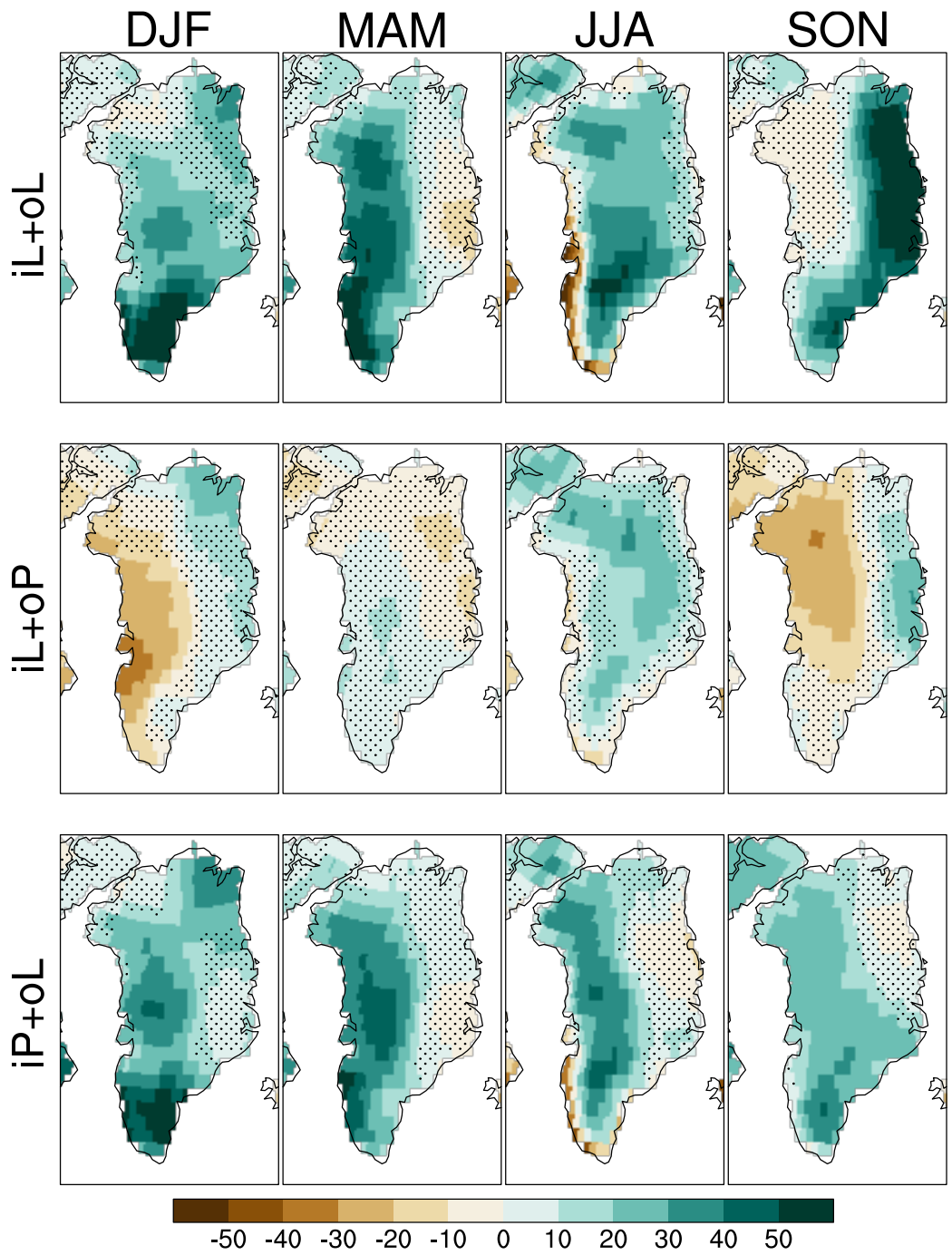

Figure 4.4: Seasonal mean relative snowfall anomalies [%] from iP+oP: iL+oL (top), iL+oP (middle), and iP+oL (bottom). Black dotted shading marks anomalies that are not statistically significant at the 95 % level.

unchanged by the precipitation-weighting, and is thus still relatively low compared to the ice core temperature reconstructions. As evident from Figure 4.5, the precipitation-weighted temperature north-northwest of dNEEM exhibits a higher increase, but the strongest does not exceed 3–4 K.

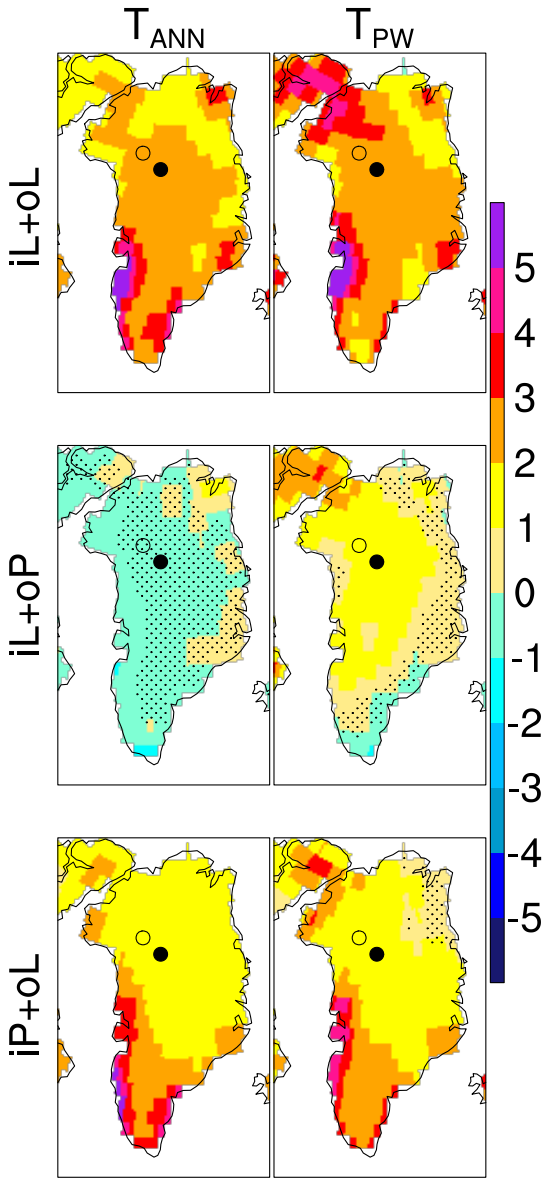

Figure 4.5: Near-surface air temperature anomalies [K] in iL+oL (top), iL+oP (mid), and iP+oL (bottom) compared to iP+oP: Annual mean (left column) and precipitation-weighted mean (right column). Black dotted shading marks anomalies that are not statistically significant at the 95 % level. dNEEM (NEEM) location is marked with the filled (hollow) black circle. Note the changed color bar compared to the seasonal means.

From the annual mean temperatures, the SST and sea ice changes (iP+oL) appear to completely dominate the temperature change at dNEEM. Taking the precipitation seasonality into account, however, reveals that the direct impact of the insolation has a comparable contribution to the warming signal recorded in the ice core.

The three experiments indicate substantial non-linearity in the responses to the changed insolation and oceanic conditions. While iP+oL indicates that SST and sea ice changes results in a warming of 1.5 K (ΔT_{pw}) at the NEEM location, the difference between

Experiment	$\Delta T_{\mathbf{ann}}$	$\sigma_{\mathbf{ann}}$	$\Delta T_{\mathbf{pw}}$	$\sigma_{\mathbf{pw}}$
iL+oL	**2.3 K**	1.5 K	**2.4 K**	3.1 K
iL+oP	**-0.2 K***	1.3 K	**1.6 K**	2.7 K
iP+oL	**1.9 K**	1.4 K	**1.5 K**	2.6 K

Table 4.2: Annual mean (T_{ann}) and precipitation-weighted (T_{pw}) temperature change relative to iP+oL and associated standard deviations (σ_{ann}, σ_{pw}) for dNEEM. *Not statistically significant at the 95 % confidence level.

iL+oL and iL+oP suggests that the oceanic changes only contribute with 0.8 K (ΔT_{pw}) additional warming.

4.3.2 GrIS surface mass balance

Both the increasing temperature and the general precipitation increase could be important for a potential reduction of the Greenland ice sheet. While the ice sheet is fixed in our experiments, the offline calculations with the subsurface model presents an estimate of the combined effect of the warming and precipitation changes over GrIS. The surface mass balance (SMB) is the sum of accumulation and ablation (i.e. run-off) calculated in each grid cell based on 6-hourly output from the EC-Earth experiments (incoming shortwave and downward longwave radiation, latent and sensible heat fluxes, rain, snow and evaporation/sublimation). As EC-Earth does not have an explicit glacier mask, we have performed the calculations in all grid cells with a minimum snow depth of 10 cm across all the simulations. Consequently, our estimates likely do not capture the full ablation zone, where the snow cover would melt every year. Therefore, we do not consider the integrated SMB, but only the spatial pattern. Figure 4.6 shows the resulting SMB changes in the three simulations compared to iP+oP.

The SMB change in iL+oL reveals a general decrease along the coast extending further inland in the north combined with increased values along the southeast coast. The central, most elevated part of the ice sheet has a small SMB increase. The hybrid experiments reveal that most of the SMB reduction is caused directly by the insolation change (cf. iL+oP) with only a minor contribution from the oceanic conditions (mainly in the southwest, cf. iP+oL). The oceanic conditions, however, appear to drive the SMB increase in the southeast.

While no dynamic feedbacks of the ice sheet are included in these estimates, they might still indicate how the simulated changes at 125 ka could impact the ice sheet. The reduced SMB in the north and northeast could be consistent with ice sheet retreat in this region (in line with the reconstructions by *Born and Nisancioglu* (2012); *Quiquet et al.* (2013); *Stone et al.* (2013)). The increased SMB in the southeast further suggests that the ice sheet could persist in southern Greenland and remain connected to the main dome near the current summit, as the accumulation increase seems to overwhelm the impact of the increased temperature.

In summary, our experiments indicate that the insolation change has a stronger impact on the GrIS SMB compared to the SST and sea ice changes. While the oceanic changes

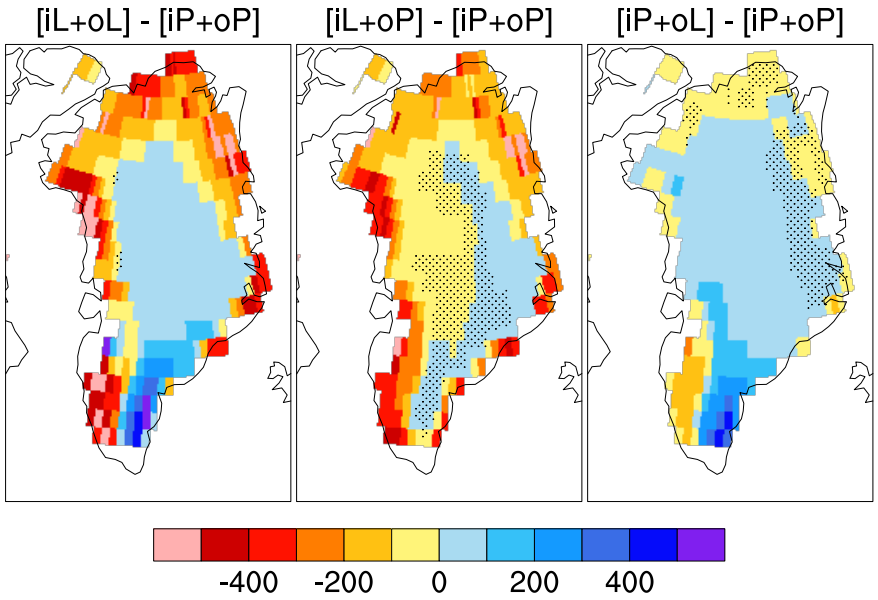

Figure 4.6: Surface mass balance anomalies [mm water-equivalent] compared to iP+oP: iL+oL (left), iL+oP (center), and iP+oL (right). Black dotted shading marks anomalies that are not significant at the 95 % confidence level.

cause a larger increase of the annual mean temperature over Greenland (Figure 4.5), the impact during summer and thus the contribution to increased melting is limited (cf. Figure 4.3). The increased summer melt thus appears to be crucial for the GrIS SMB, as strong SMB reductions are evident in iL+oP, despite the fall and winter cooling. This importance of the Eemian insolation changes for the GrIS SMB, was previous illustrated by *van de Berg et al.* (2011) based on their regional climate model experiments separating the impacts of changed insolation and changed ambient climate. Despite the fact that the Arctic warming appears stronger in our experiments [comparing EC-Earth (*Pedersen et al.*, 2016b) to the simulated Eemian warming in the ECHO-G model (*Cubasch et al.*, 2006; *Kaspar et al.*, 2007) used as boundary conditions in *van de Berg et al.* (2011)], the direct impact of the insolation is still the dominant contribution to the GrIS SMB changes. Our results thus similarly illustrate that the relation between warming and GrIS melting during the Eemian is likely not suitable for estimating the ice sheet response to future, greenhouse gas-driven warming. The combined effect of the more seasonally uniform warming and the general snowfall increase driven by the oceanic changes (iP+oL) results in a less pronounced SMB response. In southeastern Greenland, however, the oceanic changes appear to be dominating the SMB response through the increased snowfall and accumulation (Figure 4.6).

4.4 Conclusions

In line with previous model studies (*Braconnot et al.*, 2012; *Lunt et al.*, 2013; *Masson-Delmotte et al.*, 2013; *Otto-Bliesner et al.*, 2013), our simulations underestimate the warming compared to the NEEM ice core reconstructions. While we do take into account the precipitation seasonality impact on the recorded temperature signal, our model

simulations have other limitations that might contribute to the model–data discrepancy. These are, in particular, related to the fixed present-day ice sheet topography.

Firstly, a decrease of the ice sheet elevation would increase the near-surface temperature following the atmospheric lapse rate. Secondly, local circulation might be affected by altered ice sheet topography. *Merz et al.* (2014a) suggest that during winter an increased slope of the ice sheet at a given location increases the wind speed and consequently the sensible heat flux towards the surface. They estimate that GrIS topography changes could contribute up to 3.1 K annual mean warming locally at the NEEM location. Changes in the GrIS topography could also further impact the precipitation patterns and thus increase the summer weight in the precipitation-weighted temperature (*Merz et al.*, 2014b).

Our experiments show that the oceanic changes are contributing considerably to the GrIS warming. The warming even reaches the interior, elevated part of the ice sheet (including the NEEM site). Especially changes in sea ice can affect both the warming, the circulation, and the precipitation, and the GrIS changes are thus sensitive to both the magnitude and the location of sea ice loss (*Merz et al.*, 2016; *Pedersen et al.*, 2016a). Thus, the particular model's sea ice sensitivity and reference state may impact the warming. Despite the substantial Arctic warming, our simulations suggest that the Eemian Arctic sea ice extent was slightly larger than the present (e.g. in the Baffin Bay); further sea ice reduction, especially in the vicinity of Greenland, could further increase GrIS warming (*Pedersen et al.*, 2016a). Based on precipitation-weighted temperature estimates, our hybrid simulations indicate that the combined effect of sea ice loss and SST increase is responsible for 0.8–1.5 K warming recorded at the NEEM deposition site (annual mean temperatures indicate a warming impact of 1.9–2.5 K). In comparison, *Merz et al.* (2016) estimate that uncertainty in the sea ice cover can account for 1.6 K annual mean warming at the NEEM site.

The hybrid simulations illustrate that the largest contribution to the annual mean Greenland warming is due to oceanic changes. At the NEEM deposition site, the insolation changes favor changes in the precipitation seasonality that increase the summer weight in the precipitation-weighted temperature. Consequently, the isolated impacts of insolation and the associated oceanic changes on the precipitation-weighted temperature are comparable, despite the fact that the oceanic changes cause about 2 K higher annual mean warming. The SMB calculations revealed that while the oceanic changes favor increased accumulation over the southeastern GrIS, the changed insolation causes increased melting and appears to be the dominant factor behind the expected reduction of the GrIS. This reiterates the finding of *van de Berg et al.* (2011), that direct use of the relation between temperature and mass loss in the Eemian is likely to overestimate future greenhouse gas-driven melting.

4.5 Supplementary analysis: Greenland changes

The following section presents more details on the simulated Eemian climate conditions on Greenland. These sections will, unlike the paper, be based primarily on the fully coupled simulations LIG and PI. Section 4.5.1 assesses model representation of the surface changes on GrIS, while Section 4.5.2 examines the regional circulation anomalies in both the coupled and the AGCM simulations.

4.5.1 Greenland surface response

As evident from the results presented above, the warmer Arctic conditions affect the GrIS causing both increased melt and increased precipitation. Both precipitation and temperature changes could potentially impact the albedo of the ice sheet surface, and the surface processes are likely important for the simulated response on the ice sheet. Especially, since the summertime surface albedo feedback could be strengthened during the Eemian due to the increased downwelling shortwave radiation. As noted in the introduction (Section 2.3) the treatment of the GrIS surface is, unfortunately, very simplified in EC-Earth. The simulated response might therefore not capture the full impact of the surface changes.

Focusing again on the NEEM location, ice core evidence suggests regular occurrence of melt at the elevated site (*NEEM community members*, 2013; *Landais et al.*, 2016). Melt events would further accelerate surface warming by lowering the albedo: The surface albedo of the snow-covered ice sheet depends on both the snow depth, age, temperature, and liquid water content (*Warren*, 1982; *Hall*, 2004; *Box et al.*, 2012). While complete loss of the snow cover increases the albedo by revealing the darker underlying surface (ice or ground), melting on the snow-covered surface may also decrease the albedo due to snow metamorphism and accumulation of impurities (*van As et al.*, 2013). Based on the monthly mean surface temperature, the LIG simulation clearly exhibits increased potential for melt on the more elevated parts of the ice sheet. Figure 4.7 reveals that the monthly mean melting/freezing contour is situated much further inland (i.e. at higher elevation) during LIG summer (compared to PI).

The freezing temperature contours in Figure 4.7 are obviously only indicating which areas that experience melting in the monthly mean. It is, however, indicating that the probability of melt events on the interior ice sheet has increased substantially.

Based on 6-hourly output data, we have traced the occurrence of near-surface melt at the dNEEM location in LIG and PI. Unlike the ice core proxy records, no melt events are simulated at the dNEEM location in the LIG experiment. Only on four occasions in the 100 year ensemble is the temperature above -1°C. A cautionary note, is that this melt assessment relies on the absolute values simulated by the model. As described in Section 2.3, EC-Earth has a cold bias in the surface temperature over the majority of the Greenland ice sheet.

In order to assess the impact of the surface changes in the model, we have calculated the shortwave albedo as the ratio of downwelling and reflected shortwave radiation over

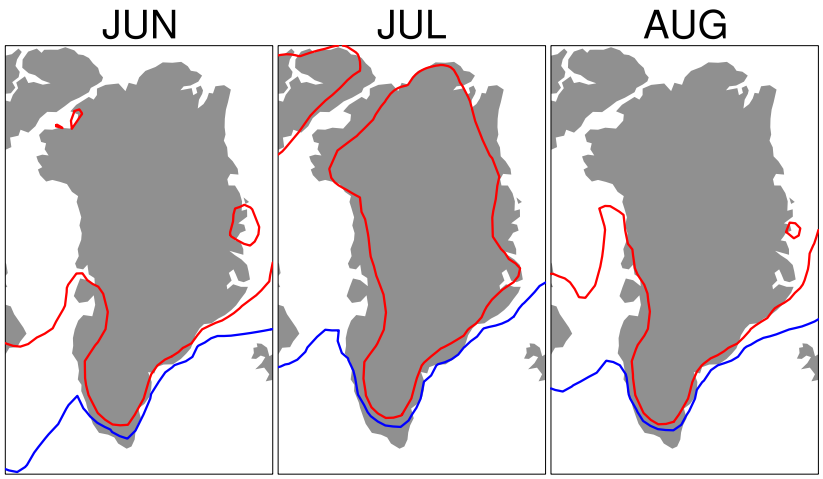

Figure 4.7: Summer near-surface air temperature freezing point (273.15 K) contours: LIG (red) and PI (blue).

GrIS:

$$\alpha_{\mathrm{SW,SFC}} = \frac{F^{\uparrow}_{\mathrm{SW,SFC}}}{F^{\downarrow}_{\mathrm{SW,SFC}}} \tag{4.2}$$

where $\alpha_{\mathrm{SW,SFC}}$ is the shortwave, surface albedo and $F_{\mathrm{SW,SFC}}$ is shortwave flux at the surface with the arrows indicating downwelling and reflected fluxes, respectively. The albedo anomalies in Figure 4.8 resemble the snow-depth changes (not shown): substantial melt near the coastal margins has reduced the surface albedo.

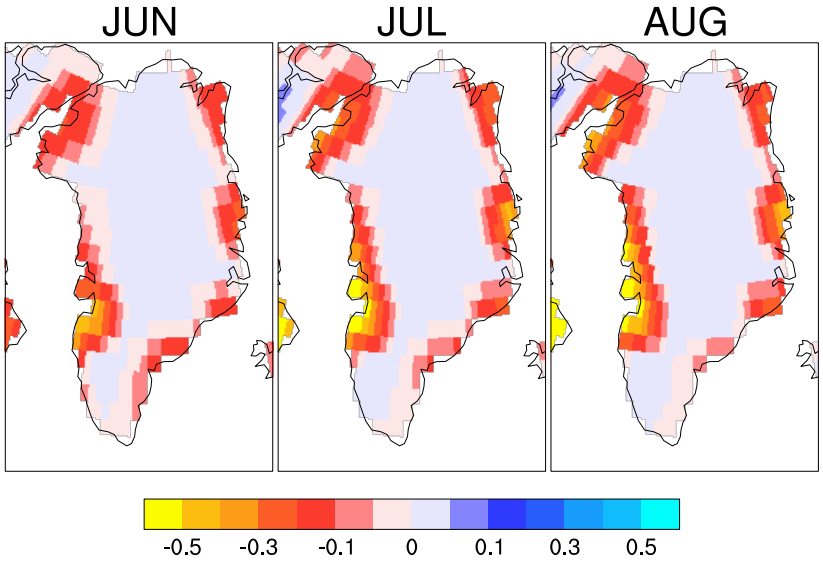

Figure 4.8: Summer surface albedo anomalies in LIG compared to PI. Negative anomalies (red-yellow) indicate increased absorption, positive anomalies (blue) increased reflection.

The interior ice sheet, however, exhibits an almost unchanged surface albedo. While this may be the net impact of albedo reduction from warming being balanced by albedo

increase from snowfall (albedo "refreshing" from snowfall events, e.g. *van den Broeke et al.*, 2011), it is likely a result of the surface treatment in the model. The unchanged surface albedo could be the result of (i) the model representation of the surface processes leading to a diminished surface albedo feedback or (ii) a model cold bias that sustains a high albedo on the interior ice sheet. The absence of melt events is consistent with (ii), while both (i) and (ii) could be contributing to the relatively cold conditions on the interior ice sheet. As ice core records suggest that melt events occurred during the Eemian, the model representation of the surface conditions likely leads to an underestimated Eemian warming at the dNEEM site, which could explain part of the discrepancy between model and proxy data reconstructions.

Opposite the central ice sheet, the surface treatment in EC-Earth may lead to overestimated warming near the margins. The summertime snow cover is lost completely in the low-elevation, near-coastal regions, and as described in Section 4.3 these regions exhibit enhanced warming. Because EC-Earth has no glacier surface type, the ice sheet surface is treated as a soil-type. Consequently, the land surface (which should be ice) can be heated beyond 0°C, thereby creating an unrealistic sensible heat flux upwards from the surface. This effect may lead to an overestimated warming in the regions with substantial snow melt.

4.5.2 Circulation changes

Atmospheric circulation changes can have a large impact on the conditions on the Greenland ice sheet. *Merz et al.* (2016) show how Eemian sea ice and SST anomalies in the Nordic Seas create a circulation anomaly that increases the advection towards the interior GrIS. As a consequence of the changed circulation, the relatively distant sea ice loss in the Nordic Seas is shown to have a larger impact on the conditions at NEEM compared to nearby sea ice loss in the Labrador Sea. In the following, we assess the circulation changes near Greenland and the potential impact on the simulated changes on the ice sheet.

Figure 4.9 compares the low-level wind anomalies and the near-surface warming in LIG relative to PI, and indicates that the warming pattern is affected by the circulation changes.

Despite substantial sea ice loss in the Nordic Seas, our simulations do not recreate the strong wintertime circulation anomaly found by *Merz et al.* (2016). While the wintertime circulation exhibits increased flow towards the continent at the southeast coast, the anomaly is weaker than observed in their CESM simulations. But combined with a smaller magnitude anomaly on the southwest coast, the anomalous circulation could be contributing to the warming simulated over the southern GrIS. The spring pattern has a similar anomaly near the southeast coast that could contribute to the simulated near-coastal warming. The strongest anomalies are found during summer, when increased onshore winds coincide with regions of substantial warming in the eastern, northwestern and central-western coastal areas.

While the circulation anomalies seem to contribute to warming over the ice sheet, they appear insufficient to cause substantial warming over the central elevated part of the ice

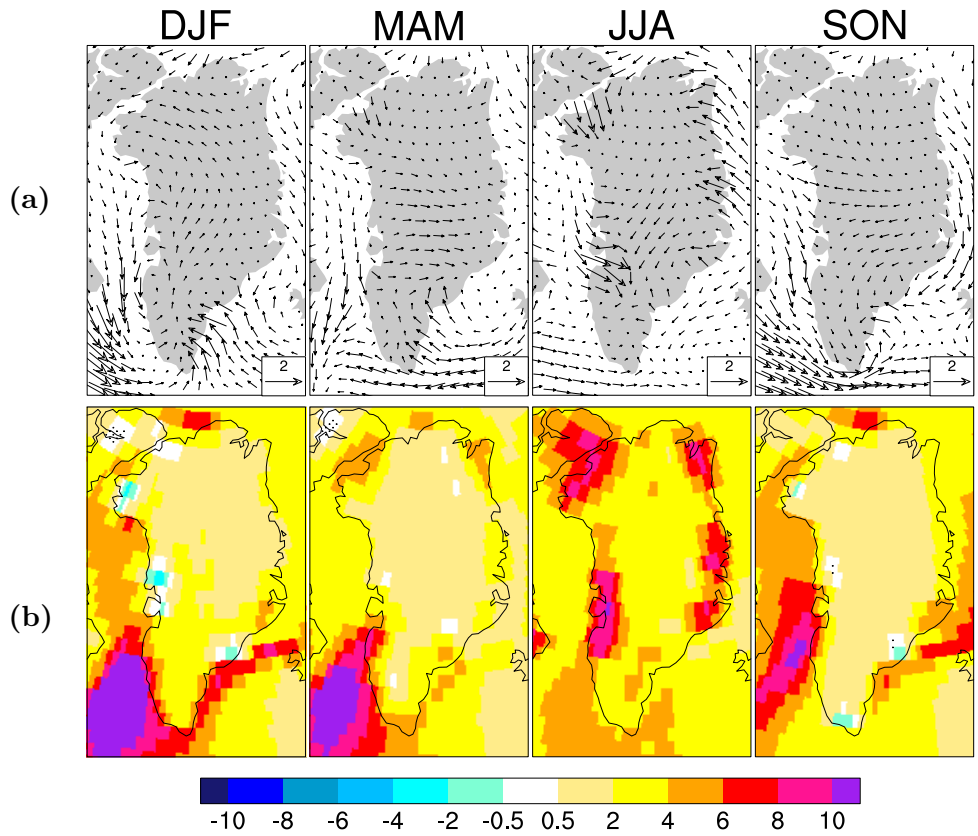

Figure 4.9: Seasonal mean anomalies in LIG compared to PI: **(a)** wind (10 m) [m/s] and **(b)** near-surface temperature [K]. Black dotted shading indicates changes that are not significant at the 95 % confidence level.

sheet. From the cross-sections (longitude-by-height, Figure 4.10) along 65°N and 75°N it is clear that the warming largely remains confined to the lower, coastal areas.

With the exception of the summer anomalies, both the northern (75°N) and southern (65°N) transects reveal how the surface-based warming is not reaching the interior parts of the ice sheets; even in the southern part with lower elevation. In comparison, the simulation by *Merz et al.* (2016) reveal how a stronger circulation anomaly could promote advection of warm air to the more elevated parts of the ice sheet. The limited warming over the central ice sheet is likely related to the GrIS topography and the local circulation patterns: the steep slopes limit the flow from the inland from the coast, while katabatic winds and the "Greenland anti-cyclone" with strong winds along the ice sheet margins limits the inland heat advection (*Steffen and Box*, 2001; *Noël et al.*, 2014; *Merz et al.*, 2016). During the colder seasons, the lower atmosphere has a very stable stratification (especially over sea ice) which could also contribute to limiting the vertical extent of the warming (more details are presented on the vertical structure of warming in Sections 5.3 and 6.2).

Using the AGCM experiments, we again try to disentangle the contributions to the circulation anomalies. These experiments can indicate whether the circulation changes

(a) 65°N

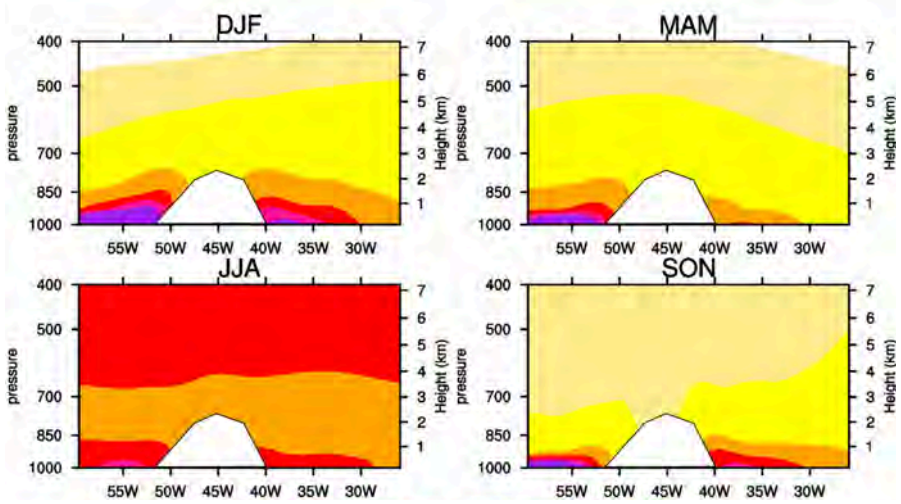

(b) 75°N

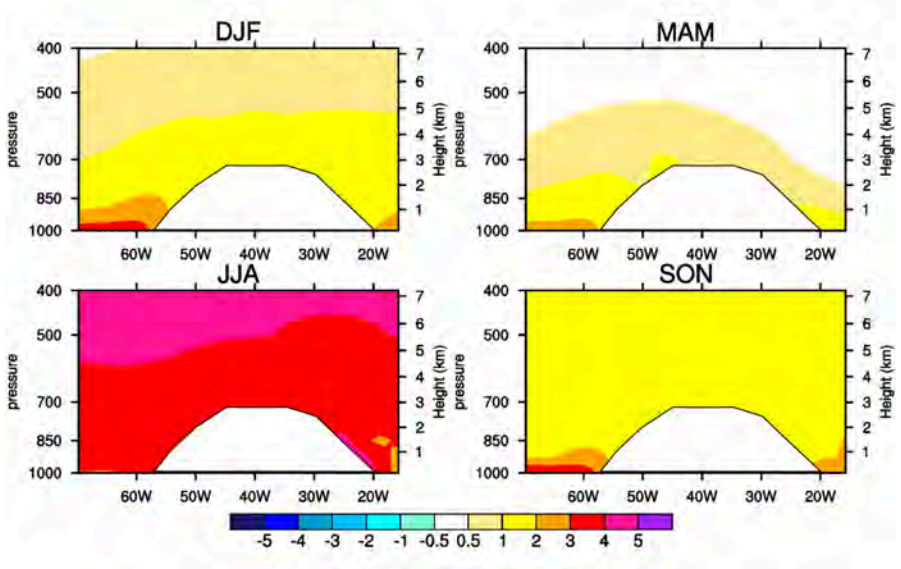

Figure 4.10: Vertical structure of warming over Greenland illustrated by cross-sections along (a) 65°N and (b) 75°N. White shaded area indicates the topography of the ice sheet.

are driven by insolation, sea surface conditions, or only occurs due to the combined impact of the two.

The AGCM experiments indicate that the onshore wind anomalies on the southeast coast are driven by the changed sea surface conditions: iP+oL and iL+oL both exhibit increased winds towards the ice sheet during winter and, with less pronounced anomalies, during spring and fall. The summertime anomalies observed in the coupled experiment and in iL+oL near the Disko Bay on the central west coast are not seen in any of the hybrid experiments (iL+oP or iP+oL), suggesting that both the insolation increase and the warmer sea surface conditions are required to drive the anomalous inland advection.

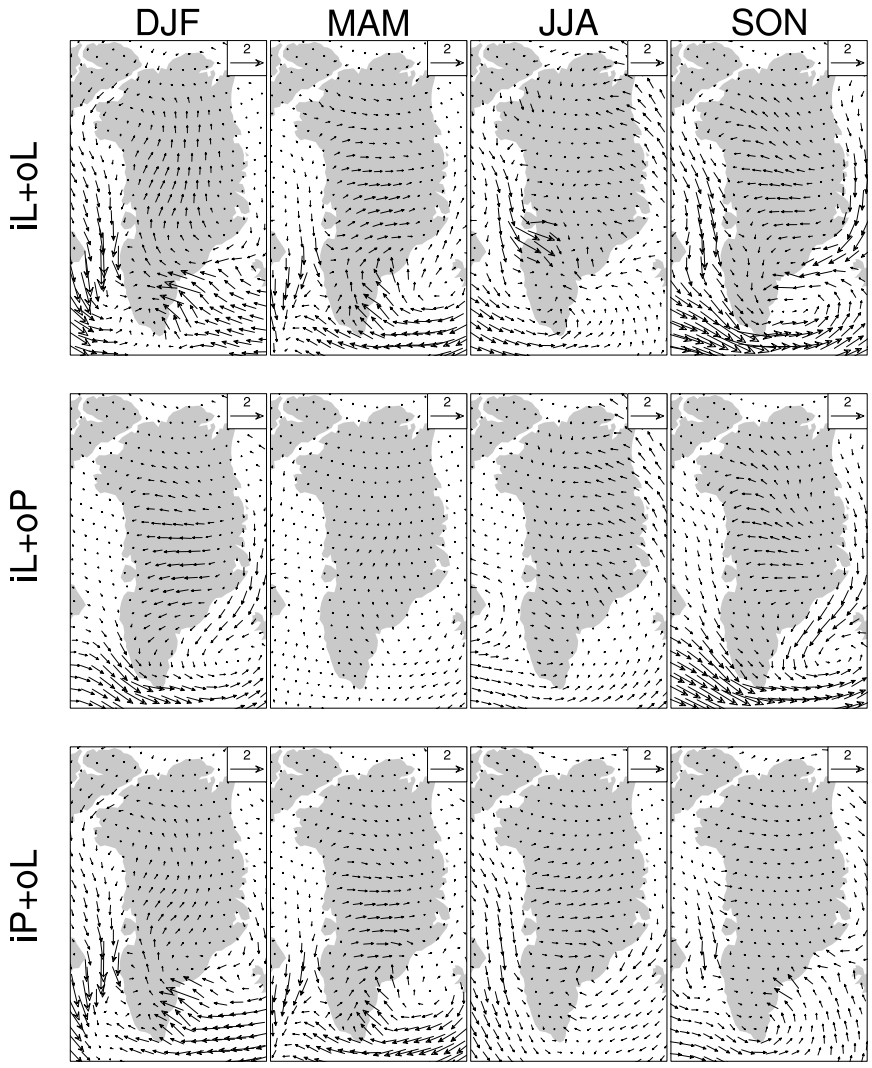

Figure 4.11: Seasonal mean wind (10 m) anomalies [m/s] in the AGCM experiments relative to iP+oP: iL+oL (top), iL+oP (mid) and iP+oL (bottom).

The increased onshore flow at the southeast coast appears to be a result of the changed sea surface conditions. The onshore advection is increased during winter, spring, and fall, consistent with the simulated precipitation increase in the south-southeast region (Section 4.3, Figure 4.4): increased onshore advection is expected to increase the precipitation due to orographic lifting (*Ohmura and Reeh*, 1991; *Chen et al.*, 1997; *Schuenemann et al.*, 2009).

4.6 Isolated impact of sea ice loss

As in Section 3.7, the isolated impact of sea ice loss can be assessed based on the iP+oP-ice simulation (LIG sea ice conditions with PI SSTs and insolation). The simulated SST increase from the coupled LIG experiment is a combined result of ocean circulation changes, increased insolation, and sea ice related effects (increased absorption during summer and revealed open ocean during winter). The iP+oP-ice simulation thus presents

a conservative estimate of the isolated impact of the sea ice changes by excluding all SST warming (regardless of the causes of the warming). Figure 4.12 compares the temperature and wind anomalies in iP+oP-ice to iP+oL, indicating the relative impacts of the sea ice loss and the SST increase.

The sea ice loss explains a large fraction of the warming during winter and spring. This is in line with the described insulation effect: During the colder seasons the large temperature gradient between the ocean surface and the atmosphere leads to an increased heat flux. Additional ocean warming would further strengthen this gradient, but the additional warming of 3–5 K (cf. Figure 4.2) is only a minor contribution compared to the strong atmosphere-ocean gradient. This comparison also reveals that the sea ice loss causes substantial warming over GrIS, even when the AMOC related SST increase in the North Atlantic is disregarded. During summer and fall, the iP+oP-ice exhibits more limited changes compared to iP+oL – as discussed in Section 3.7 this is a direct consequence of the fixed SST setup.

The wind anomalies reveal that the circulation changes are almost similar in iP+oP-ice and iP+oL. Hence, the SST increase appears to have a minor impact on the near-Greenland circulation. Especially the anomalous on-shore wind in southeastern Greenland is very similar in iP+oP-ice and iP+oL. The snowfall anomalies (not shown), however, only reveal very limited changes in iP+oP-ice. The two experiments thus indicate that the SST increase is a prerequisite for the simulated snowfall/accumulation increase.

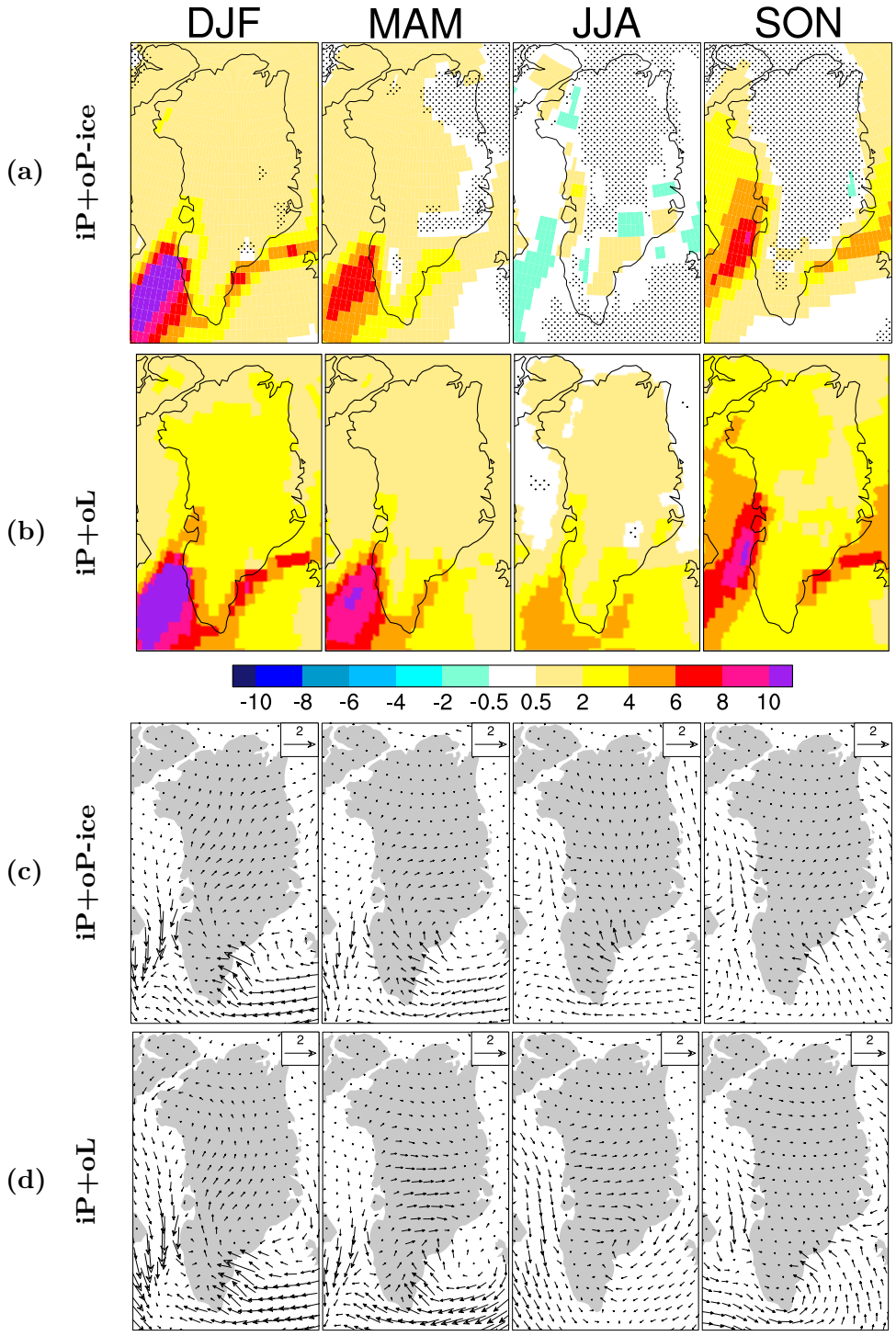

Figure 4.12: Seasonal mean anomalies in iP+oP-ice compared to iP+oL (both relative to iP+oP). **(a)** and **(b)**: near-surface temperature [K] in iP+oP-ice and iP+oL. Black dotted shading indicates changes that are not significant at the 95 % confidence level. **(c)** and **(d)**: 10 m wind [m s^{-1}] (reference vector is 2 m s^{-1}).

5 Regional Arctic sea ice loss: The impact on atmospheric circulation and the NAO

The assessment of the last interglacial climate in the past two chapters clearly illustrated the central role of sea ice changes. This chapter will further investigate the mechanisms related to sea ice loss through a set of idealized GCM simulations. The following sections will present the study by *Pedersen et al.* (2016a) which is included in full extent. The content from the paper is further discussed in Chapter 6, where the results are compared to the findings from the paleoclimate simulation. In that regard, the study has been expanded with Section 6.1 presenting a more detailed examination of the conditions on the Greenland ice sheet.

5.1 Introduction

The drastic Arctic sea ice decline observed in recent years (*Vaughan et al.*, 2013) has motivated an increased scientific focus on the impacts of sea ice loss on weather and climate. The surface energy balance is affected by sea ice loss through surface albedo changes and due to a reduction of the insulating layer between the ocean and the atmosphere (*Stroeve et al.*, 2012b). These characteristics mean that sea ice loss initiates feedbacks that contribute directly to Arctic amplification of near-surface warming (*Serreze et al.*, 2009; *Screen and Simmonds*, 2010b; *Serreze and Barry*, 2011). Furthermore, Arctic sea ice loss has been linked to climatic changes at lower latitudes through shifts in the oceanic and atmospheric circulation (*Bader et al.*, 2011; *Vihma*, 2014). The remote changes, however, remain challenging to interpret and the mechanisms are still subject to investigation (*Francis and Vavrus*, 2012; *Screen and Simmonds*, 2013; *Barnes*, 2013; *Wallace et al.*, 2014).

This study investigates the impacts of regional Arctic sea ice loss on high and mid-latitude climate. In an atmospheric general circulation model (GCM) coupled to a slab ocean, we study the atmospheric response to prescribed reductions in the Arctic sea ice cover. In contrast to the slab ocean simulations performed here, most previous studies prescribe both the sea ice and sea surface temperatures (SST) (*Seierstad and Bader*, 2008; *Deser et al.*, 2010; *Blüthgen et al.*, 2012; *Screen et al.*, 2013; *Peings and Magnusdottir*, 2014). As discussed by *Screen et al.* (2013), the atmospheric response

in the prescribed SST experiments does not describe the isolated impact of the sea ice change, but is a combined response to sea ice and SST change. An advantage of our hybrid setup is that sea surface temperatures are not prescribed; the only forcing is the prescribed sea ice loss. Most importantly, since our slab ocean setup allows for interaction between the atmosphere and the surface ocean (SSTs), we can account for the teleconnections dependent on such exchange (*Chiang and Bitz*, 2005; *Cvijanovic and Chiang*, 2013).

The atmospheric response to different sea ice configurations has been shown to be sensitive to the geographical location of ice loss (*Petoukhov and Semenov*, 2010; *Rinke et al.*, 2013). We use the new hybrid setup to investigate the atmospheric response to three different sea ice scenarios with ice loss in different parts of the Arctic. Our model simulations are designed to reveal the isolated impact of a changing sea ice cover, as the prescribed sea ice loss is the only forcing in these experiments.

In Section 5.2 we describe the climate model configuration and the experimental design. The results are presented and discussed in Section 5.3, where we assess the impact of the sea ice loss on the Arctic climate, the Northern Hemisphere atmospheric circulation and the NAO. Conclusions are presented in Section 5.4.

5.2 Methods

5.2.1 Climate model configuration

In this study, we use the National Center for Atmospheric Research's Community Earth System Model (CESM) version 1.0.4 (*Gent et al.*, 2011), which in this setup includes the Community Land Model (CLM4, *Lawrence et al.*, 2011) and the Community Atmosphere Model (CAM4, *Neale et al.*, 2013) coupled to a slab ocean (*Danabasoglu and Gent*, 2009; *Neale et al.*, 2010). The model integrations are performed on a finite volume 1.9 $\times$ 2.5 degree grid with 26 atmospheric layers in the vertical. The slab ocean is designed to approximate the behavior of the ocean component of the fully coupled model. *Danabasoglu and Gent* (2009) compare the slab ocean and the fully coupled configurations of the previous generation model (CCSM3) and find that the slab ocean setup provides a good estimate of the climate sensitivity of the fully coupled model. The input fields required for slab ocean simulations (prescribed ocean heat flux (q-flux), salinity, temperature, and velocity fields) are derived from a preindustrial CESM simulation using a full-depth ocean. The ocean input fields are identical in all the simulations presented here, and any potential thermohaline or wind driven ocean heat transport changes are thus disabled (as noted in *Caldeira and Cvijanovic* (2014)).

This model setup is an extension of the prescribed sea ice setup used by *Cvijanovic and Caldeira* (2015) and *Caldeira and Cvijanovic* (2014). The new setup combines the two types of simulations used in these studies. The first configuration maintains ice free conditions by allowing ocean temperatures to drop below freezing without initiating sea ice formation. The second prescribes the sea ice cover thus preventing sea ice loss in a warming climate, and can be viewed as a hybrid between the slab ocean model (SOM) and the data ocean model (DOM) with interactive sea surface temperatures and fixed sea ice.

In the current setup, we prescribe the sea ice cover to a specified extent while also allowing ocean temperatures to fall below the freezing point (-1.8°C) in order to prevent new sea ice formation. This combination makes it possible to prescribe any sea ice configuration regardless of the climate state. We allow ocean temperatures below the freezing point in order to prevent an unrealistic increase of the heat flux exchange over ice free areas where new sea ice would form otherwise. Thus our simulations present a more conservative estimate of the forcing from the sea ice loss. The results will reveal that the ice loss still induces a substantial forcing even with subfreezing ocean temperatures allowed.

However, it is useful to note that none of the four simulations presented here have sub-freezing sea surface temperatures in pure ocean grid cells (where the sum of land and sea ice fractions is below 1 %). The lowest temperature found in grid cells with a minimum of 50 % ocean coverage is 262 K. This could be a reasonable average wintertime surface temperature over an area consisting of 50 % sea ice or land and 50 % open ocean near the freezing point. As our idealized model setup is a simplification of the fully coupled system, it does not describe all the mechanisms of the real world climate system. While the coupled CESM model in itself has known biases that may affect the simulated response (e.g. excessive low clouds in the Arctic (*Gent et al.*, 2011; *Kay et al.*, 2012)), it is important to note the further limitations that arise from our modification of the setup. A noteworthy shortcoming of the current setup is that the fixed sea ice conditions disable any potential feedbacks from the atmospheric circulation affecting the ice cover. Such feedbacks are known to be important in shaping the Arctic sea ice cover, e.g. by increasing sea ice export from the Arctic (*Blüthgen et al.*, 2012).

5.2.2 Experimental design

In this study, we analyze the atmospheric response to three idealized sea ice reduction scenarios: (i) sea ice loss over the entire Arctic region; and sea ice loss confined to the (ii) Atlantic and (iii) Pacific sectors of the Arctic. These three scenarios are compared to a pre-industrial control state (CTRL), which is also simulated using the prescribed ice, slab ocean configuration. The prescribed CTRL sea ice conditions are obtained from a coupled CESM pre-industrial simulation with a full-depth ocean.

The first scenario represents a reduction of the Arctic sea ice cover across all longitudes (hereafter referred to as the ARC scenario). The annual minimum September sea ice extent is constructed by removing all sea ice south of 78°°N from the CTRL September extent. To avoid unnatural steep gradients in the sea ice cover, the ice concentrations are smoothed near the new, constructed ice edges. The areas in the two southernmost grid cells along the new ice edge have been reduced to respectively 33 % and 66 % of the control climate ice concentration across all longitudes. The resulting ice cover is shown in Figure 5.1.

Based on the CTRL and ARC configurations two additional sea ice scenarios are constructed to study the atmospheric response to sea ice loss in different geographical regions. Starting from the annual minimum sea ice extent in September, the overall reduction in ARC is split in two regions, referred to as the Atlantic (ATL) and the Pacific (PAC) sectors. The two sectors are chosen so that the area of sea ice removed is

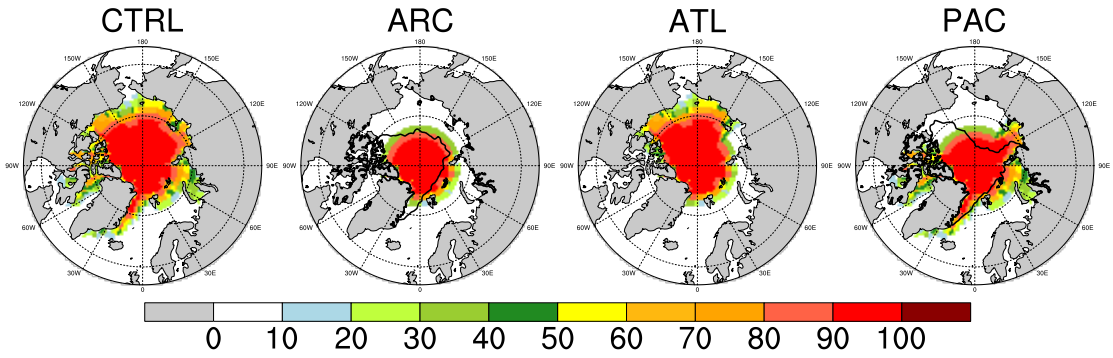

Figure 5.1: September sea ice cover [%] (i.e. annual minimum extent) in the four scenarios. Black contours overlaid on ARC and PAC illustrate observed sea ice extent in 2012 and 2007 respectively. The extent is calculated as the 15 % concentration contour in the NOAA/NSIDC Climate Data Record of Passive Microwave Sea Ice Concentration (*Meier et al.*, 2013).

identical in the two scenarios, and that the area of sea ice removed in the two sectors sum exactly to the ARC sea ice loss. In order to, once again, avoid steep gradients near the ice edges, the regions are defined with a 5° longitudinal overlap, where the sea ice in both cases is set to 50 % of the CTRL concentration. The boundaries between ATL and PAC are at 110°W (overlap from 110-115°W) and 140°E (overlap from 140-145°E). Thus the Atlantic sector includes the Baffin Bay, Greenland, Barents, Kara, and Laptev seas, while the Pacific sector covers the Beaufort, Chukchi, and East Siberian seas. Figure 5.1 displays the September sea ice cover in all four simulations (CTRL, ARC, ATL and PAC).

In the design of the Atlantic and Pacific sectors, we have aimed to balance the magnitude of forcing from the sea ice loss in the two sectors. Hence, equal amounts of sea ice area (i.e. sea ice concentration multiplied by the grid cell area) are removed in the two sectors. A consequence of this design is that the Atlantic and Pacific sectors do not cover equal geographical areas. An alternative approach would be to divide the Arctic region in two equal sectors in terms of geographical coverage. In that case, the area of sea ice removed, and thereby the induced forcing, would be substantially larger in the Pacific compared to the Atlantic sector. Therefore, the difference between the atmospheric responses in the two scenarios might be governed by the different magnitude of forcing rather than the location of the ice loss.

The geometry of the idealized sea ice cover is based on the assumption that the sea ice in the central Arctic will be more persistent in a warming climate (as illustrated by *Stroeve et al.* (2012b) for the period from 1979-2010). The prescribed ice extents resemble the observed conditions as seen from Figure 5.1 where the ARC and PAC sea ice fields have been overlaid with observed sea ice extents from 2012 and 2007, respectively (observations from NOAA/NSIDC Climate Data Record of Passive Microwave Sea Ice Concentration, *Meier et al.* (2013)).

Motivated by observational trends which show that the annual maximum sea ice extent exhibits a limited decrease compared to the annual minimum extent (*Stroeve et al.*, 2012a), the March sea ice is left unchanged from the CTRL. The sea ice concentrations in all other months are constructed from monthly weighted means between the new

reduced September conditions and the concentrations from the control climate in the given month (the annual cycle of total sea ice area is presented in Figure 5.2).

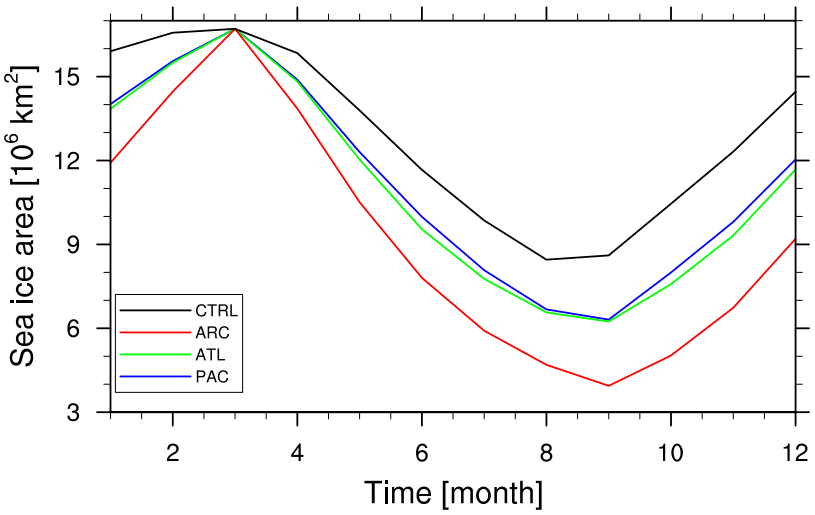

Figure 5.2: Annual cycle of northern hemisphere sea ice area (10^6 km^2) in the four simulations: CTRL (black), ARC (red), ATL (green), and PAC (blue).

Compared to the control climate, the imposed sea ice area changes results in a year-round sea ice reduction; increasing from no change in March to maximum change in September. Figure 5.3 displays the seasonal mean sea ice reduction in ARC compared to CTRL, with the boundaries of the two regional scenarios depicted by colored boxes. All the simulations are identical except for the Arctic sea ice cover. Sea ice thickness is fixed (1 meter in the Northern Hemisphere and 2 meters in the Southern) and the atmospheric conditions are kept at the pre-industrial level.

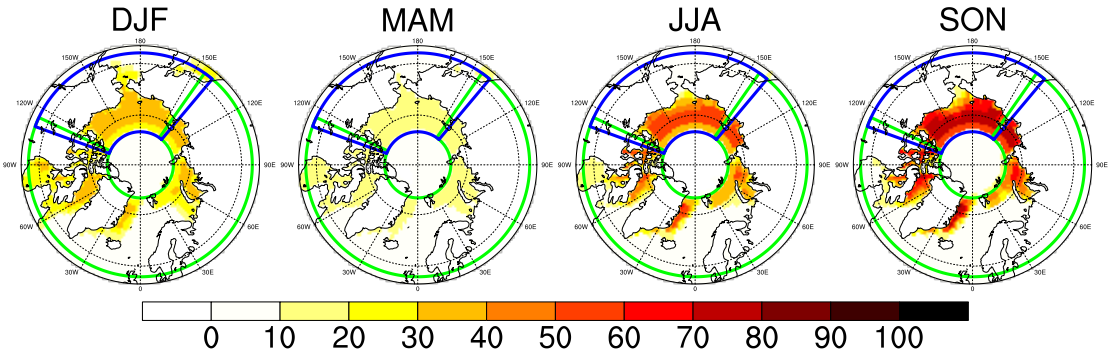

Figure 5.3: Seasonal mean anomalies in sea ice concentration []%] between the reduction scenarios and the pre-industrial control climate (CTRL). The Pacific Sector (PAC) is bounded by the blue line, the Atlantic sector (ATL) by the green line, and the overall reduction (ARC) is across all longitudes.

Anomalies presented in the remaining text are based on climatological means over the last 30 years of the model simulations. The climatologies are based on monthly mean data. The total length of each simulation is 60 years, with the first 30 years disregarded

as spin-up. Statistical significance of changes are assessed using a two-sided Student's t-test (*von Storch and Zwiers*, 2001).

5.3 Results and discussion

5.3.1 Arctic response, local changes

The imposed sea ice loss causes vast changes in the Arctic climate in our model simulations. Across all three scenarios, the surface-based changes in sea ice cause a geographically widespread warming in the near-surface air temperature throughout the year (displayed in Figure 5.4).

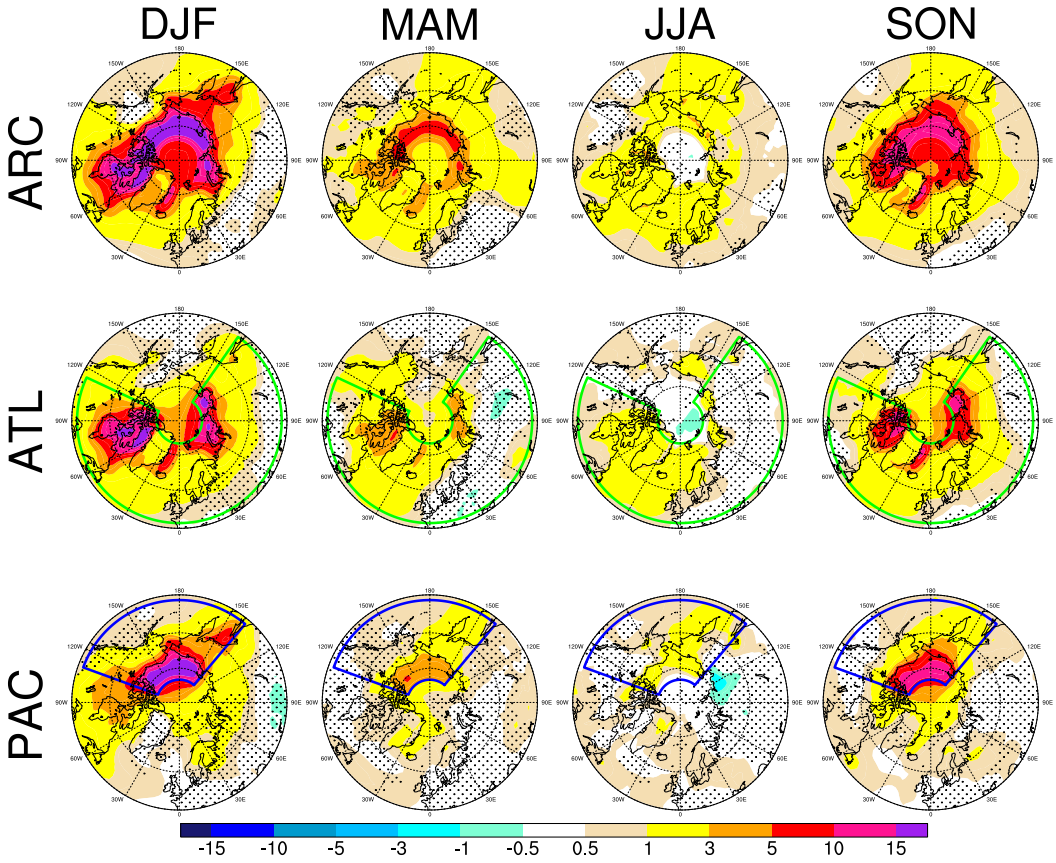

Figure 5.4: Seasonal mean near-surface air temperature change [K] compared to the control climate (CTRL). Colored boxes indicate regions of sea ice loss; the top row (ARC) is reduced at all longitudes. Black dotted areas indicate anomalies not statistical significant at the 95 % confidence level. Note the irregular spacing of the color bar.

The peak warming is more than 15 K and coincides geographically with the ice loss area. The maximum warming is found in the winter season (DJF) in all three scenarios. This might appear surprising, as the maximum sea ice loss is introduced in September. The reason for this delayed response is found in the physical mechanisms behind the warming. Sea ice loss affects the surface energy fluxes by altering the shortwave, longwave and

turbulent heat (latent and sensible heat) fluxes at the ocean surface. Figure 5.5 shows the annual cycle of the Arctic mean surface turbulent heat and net energy flux changes, and reveals that the wintertime warming is driven mainly by turbulent heat flux from the ocean surface. Even though the ice cover is partially restored during winter, the insulating effect of the sea ice is reduced and increasing amounts of heat and moisture can be exchanged between the ocean and atmosphere. The insulation between the ocean and atmosphere is only weakened due to reductions in the sea ice concentration, as the ice thickness is fixed in our experiments. The upwards heat flux is driven by the large wintertime temperature gradient between ocean and atmosphere, which persists in our experiments although the SST is allowed to cool below freezing. This key role of the turbulent heat flux and the related delayed warming agrees with several other studies of sea ice loss (*Deser et al.*, 2010; *Screen et al.*, 2013; *Vihma*, 2014).

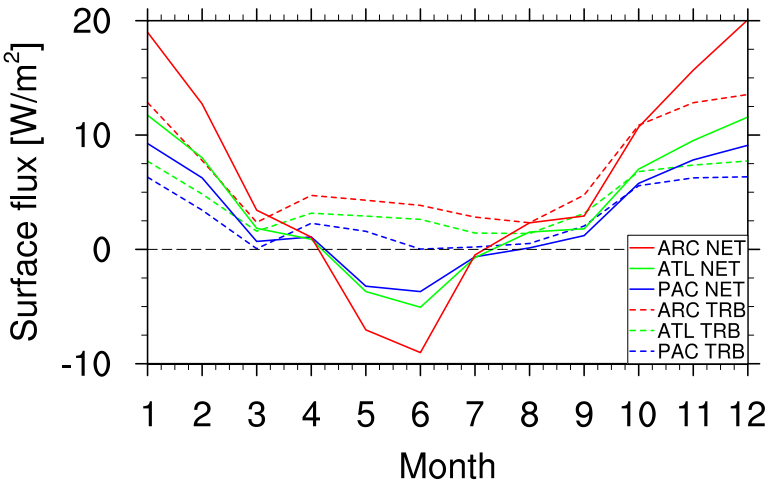

Figure 5.5: Seasonal cycles of Arctic (60–90°N) monthly mean surface flux anomalies [W m^{-2}] in the three scenarios compared to CTRL: ARC in red, ATL in green, and PAC in blue. The net flux (NET, solid lines) is the sum of the shortwave, longwave, sensible heat and latent heat surface fluxes and the turbulent heat flux (TRB, dashed lines) is the sum of the sensible and latent heat surface fluxes. Positive values indicate flux upwards from the surface to the atmosphere.

Increased longwave loss from the surface also contributes to the surface-based warming, but the longwave flux change only amounts to one third of the turbulent changes during winter (compare the net and the turbulent heat fluxes in Figure 5.5). The shortwave flux does not contribute directly to the atmospheric warming, but may have an indirect impact by causing additional ocean warming in regions of ice loss. Increased shortwave absorption is contributing to the negative net surface flux during summer evident in Figure 5.5.

The temperature response resembles the spatial pattern of the sea ice loss (compare Figures 5.3 and 5.4). This is likely connected to a limited vertical extent of the warming (not shown), due to a very stable structure of the lower atmosphere. Low level stability with frequent surface-based inversions is a well-known feature in the Arctic seen in both observations and climate models (*Zhang et al.*, 2011). Climate models, including the one employed here, even have a tendency to overestimate the stability during the polar night (*Boé et al.*, 2009; *Barton et al.*, 2014). Our simulations show that the surface-based warming will gradually work to weaken the stability, but that the inversion structure

persists over the remaining sea ice cover even with the substantial warming simulated here.

An interesting feature in the warming pattern (Figure 5.4) is the warming over the Greenland Ice Sheet (GrIS). Sea ice changes in the vicinity of Greenland are expected to cause warming over the ice sheet through atmospheric heat advection. Accordingly, significant warming signals are evident over GrIS in both ARC and ATL. In contrast, the more remote sea ice loss in the Pacific region only seems to cause a limited or insignificant Greenland warming signal. This indicates that sea ice loss distant from the GrIS (such as the minimum extent observed in 2007) does not have a substantial impact on the temperatures over the ice sheet. This finding is relevant to projections of GrIS melt in a warmer climate, i.e. simulations of future as well as paleo-climate scenarios.

5.3.2 Remote response and circulation changes

Despite the fact that the sea ice forcing is largest in the autumn, the near-surface warming peaks during winter. This could indicate that the atmosphere experiences the largest forcing during winter rather than autumn. However, it is not certain that the strongest response of the atmospheric circulation coincides with the maximum near-surface temperature change. Thus, the fall (SON) seasonal mean and the monthly progression of the atmospheric circulation response have been examined (not shown). While it might not be linked directly to the near-surface temperature response, we find that the circulation response is indeed strongest during winter (the three variables considered here are geopotential height, zonal wind and transient eddy kinetic energy). The fall patterns exhibit some significant changes, but compared to the winter patterns the changes are of lower magnitude and with less widespread significance.

The monthly data reveals that the changes in the individual months are roughly similar to the seasonal means. The strongest circulation responses are found between November and February, but we find no clear pattern in the timing of the strongest changes. The timing varies both between the experiments and the individual circulation parameters (i.e. geopotential height, zonal wind, and transient eddy kinetic energy).

As our simulations exhibit the strongest response to the sea ice loss during winter, the remainder of this analysis will focus on the wintertime (DJF) seasonal mean changes.

The temperature anomalies in Figure 5.4 show substantial warming outside the regions of ice loss. Warming in the vicinity of the ice loss is an expected result of heat advection from the newly ice free regions (*Serreze et al.*, 2011). Warming in more distant areas, however, could be related to changes in the atmospheric circulation rather than direct advection from the heat source. One asset of our hybrid setup is exactly that it allows these remote changes. An alternative setup with fixed SSTs would inhibit remote changes over ocean surfaces and potentially limit or completely disable important feedbacks and teleconnections.

Previous studies have indeed indicated that the large scale circulation could be affected by sea ice loss (*Bader et al.*, 2011; *Vihma*, 2014). Depending on the mechanisms behind potential remote changes, the different sea ice scenarios simulated here may lead to

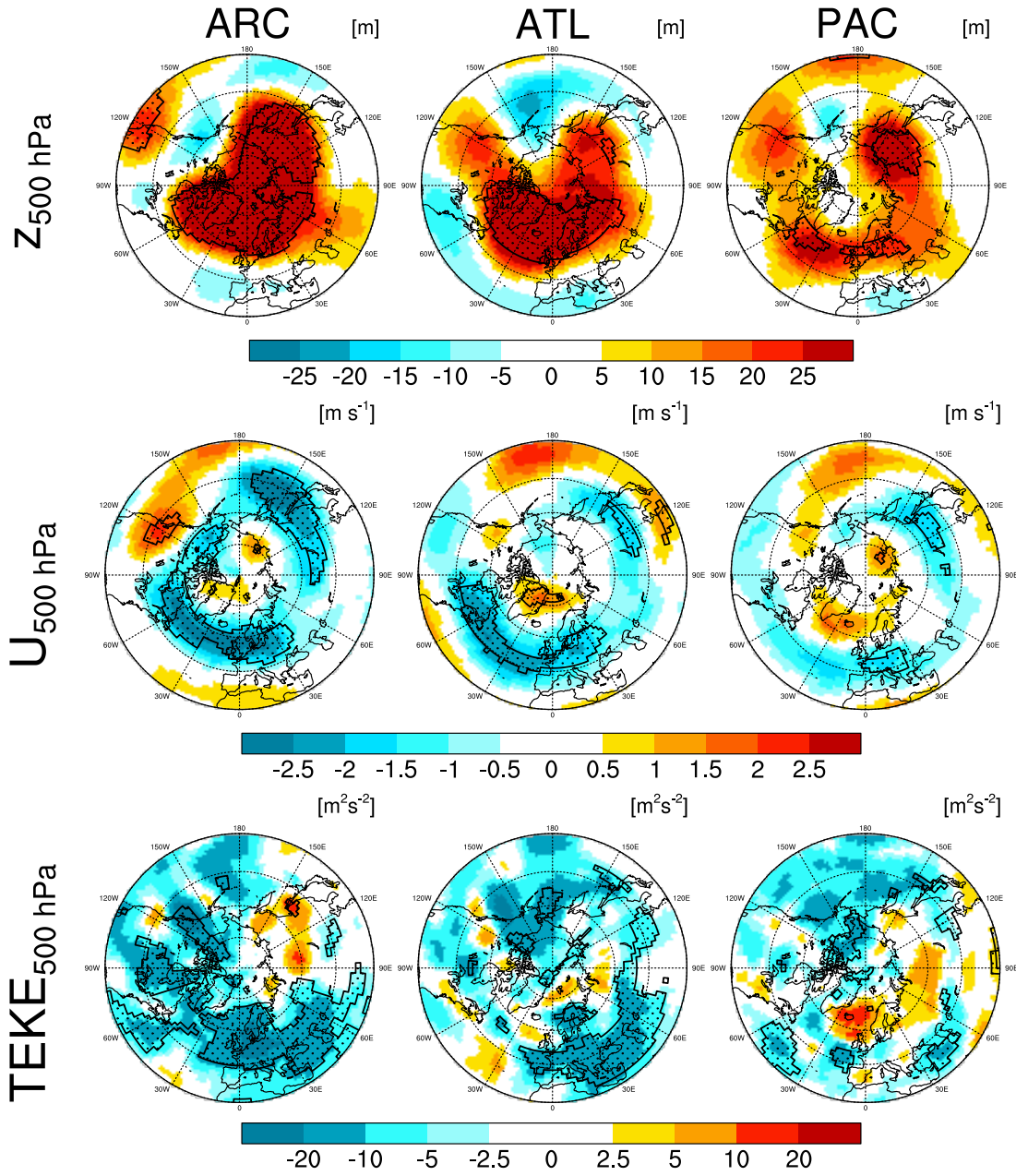

Figure 5.6: Winter (DJF) atmospheric circulation anomalies in the three scenarios ARC (left column), ATL (middle column) and PAC (right column) compared to CTRL: the height of the 500 hPa geopotential surface (top row), zonal wind speed (middle row) and transient eddy kinetic energy (lower row). All three parameters are shown at the 500 hPa level. Dotted areas indicate that the anomalies are statistically significant at the 95 % confidence level. Note the irregular spacing of the TEKE color bar.

different circulation shifts. To examine such changes, a range of atmospheric properties are investigated in the following (see Figure 5.6).

The geopotential height of the 500 hPa pressure surface increases at high latitudes across all three scenarios (Figure 5.6, top row). This is an expected result of the surface-based warming, which works to expand the overlying air masses. In the ARC scenario, the increase is statistically significant in an area covering the entire Arctic region towards

the mid-latitudes. In the ATL and PAC scenarios, the maximum increase is found in the vicinity of the ice loss regions. Significant increases are, nonetheless, also found in smaller areas more remote to the sea ice loss in both scenarios. All three simulations show increased geopotential height over the Labrador Sea, parts of Northern Europe and parts of Northeast Asia. Similar increases appear in ARC and ATL over Northwest Asia, while no significant signal is found in PAC. Most of the significant increase is found over or adjacent to areas with strong surface-based warming. This agrees with the general expectation of geopotential height increases in warming regions, but especially the PAC response indicates that strong near-surface warming can occur without increased geopotential height directly above.

The general reduction of the equator-to-pole temperature gradient is manifested in the geopotential height, where the meridional gradient is also reduced. This is expected to have implications for the mid-latitude atmospheric circulation (*Francis and Vavrus*, 2012; *Peings and Magnusdottir*, 2014). Following the thermal wind relation, the mid-tropospheric zonal flow is expected to weaken with a decrease of north-south gradient of the 500 hPa geopotential height (i.e. the thickness of the 1000-500 hPa layer). Figure 5.6 (middle row) reveals that the mid-latitude flow is indeed reduced in all three scenarios; albeit more widespread in ATL and especially ARC compared to PAC. As expected from the thermal wind relation, the zonal wind reduction appears to agree well with the geopotential height changes. Areas of significant zonal wind reduction appear south of regions with geopotential height increases in all three scenarios.

All three ice loss patterns result in a reduced flow over East Asian mid-latitudes and parts of central Europe. The overall ice loss in ARC causes significant reductions in a wide mid-latitude band across over the North Atlantic, Europe, East Asia, the West-Pacific and northern North America. The ATL response shows a comparable, overlapping reduction, but the ATL pattern appears to be shifted slightly southwards. The only significant PAC responses are found over East Asia and central Europe, where zonal wind reduction is found (in agreement with ARC and ATL). No significant changes are evident over the Atlantic mid-latitude region, where decreasing flow is observed in the two other scenarios.

A third indicator of atmospheric circulation changes is the transient eddy kinetic energy (TEKE) which is a measure of variability of the wind field. Following *Peixóto and Oort* (1984) TEKE is calculated from zonal and meridional wind-components (U and V) as:

$$\mathrm{TEKE} = \overline{U'^2} + \overline{V'^2} \tag{5.1}$$

where the overbar denotes time averaging, and the primes denote the departure from the mean as $U = \overline{U} + U'$. The TEKE can be used as an indicator of the locations and strengths of weather systems (transient eddies) and thus the mean storm tracks (*Hurrell et al.*, 1998; *Sewall*, 2005; *Greeves et al.*, 2007; *Seierstad and Bader*, 2008; *Li and Battisti*, 2008). The TEKE can be computed from the model wind output as:

$$\mathrm{TEKE} = \overline{U'^2} + \overline{V'^2} = \left(\overline{U^2} - \overline{U}^2\right) + \left(\overline{V^2} - \overline{V}^2\right) = \overline{UU} + \overline{VV} - \overline{U}^2 - \overline{V}^2 \tag{5.2}$$

The monthly mean value of the four latter variables are used to calculate the wintertime (DJF) seasonal mean of TEKE presented and analyzed here.

Reduced TEKE over the mid-latitudes appears as the dominant signal. The ARC scenario shows the strongest trend in the TEKE (Figure 5.6, lower row), which is reduced across the mid-latitudes ranging from North America eastwards to Europe and western Asia. The Pacific Ocean, Central and East Asia only exhibit smaller areas of significant changes. A small area over the East Asian mid-latitudes exhibits the only significant TEKE increase.

The ATL scenario shows a comparable TEKE reduction, while the only widespread significant area is found over Europe and Western Asia. Additionally, areas of significant decrease are evident over the Beaufort and Bering Seas.

The PAC ice loss causes a similar significant TEKE reduction near the Beaufort Sea, while the mid-latitude changes are more sparse and scattered compared to ARC and ATL. The PAC scenario exhibits significant reductions over the central Atlantic Ocean (in the southernmost part of the Figure 5.6, bottom row plot) and parts of the Middle East. A small region in the Eastern Atlantic near the west coast of Europe agrees with the TEKE reduction in the two other scenarios, but otherwise there are no significant TEKE changes over continental Europe.

While the geopotential height and zonal wind changes over Eastern Asia revealed reasonable agreement between the three scenarios, the TEKE shows some contrasting changes. PAC and ATL both show smaller areas of significant, but limited magnitude, TEKE decrease over East Asian mid-latitudes. In comparison, ARC exhibits a region of increased TEKE near the coast. This may indicate non-linearity in the circulation response: the forcing in the ATL and PAC scenarios favor similar changes, but the combination of the two favors a different response.

It has been suggested that sea ice loss could lead to more persistent mid-latitude weather through zonal wind reduction and increased meandering of the planetary waves (*Francis and Vavrus*, 2012). These findings regarding mid-latitudes weather patterns are, however, subject to ongoing scientific debate (*Screen and Simmonds*, 2013; *Barnes*, 2013; *Wallace et al.*, 2014).

Generally, our analysis of the atmospheric circulation does suggest a link between Arctic sea ice loss and mid-latitude weather. Significant mid-latitude reductions of zonal wind and TEKE are found in all three scenarios, albeit in varying regions and extent. The TEKE anomalies indicate a reduced variability of the mid-latitude winds that would be consistent with weakening or less frequent passage of the weather systems. While our analysis cannot reveal the mechanism behind the changes, the TEKE results could lend support to the idea of more persistent mid-latitude weather (as suggested by *Francis and Vavrus* (2012)).

Several studies have identified links between Arctic sea ice loss, circulation changes and cold winters in Europe and parts of Asia (*Petoukhov and Semenov*, 2010; *Yang and Christensen*, 2012; *Cohen et al.*, 2013; *Peings and Magnusdottir*, 2014; *Tang et al.*, 2013). Nevertheless, none of the three sea ice reduction scenarios result in colder winters in Europe or Asia (cf. Figure 5.4). *Outten and Esau* (2012) propose that the continental cooling is linked to a reduced meridional temperature gradient and the consequent reduction of the zonal wind. These conditions are apparent in multiple regions over Europe and Asia in all three simulations, but neither response shows significant cooling in these regions (compare Figure 5.4 and 5.6). There are two potential explanations for

this lack of cooling in our experiments. It could indicate a nonlinear nature of the atmospheric response to sea ice loss. Several studies suggest that a sea ice decline exceeding the current observations no longer favors the colder winter conditions (*Petoukhov and Semenov*, 2010; *Yang and Christensen*, 2012; *Peings and Magnusdottir*, 2014). The sea ice loss applied here is relatively strong and widespread, and could be too extensive to cause the cold Eurasian winters. Alternatively, this particular model might not favor the circulation changes that cause the colder winters.

We will further investigate the circulation changes by examining the North Atlantic Oscillation (NAO). The NAO describes the leading mode of atmospheric variability in the North Atlantic region and is closely related to circulation changes affecting the wintertime climate of Eurasia and the Arctic (*Hurrell*, 1995; *Wanner et al.*, 2001; *Hurrell et al.*, 2003; *Hurrell and Deser*, 2010; *Bader et al.*, 2011).

5.3.3 NAO

The link between the NAO and sea ice cover has been investigated by several other studies (*Magnusdottir et al.*, 2004; *Deser et al.*, 2004; *Kvamstø et al.*, 2004; *Seierstad and Bader*, 2008; *Strong and Magnusdottir*, 2010; *Jaiser et al.*, 2012; *Peings and Magnusdottir*, 2014). Despite varying conclusions, there seems to be widespread agreement that Arctic sea ice loss favors the negative mode of the NAO (*Vihma*, 2014). In our experiments, the NAO index shows no significantly different response to the varying patterns of sea ice loss (not shown), but further analysis reveals that the circulation pattern is indeed affected.

Empirical Orthogonal Function (EOF) analysis has been performed for the North Atlantic region in order to assess the circulation changes in more detail. The leading mode of variability in the sea level pressure, i.e. the first EOF, is a representation of the NAO (*Kutzbach*, 1970; *Deser*, 2000; *Hurrell et al.*, 2003). The analyzed region covers 20° – 80°N and 90°W – 40°E (following (following *Hurrell*, 1995; *Hurrell and National Center for Atmospheric Research Staff (Eds.)*, 2015)), and the analysis is based on sea level pressure weighted by the square root of cosine of the latitude. The first EOF, presented in Figure 5.7, reveals that the NAO is the dominant mode of variability in all simulations. The NAO describes similar fractions of the variability in all four simulations: 45.8 %, 55.9 %, 43.4 %, and 42.7 %, respectively in CTRL, ARC, ATL and PAC. The spatial pattern, however, reveals a difference in response to the varying sea ice reductions.

While the leading EOFs in the four simulations all are similar to the observed NAO pattern, the shape and position of the two extremes appear to shift with the different sea ice reductions. The location of the two extremes of the EOF can be interpreted as "centers of action", representing the mean locations of the "Icelandic Low" and "Azores High" that forms the NAO pattern in terms of sea level pressure. To visualize the potential shift, the locations of the centers of action are marked in Figure 5.7: The grid cells with the ten highest and ten lowest values in the region are marked with white dots to illustrate the locations of the maximum (the Azores High) and the minimum (Icelandic Low).

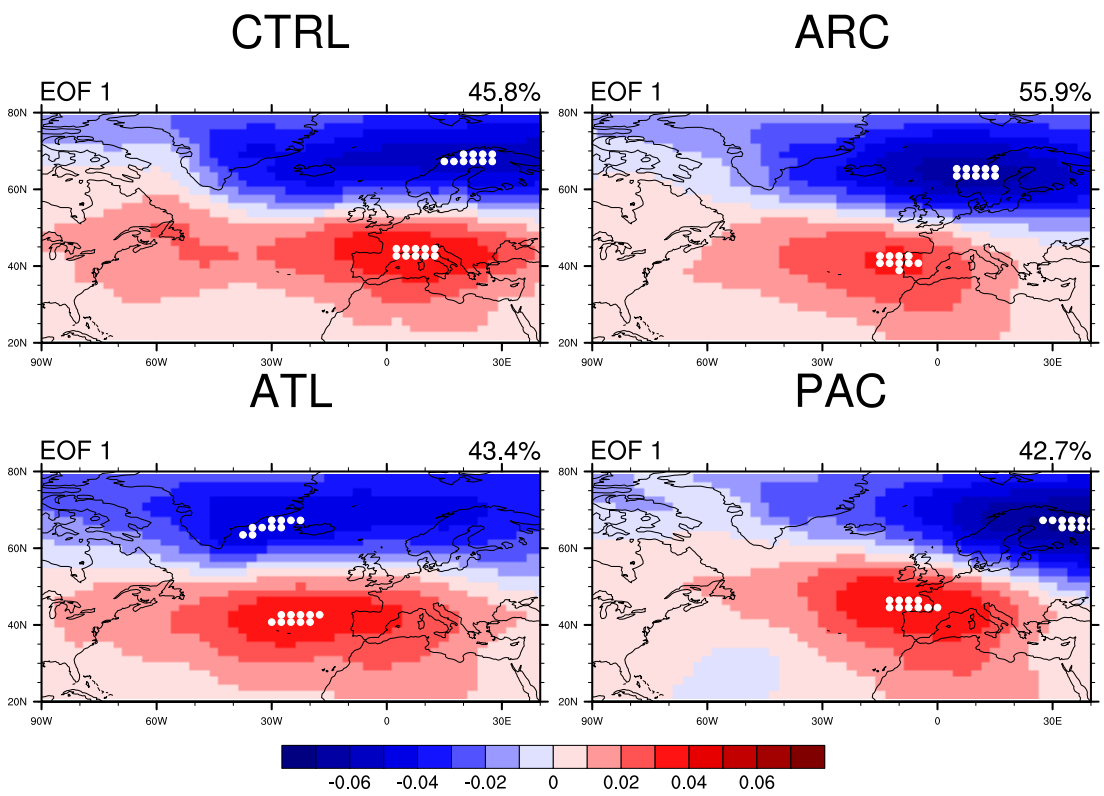

Figure 5.7: The first EOF of the winter (DJF) mean weighted sea level pressure in the four simulations. The weight on the particular mode of variability is shown in the upper right corner of each plot. White circles mark the location of the ten highest and lowest values, thus indicating the locations NAO centers of action.

To further investigate the robustness of this shift, we employ a bootstrap analysis (*Efron and Gong*, 1983; *von Storch and Zwiers*, 2001) where a resampling procedure presents an estimate of the variance in the dataset based on a large number of random subsets from the dataset. Similarly to the approach from *Wang et al.* (2014), a total of 500 random 30-year samples are drawn with replacement from the 30 years that form the analyzed climatology. Based on each 30-year sample, we conduct a new identical EOF analysis and calculate the location of the centers of action. The centers of action from the bootstrap analysis are presented in Figure 5.8. As in Figure 5.7, the ten highest and lowest values from each sample are used to assess the locations of the minimum and maximum. This assures more robust distributions compared to only selecting one maximum and one minimum location from each sample.

The bootstrap analysis reveals some variance in the location of the centers of action. Nevertheless, the location of the northern center of action appears sensitive to the location of sea ice loss and some clear groupings appear for each of the simulations. The overall tendency is that the CTRL centers group near the Icelandic east coast, the ARC ice reduction shifts the grouping eastward, the PAC ice reduction even further eastward, and the ATL reduction triggers an opposite shift westward from the CTRL grouping. The southern center shows no similar clear shifts or groupings; most of the locations are clustered around 40°N, 0°E. The ATL westward shift and the PAC eastward shift are

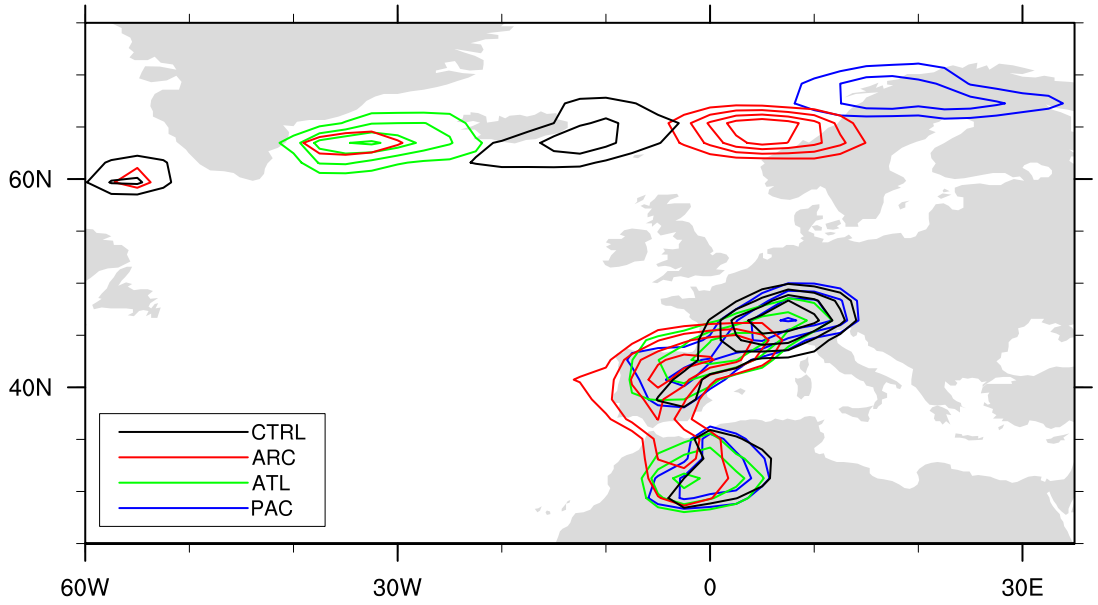

Figure 5.8: The location of the wintertime (DJF) NAO centers of action are illustrated through the location of the ten highest and ten lowest values of the leading EOF from each bootstrap sample. Contours show the total number occurrences in each grid cell combining all 500 samples: CTRL in black, ARC in red, ATL in green and PAC in blue. The contour interval is 50 counts with the lowest contour at 50. Only a subset of the analyzed region is displayed; spurious counts over the Great Lakes in North America are not shown.

both of 20–30° longitude (cf. Figure 5.8). The combined ARC reduction caused a less pronounced eastward shift; reminiscent of a linear combination of the ATL and PAC shifts or slightly eastward hereof. This is one of the few examples that suggest any kind of quasi-linear responses, when comparing the sum of ATL and PAC to ARC.

As described by *Wang et al.* (2014), bootstrap analysis is an advantageous method to assess the spatial variability of the EOF-based NAO pattern, and can illustrate the uncertainty of the location of the NAO centers. Hence, our Figure 5.8 provides more information on the spatial changes of the NAO pattern compared to Figure 5.7. The bootstrap reveals that the some of the center locations found based on the single EOF in Figure 5.7 are not representative of the complete data set. Notable differences are seen in the locations of the northern center in the CTRL experiment and the southern center in the ATL.

Shifts in the location of the NAO centers of action are known from several other studies. An eastward shift has been identified in observations from the late 1970s (*Hilmer and Jung*, 2000; *Jung et al.*, 2003; *Dong et al.*, 2011) and in climate modelling studies of increasing greenhouse gas scenarios (*Ulbrich and Christoph*, 1999; *Hu and Wu*, 2004; *Dong et al.*, 2011). Recently, *Wang et al.* (2014) also identified this significant eastward shift using bootstrap analysis of reanalysis data.

Using GCM simulations *Ulbrich and Christoph* (1999) found a shift in the NAO pattern, which was not captured by the NAO index. The simulations were forced with increasing greenhouse gas concentrations, and the authors identified increased storm track activity in combination with a north-eastward shift of the NAO northern center of action. Their

pre-industrial control climate and years with low forcing had the northern center of action located at the Greenlandic south-east coast, while it shifted into the Nordic Seas (northeast of Iceland) when the forcing exceeded 3 W m^{-2}. The shift was accompanied by an increase of the westerlies in the North Atlantic region. This corresponds well to the results of the PAC scenario here, where the eastward shift is accompanied by zonal wind increase over the North Atlantic (the wind speed increase here is, however, statistically insignificant). *Ulbrich and Christoph* (1999) conclude that the reason for the observed shift "remains an open question", and unfortunately there is no mention of sea ice changes or surface-warming patterns in the paper.

Dong et al. (2011) identify a similar eastward shift of the NAO centers of action in both observations and a series of AGCM experiments with increased CO_2 and SST. While the eastward shift is similar to the response in our PAC ice loss simulation, the simulations by *Dong et al.* (2011) only exhibit significant Arctic warming near the Barents Sea, indicating that this is also the only region with chance of substantial sea ice loss.

Peterson et al. (2003) investigated the mechanism of the pattern shift by performing experiments with a primitive equation atmospheric model. Their results revealed a nonlinear dependence of the spatial pattern of the NAO on the NAO index. They found an eastward (westward) shift in connection with high (low) NAO indices. Our results do, however, indicate that such shifts can occur even without a clear trend in the NAO index.

5.4 Conclusions

All of the three idealized sea ice loss scenarios (ice loss in the entire Arctic and in the Atlantic and Pacific sectors only) result in substantial wintertime warming. The warming is driven by turbulent heat fluxes from the newly ice free ocean, and is to a large extent confined to the region of sea ice loss. The Arctic region exhibits an overall warming in all three scenarios, but ice loss in the Pacific sector of the Arctic (such as the observed extent in 2007) only causes limited warming over the Greenland Ice Sheet.

The simulations show that the mid-latitude atmospheric circulation is affected by sea ice loss. All three simulations show increased geopotential height at high latitudes near the regions of sea ice loss. There is, however, no direct overlap between the spatial patterns of near-surface warming and geopotential height at the 500 hPa level; substantial surface-based warming can occur without significant increase of the geopotential height directly above. As expected from the thermal wind relation, the decreased meridional gradient in geopotential height causes a general reduction in zonal wind strength. Significant wind reductions are found south of areas of increased geopotential heights in all experiments. The three ice loss scenarios all cause reduced mid-latitude zonal winds over Europe and Eastern Asia. Substantial mid-latitude wind reductions are found over the Atlantic Ocean in both ARC and ATL, while no significant changes are evident in PAC. The circulation patterns indicate a non-uniform atmospheric sensitivity to the location of ice loss. While some regions show a similar atmospheric response to the different scenarios (e.g. decreased zonal flow over central Europe and East Asian mid-latitudes), it is clear that other regions are sensitive to the location of the sea ice loss. Particularly the North Atlantic Oscillation exhibits a high sensitivity.

This study, in line with several previous studies, demonstrates a link between the Arctic sea ice cover and the North Atlantic Oscillation. While no clear trend is found in the NAO index, the spatial structure of the NAO pattern appears sensitive to the location of the ice loss. We find that the sea ice loss in the Pacific region of the Arctic tends to shift the northern center of action of the NAO eastward, while the sea ice loss in the Atlantic region causes a westward shift. Clarification of the exact mechanism behind this link will require further investigation.

6 Comparing the impacts of different forcing types

The combined ensemble of the experiments presented here, provides at test bed for analyzing the mechanisms in a warming climate. This chapter presents analyses that intercompare the results of the two main parts of this project (the paleoclimate experiments and the sea ice loss experiments) with special attention on the Arctic climate. Table 6.1 presents an overview of the complete ensemble of simulations from the two sets of experiments. The two sea ice experiments with increased CO_2 (CO2 and ARC+CO2) have not been described previously; they are only used in this section to illustrate the impact of CO_2 increase.

Name	**Model**	**Setup**	**CO_2**	**Solar**	**SST**	**Sea ice**
PI	EC-Earth	Coupled	PI	PI	Active[1]	Active[1]
LIG	EC-Earth	Coupled	LIG	LIG	Active[1]	Active[1]
iP+oP	EC-Earth	AGCM	PI	PI	PI	PI
iL+oL	EC-Earth	AGCM	LIG	LIG	LIG	LIG
iL+oP	EC-Earth	AGCM	LIG	LIG	PI	PI
iP+oL	EC-Earth	AGCM	PI	PI	LIG	LIG
iP+oP-ice	EC-Earth	AGCM	PI	PI	PI	LIG
CTRL	CESM	Slab	CTRL	PI	Active[2]	CTRL
ARC	CESM	Slab	CTRL	PI	Active[2]	ARC
ATL	CESM	Slab	CTRL	PI	Active[2]	ATL
PAC	CESM	Slab	CTRL	PI	Active[2]	PAC
CO2	CESM	Slab	2×CTRL	PI	Active[2]	CTRL
ARC+CO2	CESM	Slab	2×CTRL	PI	Active[2]	ARC

Table 6.1: Overview of all simulations in this project: EC-Earth paleoclimate experiments (upper two sections) and CESM sea ice experiments (bottom section). CTRL CO_2 level indicates the pre-industrial default in CESM (equivalent to PI in EC-Earth).
[1] Computed by full ocean and sea ice models (NEMO and LIM3)
[2] Computed by slab ocean model

6.1 The impact of sea ice loss on Greenland climate

Chapter 4 revealed how sea ice may impact the conditions on the Greenland ice sheet during the last interglacial. The following section will present a more detailed look at the Greenland response to the varying sea ice forcings from Chapter 5, and discuss how the response compares to the LIG experiments. As noted in Chapter 5, the apparent limited impact of the PAC sea ice loss on Greenland climate is relevant for both future projections and paleoclimate assessments of ice sheet changes. Hence, the following section presents more details on the response over Greenland; both for temperature, precipitation, and potential impact on the ice core records.

Figure 6.1 presents a detailed look on the warming over GrIS in the sea ice scenarios, reiterating the relatively limited impact of the PAC sea ice loss. Especially the PAC wintertime (DJF) response is noteworthy: the peak Arctic warming is found during winter, but the temperature on GrIS is completely unaffected. Evidently, the circulation does not favor advection from the PAC sector towards Greenland.

The atmospheric stability combined with the barrier effects of the ice sheet slopes and the local circulation further means that the heat which does reach the Greenland vicinity has a very limited impacts over the interior ice sheet are limited. Even the very strong local warming in ARC and ATL has a more limited impact on the interior, elevated part of the ice sheet. Figure 6.2 presents the vertical structure of warming near the central GrIS, illustrating this pattern (compare with Figure 4.10 for the Eemian).

The vertical structure of warming near Greenland reveals high similarity with the Eemian pattern during the colder seasons (fall – spring). This is another illustration of the surface-based warming that dominates the Eemian Arctic climate in all seasons, except during the summertime insolation increase.

An interesting feature of the cross-sections in Figure 6.2 is that the warming appears to have a larger vertical extent east of Greenland. This difference applies to majority of the seasonal means in all three scenarios. This could be related to the circulation pattern and/or varying lower-atmosphere static stability east and west of Greenland. During the colder seasons, the latter could be a factor due to the different sea ice regimes along the eastern and western Greenland coasts: the east coast sea ice is primarily pack ice exported from the Arctic Ocean and only has a limited extent from the coast, while the Baffin Bay sea ice cover primarily consists of seasonal "locally-formed" sea ice covering the entire bay for part of the year (albeit the concentration is reduced in ARC and ATL). The shorter distance to open ocean on the east coast could be the reason for the larger vertical extent of the warming; this will be investigated in detail below (Section 6.2).

In assessments of the GrIS response in a warming climate, it is obviously important also to consider the precipitation on the ice sheet. It is not given that the temperature and precipitation responses are linked, but the PAC ice loss again seems to have a limited impact on the ice sheet. The snowfall anomalies are presented in Figure 6.3.

The sea ice loss generally favors a snowfall increase on Greenland, peaking during the colder seasons. The spatial pattern of the anomalies in ARC and ATL are relatively

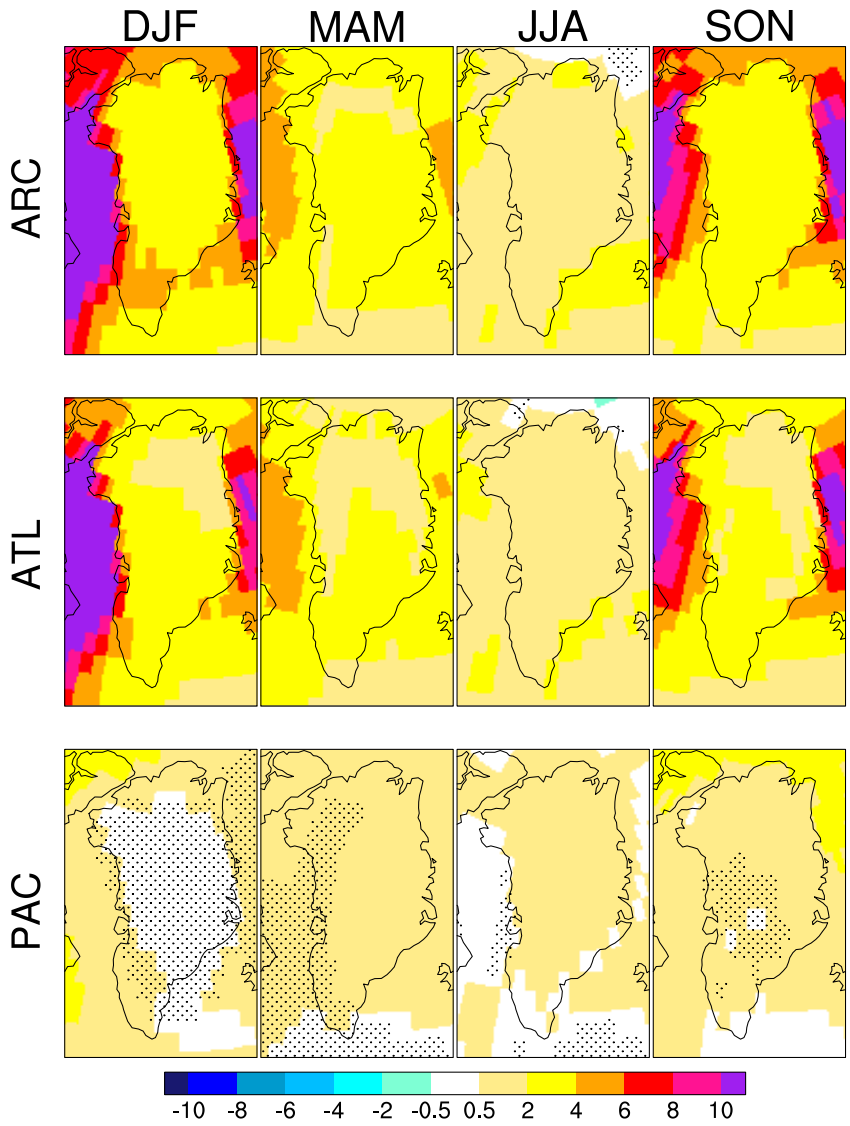

Figure 6.1: Greenland seasonal mean near-surface temperature anomalies [K] compared to CTRL: ARC (top), ATL (mid), and PAC (bottom). Black dotted shading marks anomalies that are not significant at the 95 % confidence level. This figure is a zoom of Figure 5.4 using the colorbar from 4 to facilitate direct comparison.

similar, with the most pronounced increase near the south-east coast (somewhat resembling the response to the sea ice loss and SST increase in the Eemian simulations; Figure 4.4). The apparent decrease in snowfall in the coastal areas during summer is related to the warming in ARC and ATL: the total precipitation is not reduced, but the relative fraction of rainfall is increased. The PAC ice loss also increases snowfall at the south-east coast (albeit a more limited change), but almost no significant changes are simulated anywhere else on the ice sheet. Hence, both the limited response in PAC and the high resemblance of ARC and ATL indicate that the local sea ice conditions have a larger impact over Greenland. It should be noted that the lack of significant changes in PAC could be related to the very dry conditions over the ice sheet and the relatively short simulation ensembles of 30 years.

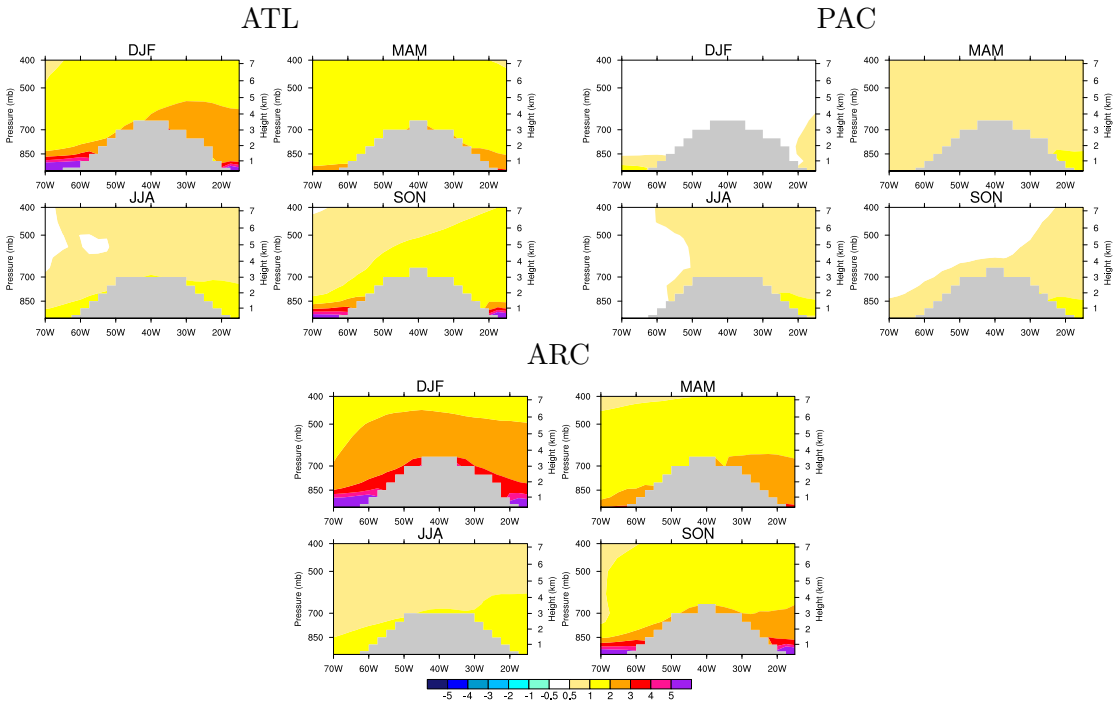

Figure 6.2: Greenland seasonal mean vertical temperature anomalies [K] along 75°N relative to CTRL: ATL (top, left), PAC (top, right), and ARC (bottom).

From a paleoclimate perspective, the sea ice loss impacts the Greenland ice core records through temperature and snowfall changes. As in Chapter 4, we have calculated the precipitation-weighted temperature mean as the best representative of the ice core record. The precipitation-weighted mean is compared to the classical annual mean in Figure 6.4.

Comparison of T_{ANN} and T_{PW} reveals that the changes in the precipitation seasonality gives more weight to the colder seasons over the central ice sheet, especially in ARC and ATL. Otherwise T_{PW} largely resembles the time-averaged T_{ANN}. One interesting feature in the PAC scenario is that the precipitation changes gives increased weight to the warmer seasons in the northwestern part of the ice sheet. This could be a hint of a potential larger sensitivity to PAC ice loss in this region, e.g. at the NEEM ice core site. This again highlights the potentially important impact of sea ice changes during the LIG: The magnitude and location of the sea ice changes have a large impact on GrIS conditions and the ice core records.

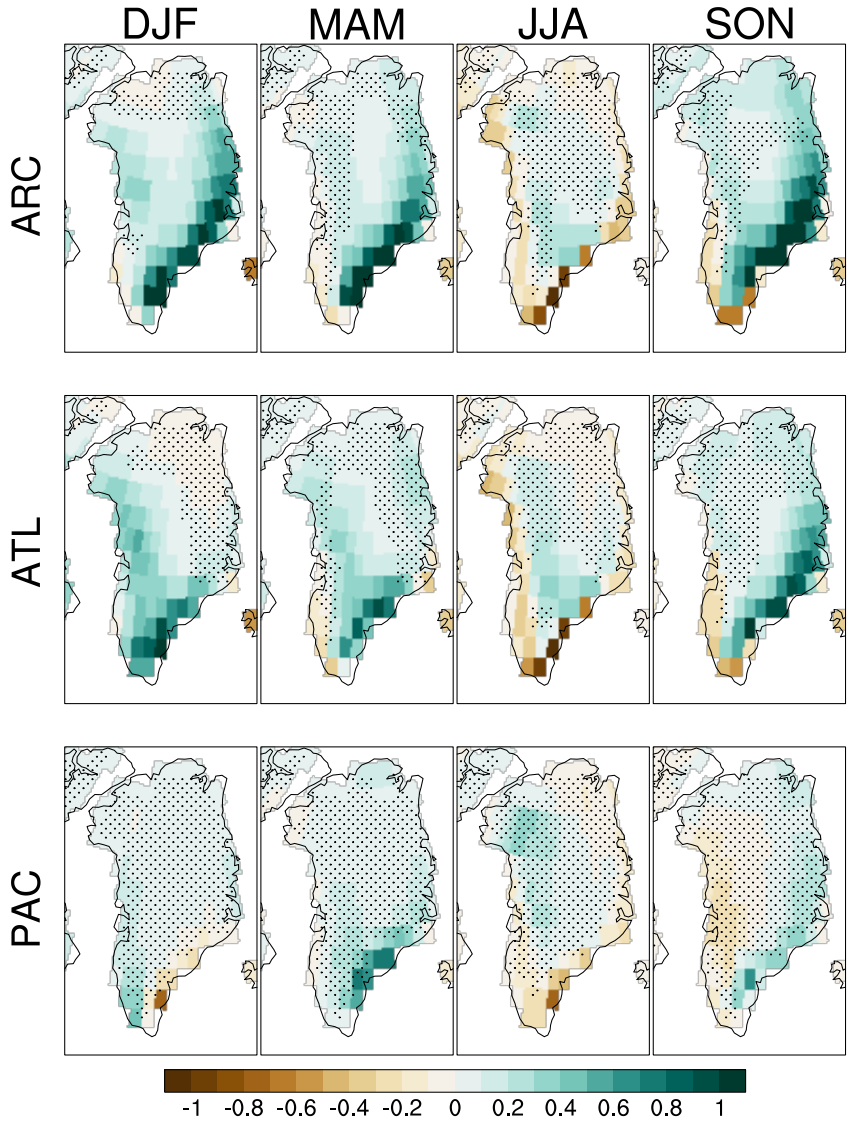

Figure 6.3: Greenland seasonal mean snowfall anomalies [mm/day] compared to CTRL: ARC (top), ATL (mid), and PAC (bottom). Black dotted shading marks anomalies that are not significant at the 95 % confidence level.

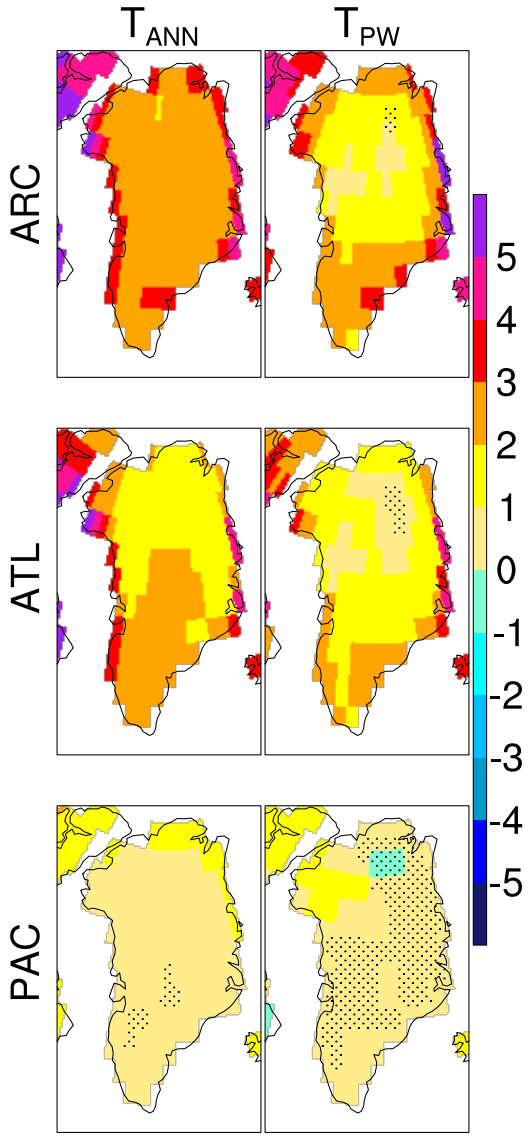

Figure 6.4: Greenland seasonal annual mean (T_{ANN}) and precipitation-weighted (T_{PW}) temperature anomalies [K] compared to CTRL: ARC (top), ATL (mid), and PAC (bottom). Black dotted shading marks anomalies that are not significant at the 95 % confidence level.

6.2 Vertical structure of warming

The Arctic wintertime low-level atmosphere is very stably stratified and surface-based inversions are frequent (*Serreze et al.*, 1992; *Zhang et al.*, 2011). Both sets of climate model experiments simulate strong near-surface warming that could potentially decrease or completely break down the stable stratification. Previous studies have found that sea ice loss could dramatically reduce low-level stability and increase wintertime atmospheric convection (e.g. *Abbot and Tziperman*, 2008). This could impact the Arctic climate system, and alter the strengths of the feedbacks that are dominant during present-day conditions. As an example, *Bintanja et al.* (2011) illustrate how the thermal inversion structure dampens the longwave cooling to space during near-surface warming (e.g. related to sea ice loss). Reduced low-level stability could thus potentially reduce the near-surface warming impact of sea ice loss. Figure 6.5 shows the wintertime mean lower atmospheric stability, indicated by the temperature difference between the 1000 and 850 hPa levels.

From the inversion assessment in Figure 6.5 it is clear that the Arctic region has very stable near-surface conditions during winter. The inversion structure persists over the sea ice cover even during substantial near-surface warming (e.g. in ARC, CO2, ARC+CO2, and LIG). Interestingly, the warming from the CO_2-doubling has no visible impact on the inversion structure when the sea ice is unchanged (comparing CO2 to CTRL and ARC+CO2 to ARC). The very persistent inversion structure might, however, be exaggerated by the two climate models: as mentioned in *Pedersen et al.* (2016a), previous studies have found that most climate models (including CESM) tend to overestimate the stability during the Arctic winter (*Boé et al.*, 2009; *Barton et al.*, 2014). Revisiting the discussion from Section 6.1, it appears that the low level stability cannot explain the larger vertical extent of warming east of Greenland (relative to west of Greenland). The sea ice reduction in ARC and ATL is large enough to practically break down the stability both east and west of Greenland. Comparing the inversions structures here and the vertical warming cross-sections (Figure 6.2) it appears that the differential elevated warming east and west of Greenland is due to the atmospheric circulation patterns rather than the local static stability.

The vertical structure of Arctic warming can be used as an indicator of the relative contributions of local and remote warming sources (*Graversen et al.*, 2008; *Screen and Simmonds*, 2010b; *Chung and Räisänen*, 2011). The idea is that surfaced-based warming peaks at the surface (e.g. *Serreze et al.*, 2009), whereas elevated warming peaks indicate a non-local heat source. Figure 6.6 shows the seasonal mean vertical structure of warming in the Arctic (60–90°N) for the sea ice experiments.

In line with the previous description (in *Pedersen et al.*, 2016a) and the Greenland cross-sections above, the Arctic mean warming from sea ice loss is confined near the surface (especially during the cold seasons). The near-surface warming is more limited during summer (JJA) when all excess heat contributes to additional snow and ice melt. Hence, the near-surface temperature remains near the freezing (thawing) point as long as snow or ice is present in the vicinity. The CO_2-driven warming causes a more vertically uniform warming signal. The warmer atmosphere contains more moisture, and increased

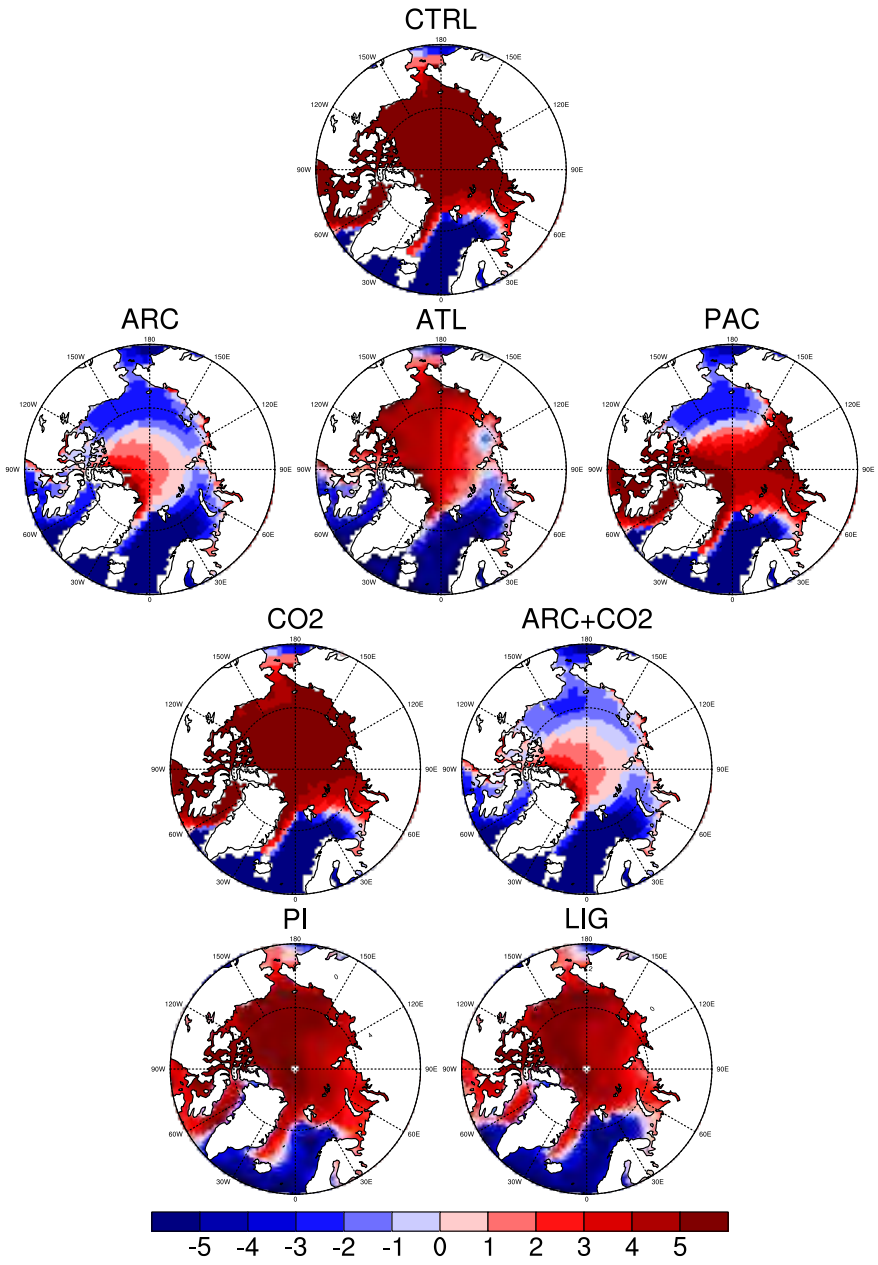

Figure 6.5: Wintertime low-level thermal inversions illustrated by the DJF seasonal mean difference T(850 hPa) – T(1000 hPa): Positive values indicate existence of a surface-based inversion.

longwave absorption from CO_2 and water vapor spreads the warming throughout the atmospheric column. An interesting feature of the summertime warming is a secondary warming peak aloft (near 400 hPa). This elevated warming peak suggests a remote warming source, i.e. an increased atmospheric heat transport into the Arctic (e.g. *Chung and Räisänen*, 2011). The changes in the poleward atmospheric heat transport are investigated in the following section (Section 6.3).

While surface-based changes are contributing substantially to the Eemian Arctic warming, the vertical profile of warming is different from the sea ice experiments. Figure 6.7

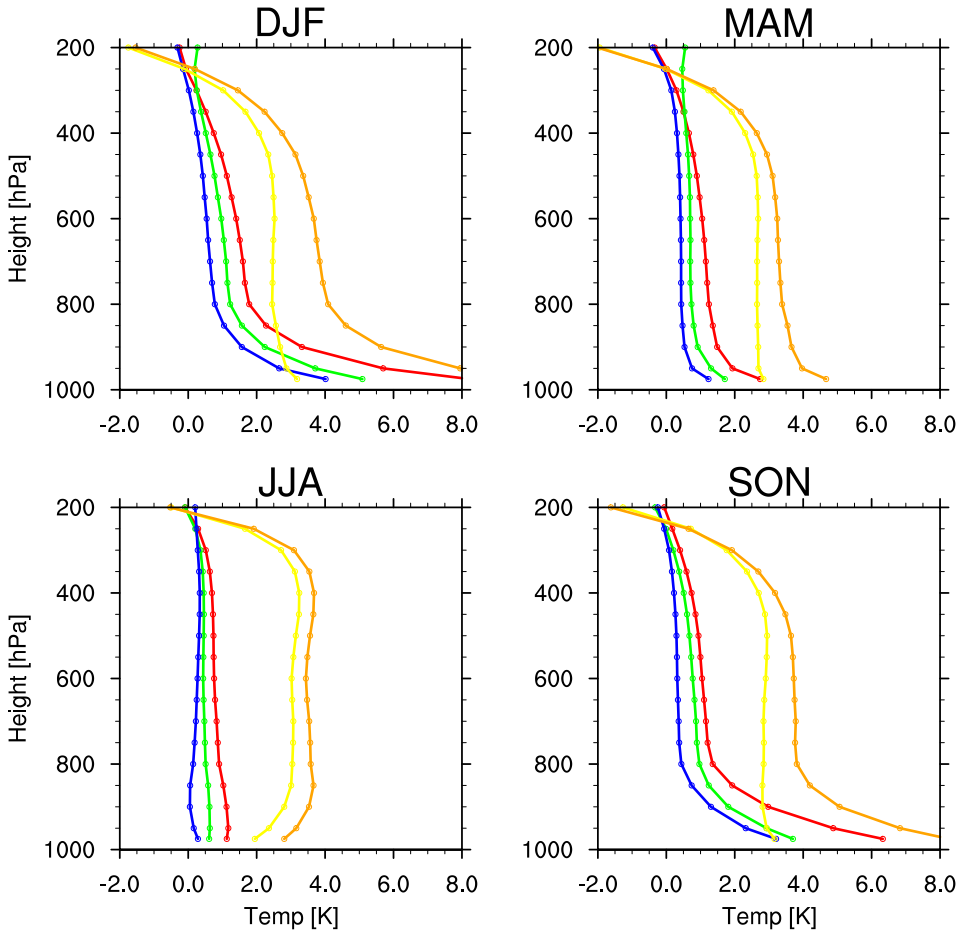

Figure 6.6: The vertical structure of Arctic (60–90°N) warming [K] in the five sea ice scenarios compared to CTRL: ARC (red), ATL (green), PAC (blue), CO2 (yellow), and ARC+CO2 (orange).

compares the warming in the AGCM Eemian experiments, and reveals warming aloft that is not related to the surface-based changes.

While the near-surface warming is less pronounced compared to the sea ice experiments (Figure 6.6), both iL+oL, iP+oL, and iP+oP-ice exhibit peak warming at the surface during fall, winter, and spring. The less pronounced warming matches the more limited sea ice changes, especially in the central Arctic. The cold season warming appears to have a larger vertical extent, perhaps indicating that EC-Earth simulates a weaker low-level stability. During the colder seasons (DJF, MAM, and SON) iP+oP-ice indicates that the sea ice alone explains a considerable part of the warming; the increased SSTs in iP+oL do, however, provide an additional warming contribution. During summer the sea ice loss alone provides no warming impact; as the SSTs are fixed the albedo feedback is essentially disabled. Comparison to the sea ice experiments (Figure 6.6), however, reveals that including the SST increase directly related to sea ice loss only results in limited summertime warming.

Generally, the Arctic mean warming response appear quasi-linear throughout the atmospheric column, i.e. the iL+oL response resembles the sum of iP+oL and iL+oP.

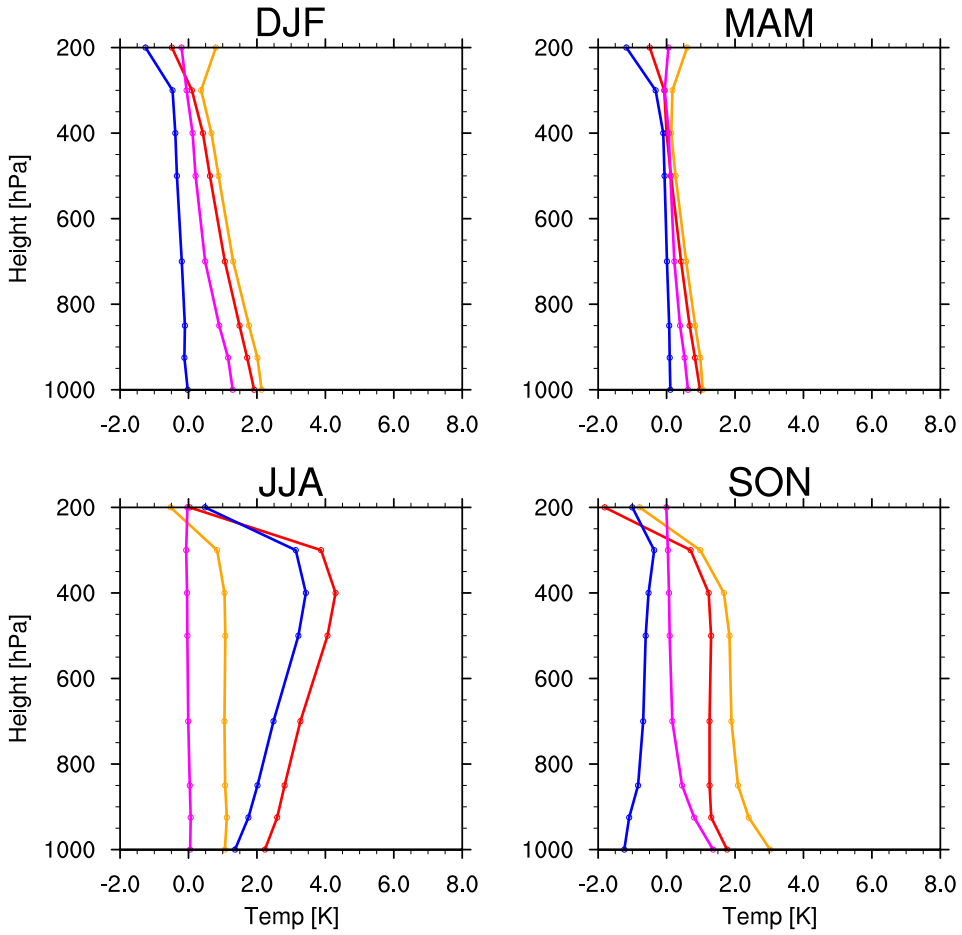

Figure 6.7: The vertical structure of Arctic (60–90°N) warming [K] in Eemian AGCM experiments (compared to iP+oP): iL+oL (red), iL+oP (blue), iP+oL (orange), and iP+oP-ice (magenta).

During summer, the Eemian insolation appear to cause an upper-level warming peak; peak warming is observed near 400 hPa in iL+oL and iL+oP, but not in iP+oL. Again, this elevated warming could indicate an increased atmospheric heat transport into the Arctic. We will investigate the atmospheric meridional heat transport in the following section.

6.3 Atmospheric meridional heat transport in a warming climate

The atmospheric meridional heat transport (MHT) is important for the relative warming of high and low latitudes, and is a contributing factor to Arctic amplification under GHG driven warming (*Alexeev et al.*, 2005; *Graversen et al.*, 2008; *Serreze and Barry*, 2011; *Graversen and Burtu*, 2016). In a simplistic view, the MHT is a response to the differential heating at high and low latitudes. The transport is therefore sensitive to the strength of the meridional temperature gradient, and thus to changes in the Arctic climate. In detail, the MHT is a moist static energy flux (in this context we do not consider the kinetic energy contribution) which consists of three contributions (e.g.

Serreze and Barry, 2005):

$$\mathrm{MHT} = \oint \int_0^{p_s} v \left(c_p T + gz + L_v q\right) \frac{\mathrm{d}p}{g} d\bar{x} \tag{6.1}$$

where p_s is the surface pressure (height), c_p the specific heat of the atmosphere at constant pressure, T the temperature, L_v the latent heat of evaporation, q the specific humidity, g the gravitational acceleration, z the geopotential height, and $\bar{x}$ is the spatial coordinates (latitude and longitude). The sum of the two first terms ($c_p T + gz$) is called the dry static energy (DSE), while the latter ($L_v q$) is the latent heat transport. The equation illustrates that it is not straightforward to predict the MHT response directly from the the meridional temperature gradient offset, as only the DSE depends directly on the temperature.

From the model output, we calculate the implied energy transport based on the zonal mean flux imbalance. Starting the iteration from the South Pole, the flux imbalance in the zonal band must correspond to the northward flux into the next grid cell band. The zonal mean implied northward MHT from zonal band n to $n+1$ can thus expressed as:

$$\begin{aligned}
\mathrm{MHT}^{(n)} &= \Delta F^{(n)}_{\mathrm{SFC}} + \Delta F^{(n)}_{\mathrm{TOA}} + \Delta F^{(n)}_{\mathrm{latent}} + \mathrm{MHT}^{(n-1)} \\
&= F^{(n)}_{\mathrm{SW,SFC}} + F^{(n)}_{\mathrm{LW,SFC}} + F^{(n)}_{\mathrm{LH,SFC}} + F^{(n)}_{\mathrm{SH,SFC}} \\
&\quad + F^{(n)}_{\mathrm{SW,TOA}} + F^{(n)}_{\mathrm{LW,TOA}} + F^{(n)}_{\mathrm{LH,PREC}} + \mathrm{MHT}^{(n-1)}
\end{aligned} \tag{6.2}$$

where SFC and TOA denotes surface and top-of-the-atmosphere, SW is shortwave radiation, LW is longwave radiation, and LH and SH are latent and sensible heat fluxes. The superscript parentheses indicate the zonal grid cell band (starting at n=1 at the South Pole, therefore MHT(0) = 0 per definition), and $F_{\mathrm{LH,PREC}}$ indicates the latent heat release related to precipitation as $F_{\mathrm{LH,PREC}} = L_v\ \rho\ (P_{\mathrm{LS}} + P_{\mathrm{CP}})$. This approach thus estimates the total and latent heat transports; the DSE is calculated as the difference between the two (cf. Eq. (6.1)).

6.3.1 MHT during the Eemian

The LIG insolation forcing is non-uniform (compared to e.g. globally uniform forcing from increased GHG concentration) with an annual net increase at high latitudes compensated by a reduction in the tropics (Figure 3.1). As discussed previously, this meridional gradient in the forcing is further strengthened by feedback mechanisms favoring high latitude (Arctic) warming. Figure 6.8 shows the response of the MHT in LIG compared to PI, calculated as the implied transports following Equation (6.2).

The annual mean Northern Hemisphere meridional temperature gradient is reduced substantially due to Arctic warming of 2.4 K and the unchanged temperature in the tropics (0.02 K increase). Consistently, the poleward DSE transport is reduced throughout the Northern Hemisphere. Despite partial, regional compensation by the latent heat transport, the total poleward MHT is reduced in LIG throughout the Northern Hemisphere. The earlier presented AMOC estimates, indicate that increased northward ocean heat transport is likely also contributing to the reduction of the MHT. The poleward heat transport south of 30°S is reduced in both latent heat and DSE. The simulated changes

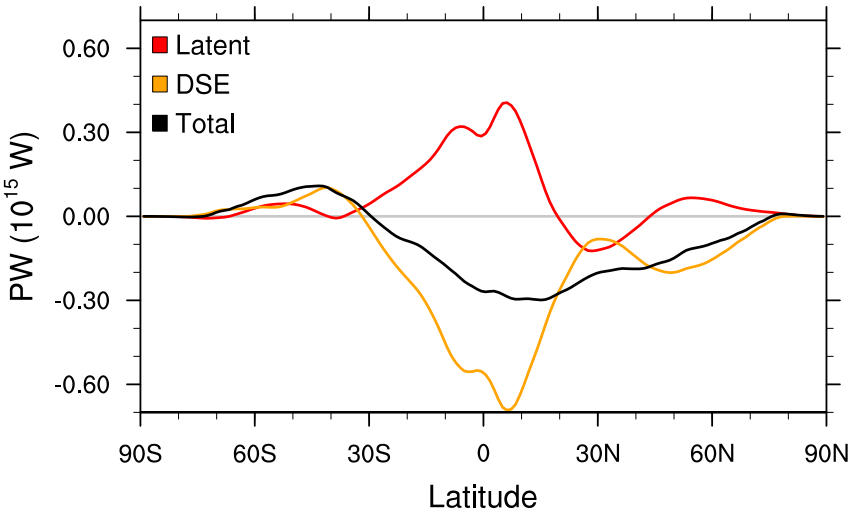

Figure 6.8: Implied meridional heat transport [PW] in LIG compared to PI. Total (black), latent heat (red), and dry static energy transport (orange). Positive values indicate northward transport.

have similar magnitude and meridional structure as found in experiments performed with ECHAM-5 by *Fischer and Jungclaus* (2010).

As before, the AGCM hybrid experiments can aid the interpretation of the full LIG response in the coupled simulation. Figure 6.9 reveals the relative impact of the insolation and the oceanic changes on the MHT.

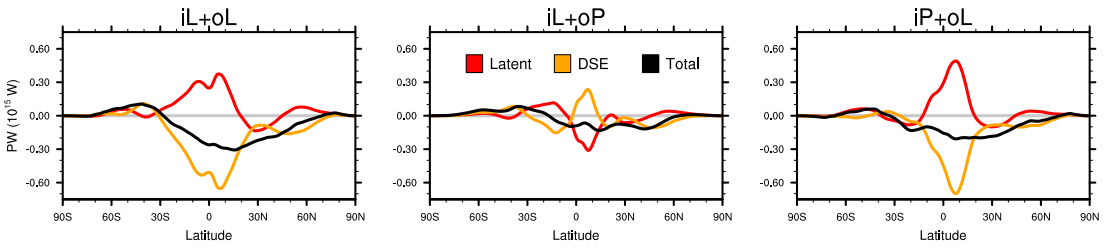

Figure 6.9: Implied atmospheric energy transport anomalies [PW] relative to iP+oP: iL+oL (left), iL+oP (center), and iP+oL (right). Latent heat (red), dry static energy (orange), and total energy transport (black).

Figure 6.9 indicates relatively linear behavior, i.e. iL+oL resembles the sum of iP+oL and iL+oP. While the cooling in the tropics offsets the meridional temperature gradient in iL+oP, the mid- to high latitude warming is much more pronounced in iP+oL. The changed sea surface conditions, and the related high-latitude warming, appear to be causing the largest decrease in northward DSE transport. The monsoon related cooling around 10°N in iL+oP causes a DSE input from the region south of the cooling belt, consistent with the local temperature gradient in the tropical region. Looking at the Arctic region, the MHT across 60°N is decreased in all three cases. Despite the dominant DSE transport decrease, both iP+oL and iL+oP indicate a minor latent heat transport increase into the Arctic region.

The summertime elevated Arctic warming peak displayed in Figure 6.7 indicate increased atmospheric heat transport into the Arctic. While there is no substantial change in the annual mean, our assessments indicate that the upper level warming is related to increased MHT into the Arctic. Opposite the three other seasons, the summertime warming peaks at Northern Hemisphere mid-latitudes and not in the Arctic (cf. Figures 3.4 and 3.8). Thus, the DSE transport which is responding to the temperature gradient could be increased during summer (rather than the expected decrease during the remaining seasons, where the Arctic supersedes mid-latitude warming).

Alternative sources of the upper-level warming could be increased absorption from clouds or moisture at this particular height. Despite a general increase of specific humidity q aloft during summer, neither humidity or cloud cover show any substantial anomalies near 400 hPa where the warming peak is observed (not shown). This further substantiates that the upper-level warming could be related to increased atmospheric heat transport.

6.3.2 MHT response to sea ice loss

The impact of Arctic changes on the MHT can be further assessed using the sea ice experiments. While the experiments indicate significant remote impacts of sea ice loss, the primary impact of the sea ice loss is a direct warming of the Arctic region. Figure 6.10 shows the hemispheric temperature gradients in the sea ice experiments, and clearly illustrates the central role of the Arctic sea ice in shaping the Arctic amplification (as described in Chapter 2): The CO2 experiment with CO_2 doubling but unchanged sea ice conditions exhibits the lowest ratio between high and low latitude warming. Nonetheless, Arctic warming is still amplified even without any sea ice response in CO2.

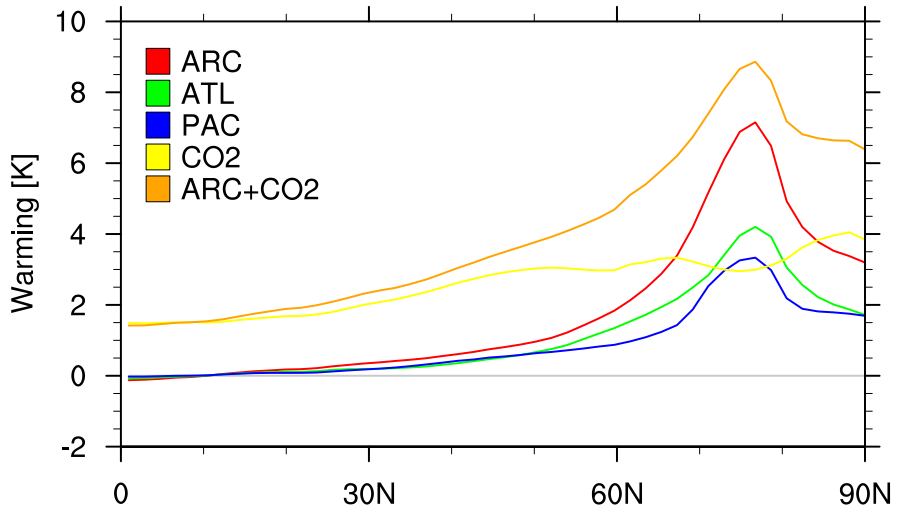

Figure 6.10: Northern Hemisphere zonal mean near-surface warming [K] in the five sea ice experiments compared to CTRL.

In these idealized experiments, the main sea ice loss is located near the margins of the Arctic region. The strong local warming over the areas of ice loss means that temperature

and moisture gradients are offset which could affect the heat and moisture transports into the central Arctic. Despite similar meridional temperature gradients, Figure 6.11 illustrates that the response of the MHT is indeed also very different with and without addition of CO_2-driven warming.

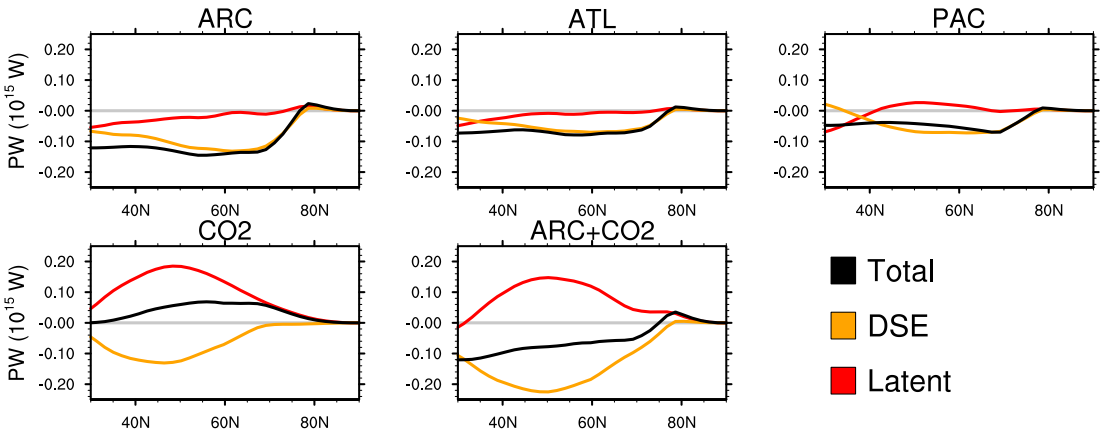

Figure 6.11: Implied atmospheric meridional heat transport anomalies [PW] compared to CTRL.

All three sea ice loss scenarios (ARC, ATL, and PAC) lead to decreased MHT into the Arctic driven by DSE decrease. The latent heat transport is largely unchanged at high northern latitudes. Hence, the isolated impact of the sea ice loss is the expected reduction of poleward heat transport. Furthermore, the ATL and PAC responses are similar, and sum approximately to the response in ARC.

Compared to the response in ARC, the CO_2 doubling in ARC+CO2 further decreases the DSE transport. The total transport, however, is almost unchanged as the GHG warming introduces a substantial, countering increase of latent heat transport. In absence of sea ice changes, the MHT anomaly in CO2 indicates that the latent heat increase is large enough to compensate the DSE decrease, resulting in a net increased MHT into the Arctic. The addition of sea ice loss in ARC+CO2 causes a MHT reduction; except in the high Arctic region where the increased latent heat transport more than outweighs the reduced DSE transport (positive net MHT between 75 – 80°N). This pattern reflects the prescribed sea ice changes: the sea ice concentration is unchanged north of 80°N, whereas the main warming occurs between 70–80°N.

Evidently, sea ice loss alone decreases heat transport towards high-latitudes; the increased northward latent heat transport which drives the net increase is dependent on low-latitude warming (*Alexeev et al.*, 2005; *Screen et al.*, 2012). As suggested by previous studies (*Alexeev et al.*, 2005; *Graversen et al.*, 2008; *Graversen and Burtu*, 2016), these experiments indicate that the (latent) MHT changes appear to contribute to amplified warming in Arctic. One important caveat related to our experiments is, however, that the sea ice loss and CO_2-driven warming are decoupled in the ARC+CO2 experiment; stronger sea ice loss under the same atmospheric conditions could alter the balance between the heat transport components.

7 Conclusions

7.1 Summary

The first part of this thesis investigates the last interglacial climate through simulations with the fully coupled EC-Earth model. The climatic response to the insolation change is further assessed through AGCM experiments used to separate the direct impact of insolation forcing from the impact of secondary sea surface warming and sea ice loss. Chapter 3 presented the following results:

- The simulated LIG climate revealed an annual mean temperature response resembling the multi-model mean from *Lunt et al.* (2013). While the spatial pattern is similar, the annual mean warming of 0.5 K is high compared to the multi-model ensemble. A prominent feature of the annual mean temperature pattern is a cooling over the tropical monsoon regions in India and northern Africa. The cooling is related to an intensified monsoon leading to increased precipitation and cloud cover. The most pronounced warming is simulated in the North Atlantic region in response to an increased AMOC and a northward retreat of the sea ice edge. The simulated North Atlantic warming shows fair agreement with proxy records, but does not capture the regional cooling suggested by the temperature reconstructions. Correlation and regression estimates suggest that the AMOC increase alone cannot explain the model-data discrepancy.

- The AMOC increase is associated with the activation of deep convection in the Labrador Sea (where it is absent in the PI simulation). The lack of convection in PI is likely a model bias that could be related to an excessive sea ice extent. It is, however, not possible to conclude whether the sea ice cover causes the convection shutdown or if the cooling from the shutdown favors sea ice growth. Similarly, it is challenging to assess the causality between the stronger LIG AMOC and the general salinity increase in the North Atlantic; increased AMOC results in higher salinity which further increases the convection strength.

- Despite a considerable northward retreat of the sea ice edge, there is no considerable changes in the central Arctic sea ice cover. The sea ice thickness is reduced compared to PI, but remains 2–4 meters in the central Arctic. Proxy records suggest reduced sea ice concentrations in the central Arctic during the Eemian. This discrepancy could be related to the model performance; EC-Earth is overestimating the sea ice extent in the present climate state.

- A series of AGCM simulations was used to separate the direct impact of the insolation and the indirect impact of changed sea surface conditions. These experiments revealed that the monsoon response was driven by the insolation, while the oceanic changes were important for the mid- to high northern latitude warming – especially in the Arctic, where the sea ice loss and SST increase prolongs the impact of the summertime forcing resulting in an all-year warming.

Chapter 4 continues with a detailed assessment of the last interglacial conditions on the Greenland ice sheet. The model simulations were analyzed with a focus on potential ice sheet changes and the climatic impact on the ice core records, leading to the following results:

- The simulated Eemian climate underestimate the warming on Greenland compared to reconstructions from the NEEM ice core. The hybrid AGCM experiments reveals that the largest contribution to GrIS warming is related to the changed SST and sea ice conditions. Estimates of the precipitation-weighted temperature, which accounts for changes in precipitation-seasonality, show that the direct impact of insolation and the indirect impact of oceanic changes would have comparable impacts on the warming signal in the NEEM ice core record. The precipitation-weighted mean is only marginally higher than the annual mean temperature indicating that the precipitation changes cannot explain the model deviation from the reconstructed temperature.

- The model–data discrepancy could be related to the experiment setup; in particular, related to the fixed present-day ice sheet topography. Firstly, a decrease of the ice sheet elevation would increase the near-surface temperature following the atmospheric lapse rate. Secondly, local circulation might be affected by altered ice sheet topography.

- Detailed calculation of the GrIS surface mass balance indicates that the insolation is the dominant factor behind the Eemian GrIS melt. This suggests that the Eemian temperature-melt relationship does not apply under greenhouse gas driven warming, making the Eemian a poor analogue for future ice sheet changes.

- The NEEM ice core indicates that melt events occurred on the interior ice sheet during the Eemian, but no occurrences of melt is simulated by the model. The modeled surface albedo is also largely unchanged on the central ice sheet, which could be related to the relative low surface temperature on GrIS. The Eemian Arctic warming is largely confined near the surface (especially during the colder seasons from fall to spring) and thus mainly affects the coastal, low-elevation parts of the ice sheet.

- Atmospheric circulation changes appear to impact the coastal regions. During summer, increased onshore winds coincide with warming regions in the eastern, northwestern and central-western coastal areas. This could indicate that the circulation anomalies cause heat advection further inland compared to PI. Nonetheless, the circulation changes appear too weak to impact the temperature on the most elevated parts of the ice sheet. Increased onshore wind on the southeastern coast during winter appear consist with the snowfall increases on the slope of the ice sheet.

- Our experiments show that the oceanic changes (SST and sea ice) are contributing considerably to the GrIS warming. Based on precipitation-weighted temperature estimates, our hybrid simulations indicate that the combined effect of sea ice loss and SST increase is responsible for 0.8–1.5 K warming recorded at the NEEM deposition site (annual mean temperatures indicate a warming impact of 1.9–2.5 K).

- A supplementary experiment simulating the isolated impact of sea ice loss revealed that sea ice loss alone can explain a considerable part of the warming on the ice sheet. The circulation response is very similar to the changes in iP+oL, but the snowfall is, however, largely unchanged. This could indicate that increased moisture from the warmer ocean surface is a prerequisite for the precipitation increase.

The analysis of the last interglacial climate revealed a large impact from changes in the sea ice cover. The second part of the thesis is dedicated to investigating the climate change mechanisms related to the Arctic sea ice cover both within and beyond the Arctic region. The idealized model study presented in Chapter 5 reached the following conclusions:

- The idealized ice loss scenarios all result in substantial wintertime warming, driven by turbulent heat fluxes and largely confined to the region of sea ice loss. All the scenarios cause an overall Arctic warming, but the PAC ice loss (such as the observed extent in 2007) only causes limited warming over the Greenland Ice Sheet.

- The Arctic sea ice loss affects the mid-latitude atmospheric circulation. Following the thermal wind relation, the mid-latitude zonal wind is reduced in all three scenarios, albeit in varying locations. While winds are reduced over Europe and Eastern Asia in all scenarios, only ARC and ATL favor reductions over the Atlantic Ocean.

- The North Atlantic Oscillation exhibits high sensitivity to the location of ice loss. Sea ice loss in the Pacific region of the Arctic tends to shift the northern center of action of the NAO eastward, while the sea ice loss in the Atlantic region causes a westward shift.

The final chapter intercompares results from the two parts of the project, and provides additional details on the varying impacts of the LIG insolation, sea ice loss, and CO_2 increase.

- The CESM sea ice experiments, which allows assessment of the isolated impact of sea ice loss, show that the Greenland temperature is less sensitive to sea ice loss in the PAC sector. The sea ice scenarios all lead to increased snowfall on the ice sheet throughout the year, but the PAC scenario again has a less substantial impact. The snowfall increase is smaller during summer, where the coastal areas also experience an increased occurrence of rainfall. From an ice core perspective, the changed precipitation seasonality means that the winter temperatures generally would gain more weight in the ice core records; one exception is that the PAC sea ice loss leads to an increased precipitation-weighted temperature in northwestern Greenland (e.g. at the NEEM ice core site).

- While the more local sea ice loss leads to larger Greenland warming, all three scenarios reveal that the warming is largely confined to the lower atmosphere and thus to the coastal, low-elevation parts of the ice sheet. The experiments from both models suggest that the stable low-level conditions persist over any remaining sea ice cover, even with substantial near-surface warming (as seen e.g. in LIG, CO2 and ARC+CO2).
- The vertical structure warming in the Eemian show strong surface-based warming similarly to the sea ice experiments. The summertime warming, however, exhibits different structures, as the experiments with Eemian insolation (iL+oL and iL+oP) and with CO_2 warming (CO2 and ARC+CO2) feature an elevated warming peak near 400 hPa. This upper-level warming indicates warming from remote sources, i.e. through increased poleward heat transport during summer.
- The meridional heat transport (estimated from zonal mean flux imbalances) indicates that sea ice loss generally works to reduce the poleward heat transport. An important note is, however, that the general warming from a CO_2 increase induces a countering increase in the poleward latent heat transport. The CO2 experiment indicates that if the sea ice loss is disregarded, the latent heat transport exceeds the DSE decrease resulting in a larger poleward net heat transport.

7.2 Perspectives and future work

Research projects like the present Ph.D. study often raises more questions than can be answered within the scope of the work. In this section, unanswered questions and ideas for future work are presented. Some ideas have been part of the original project plan but have not been feasible within the final frame of the project, while others are building on the findings throughout the project.

- **Greenland ice sheet reconstruction.** A natural continuation of the surface mass balance calculations (Chapter 4) would be to force an ice sheet model with the fields derived from the GCM. The caveats are that the output fields are in relative coarse resolution and represent only a single time slice during the Eemian. Nonetheless, it would be interesting to assess how the 125 ka conditions could impact the ice sheet, and to compare the simulated ice sheet to the existing reconstructions.
- **Sensitivity to changing ice sheets.** The paleo-model ensemble could be expanded with simulations exploring the sensitivity to changed ice sheet configurations. This could be done using an ice sheet reconstruction based on this simulation, existing reconstructions or by imposing idealized ice sheet changes. The sea level reconstructions suggest considerable ice sheet changes, and as discussed these changes could cause further warming on the ice sheets and affect the atmospheric circulation – and thereby potentially also the ocean circulation.
- **Sensitivity to sea ice loss.** Although important for the simulated Arctic warming, the simulated sea ice cover is still quite extensive (e.g. bigger in extent than current conditions). Whether this is related to a model bias or not, it would be worthwhile to further explore the impact of more drastic sea ice loss; especially

since proxy reconstructions indicate reduced sea ice conditions even in the central Arctic.

- **Assessment of the AMOC response.** The simulated AMOC increase has a big impact on the North Atlantic climate. It would be useful to investigate the impact of the activated Labrador Sea convection, and assess the relative contributions to the AMOC increase – e.g. by separating the overturning and gyre components. Similarly it is important to establish the causality of the changes in the Labrador Sea: is the sea ice retreat activating convection, or is the increased convection driving the sea ice retreat.
- **Eemian melt events on Greenland.** In an earlier state of the project, it was planned to investigate the likelihood of melt events on Greenland based on the simulations. Ice cores show clear melt-layer features during the Eemian (*NEEM community members*, 2013), and the pronounced high-latitude summer warming suggest that melt events could occur. The simulations, however, showed no sign of surface melt on the Greenland ice sheet. Nonetheless, some features of the simulated climate indicate increased potential for GrIS surface melt. The widespread surface melt observed in 2012 has been associated with a so-called atmospheric river event and sequence of contributing factors. These included warm conditions over the North American continent and warm waters south of Greenland (*Neff et al.*, 2014); both of these conditions are present in the simulated mean Eemian summertime climate. Hence, comparison of the simulated Eemian atmospheric circulation to the 2012 conditions might reveal if warm air advection could similarly cause warming over Greenland.
- **Moisture sources.** The precipitation is increased considerably over Greenland, but what is the source of the moisture? Ice core records are sensitive to changes in moisture sources regions, and it would be valuable to identify the moisture origin during the Eemian. A first attempt could be an analysis similar to *Bintanja and Selten* (2014) identifying if the additional moisture originates from the Arctic region or more remote sources.
- **Antarctic warming.** The simulated Antarctic climate only show very limited temperature changes. This could be due to the choice of time-slice (Antarctic peak warming occurred in the earlier part of the Eemian) or the fixed ice sheet topography. Some of the above-mentioned sensitivity studies (sea ice and/or ice sheet configuration) could serve as starting points for assessing the (lack of) Antarctic warming. Alternatively, the "calendar-effect" could be impacting especially the Antarctic changes, as the peak forcing occurs in Austral spring (i.e. furthest from the fixed vernal equinox). However, the calculations by *Joussaume and Braconnot* (1997) show that angular season definitions would reduce the Austral spring forcing over Antarctica, suggesting that the consequent warming response might also be reduced.

7.3 Conclusion

The climate model experiments in this project all indicate that the Arctic sea ice plays an important role in shaping both past, present, and future climate states. As the paleoclimate experiments here indicate, it can be challenging to model the sea ice which is affected by both atmospheric and oceanic conditions. This emphasizes the need for further research in the impacts of sea ice changes that could have a large impact on the future climate.

This analysis revealed that the atmospheric circulation is sensitive to the location of sea ice loss, which can affect the climate both within and beyond the Arctic region. The remote response still requires scientific investigation, but these experiments have shown that responding sea surface temperatures are important for the propagation of the response. This should be taken into account, when designing future model projections of sea ice loss scenarios.

The high-resolution simulations of the last interglacial climate appeared relatively similar to previous paleoclimate simulations, and consequently still deviated from proxy data reconstructions. Part of the deviation is likely due to the model setup, suggesting that traditional paleoclimate modelling setups can not capture all past climate states accurately. As also noted by *Lunt et al.* (2013) (cf. Section 2.1), inclusion of changed ice sheet topography and changed vegetation patterns could potentially reduce to model-data discrepancy. The particular model sensitivity and regional biases is also impacting our results: proxy data reconstructions suggest a larger sea ice response than simulated here. The relatively cold conditions on the Greenland ice sheet are further inhibiting potential feedbacks; e.g. the albedo impact of surface melt.

A long-lasting research question is whether the last interglacial can serve as an analogue for future climate changes. While sea surface warming and sea ice loss dominates the Arctic climate for a large part of the year, these experiments highlight that the insolation is very important for the changes on the Greenland ice sheet. Consequently, the last interglacial temperature-melt relationship may lead to excessive mass loss estimates if applied to future climates.

While inclusion of more active elements (i.e. ice sheet and vegetation models) in paleoclimate studies reduce the model data mismatch, this thesis indicates that the treatment of the Arctic sea ice in the models could substantially impact the simulated response. With increased understanding of the climate mechanisms related to the sea ice, we might improve our understanding of the past climate and projections of the future.

Bibliography

Abbot, D. S., and E. Tziperman, Sea ice, high-latitude convection, and equable climates, *Geophysical Research Letters*, *35*(3), 1–5, doi:10.1029/2007GL032286, 2008.

Abbot, D. S., C. C. Walker, and E. Tziperman, Can a convective cloud feedback help to eliminate winter sea ice at high CO_2 concentrations?, *Journal of Climate*, *22*(21), 5719–5731, doi:10.1175/2009JCLI2854.1, 2009.

Adler, R. E., L. Polyak, J. D. Ortiz, D. S. Kaufman, J. E. T. Channell, C. Xuan, A. G. Grottoli, E. Sellén, and K. A. Crawford, Sediment record from the western Arctic Ocean with an improved Late Quaternary age resolution: HOTRAX core HLY0503-8JPC, Mendeleev Ridge, *Global and Planetary Change*, *68*(1-2), 18–29, doi:10.1016/j.gloplacha.2009.03.026, 2009.

Alexander, M. A., U. S. Bhatt, J. E. Walsh, M. S. Timlin, J. S. Miller, and J. D. Scott, The Atmospheric Response to Realistic Arctic Sea Ice Anomalies in an AGCM during Winter, *Journal of Climate*, *17*, 890–905, 2004.

Alexeev, V. A., P. L. Langen, and J. R. Bates, Polar amplification of surface warming on an aquaplanet in "ghost forcing" experiments without sea ice feedbacks, *Climate Dynamics*, *24*(7-8), 655–666, doi:10.1007/s00382-005-0018-3, 2005.

Arrhenius, S., On the Influence of Carbonic Acid in the Air upon the Temperature of the Ground, *Philosophical Magazine and Journal of Science*, 1896.

Bader, J., M. D. S. Mesquita, K. I. Hodges, N. Keenlyside, S. Østerhus, and M. Miles, A review on Northern Hemisphere sea-ice, storminess and the North Atlantic Oscillation: Observations and projected changes, *Atmospheric Research*, *101*(4), 809–834, doi:10.1016/j.atmosres.2011.04.007, 2011.

Bailey, D., M. Holland, E. Hunke, B. Lipscomb, B. Briegleb, C. Bitz, and J. Schramm, Community Ice CodE (CICE) User's Guide Version 4.0, *Tech. rep.*, National Center for Atmospheric Research, Boulder, CO, USA, 2010.

Bailey, D., C. Hannay, M. M. Holland, and R. Neale, Slab Ocean Model Forcing, 2011.

Bakker, P., and H. Renssen, Last interglacial model-data mismatch of thermal maximum temperatures partially explained, *Climate of the Past*, *10*(4), 1633–1644, doi:10.5194/cp-10-1633-2014, 2014.

Bakker, P., et al., Last interglacial temperature evolution – a model inter-comparison, *Climate of the Past*, *9*(2), 605–619, doi:10.5194/cp-9-605-2013, 2013.

Bakker, P., et al., Temperature trends during the present and last interglacial periods - a multi-model-data comparison, *Quaternary Science Reviews*, *99*, 224–243, doi:10.1016/j.quascirev.2014.06.031, 2014.

Balsamo, G., A. Beljaars, K. Scipal, P. Viterbo, B. van den Hurk, M. Hirschi, and A. K. Betts, A Revised Hydrology for the ECMWF Model: Verification from Field Site to Terrestrial Water Storage and Impact in the Integrated Forecast System, *Journal of Hydrometeorology*, *10*(3), 623–643, doi:10.1175/2008JHM1068.1, 2009.

Barnes, E. A., Revisiting the evidence linking Arctic amplification to extreme weather in midlatitudes, *Geophysical Research Letters*, *40*(17), 4734–4739, doi:10.1002/grl.50880, 2013.

Barton, N. P., S. A. Klein, and J. S. Boyle, On the Contribution of Longwave Radiation to Global Climate Model Biases in Arctic Lower Tropospheric Stability, *Journal of Climate*, *27*(19), 7250–7269, doi:10.1175/JCLI-D-14-00126.1, 2014.

Bauch, H. A., E. S. Kandiano, and J. P. Helmke, Contrasting ocean changes between the subpolar and polar North Atlantic during the past 135 ka, *Geophysical Research Letters*, *39*(11), doi:10.1029/2012GL051800, 2012.

Berger, A., Long-term variations of daily insolation and Quaternary climatic changes, *Journal of the Atmospheric Sciences*, *35*, 2362–2367, 1978.

Betts, A. K., and J. H. Ball, Albedo over the boreal forest, *Journal of Geophysical Research*, *102*(D24), 28,901–28,909, doi:10.1029/96JD03876, 1997.

Bintanja, R., and F. M. Selten, Future increases in Arctic precipitation linked to local evaporation and sea-ice retreat, *Nature*, *509*(7501), 479–482, doi:10.1038/nature13259, 2014.

Bintanja, R., R. G. Graversen, and W. Hazeleger, Arctic winter warming amplified by the thermal inversion and consequent low infrared cooling to space, *Nature Geoscience*, *4*(11), 758–761, doi:10.1038/ngeo1285, 2011.

Bitz, C. M., K. M. Shell, P. R. Gent, D. A. Bailey, G. Danabasoglu, K. C. Armour, M. M. Holland, and J. T. Kiehl, Climate sensitivity of the Community Climate System Model, version 4, *Journal of Climate*, *25*(9), 3053–3070, doi:10.1175/JCLI-D-11-00290.1, 2012.

Blaschek, M., P. Bakker, and H. Renssen, The influence of Greenland ice sheet melting on the Atlantic meridional overturning circulation during past and future warm periods: a model study, *Climate Dynamics*, pp. 2137–2157, doi:10.1007/s00382-014-2279-1, 2014.

Blüthgen, J., R. Gerdes, and M. Werner, Atmospheric response to the extreme Arctic sea ice conditions in 2007, *Geophysical Research Letters*, *39*(2), doi:10.1029/2011GL050486, 2012.

Boé, J., A. Hall, and X. Qu, Current GCMs' Unrealistic Negative Feedback in the Arctic, *Journal of Climate*, *22*(17), 4682–4695, doi:10.1175/2009JCLI2885.1, 2009.

Bonan, G. B., D. Pollard, and S. L. Thompson, Effects of Boreal Forest Vegetation on Global Climate, *Nature*, *359*(6397), 716–718, doi:Doi10.1038/359716a0, 1992.

Born, A., and K. H. Nisancioglu, Melting of Northern Greenland during the last interglaciation, *The Cryosphere*, *6*(6), 1239–1250, doi:10.5194/tc-6-1239-2012, 2012.

Born, A., K. H. Nisancioglu, and P. Braconnot, Sea ice induced changes in ocean circulation during the Eemian, *Climate Dynamics*, *35*(7-8), 1361–1371, doi:10.1007/s00382-009-0709-2, 2010.

Bosmans, J. H. C., S. S. Drijfhout, E. Tuenter, F. J. Hilgen, and L. J. Lourens, Response of the North African summer monsoon to precession and obliquity forcings in the EC-Earth GCM, *Climate Dynamics*, *44*(1-2), 279–297, doi:10.1007/s00382-014-2260-z, 2015.

Boucher, O., et al., Clouds and aerolsols, in *Climate Change 2013: The Physical Science Basis. Contribution of Working Group I to the Fifth Assessment Report of the Intergovernmental Panel on Climate Change*, edited by T. F. Stocker, D. Qin, G.-K. Plattner, M. Tignor, S. K. Allen, J. Boschung, A. Nauels, Y. Xia, V. Bex, and P. M. Midgley, chap. 7, pp. 571–657, Cambridge University Press, Cambridge, United Kingdom and New York, NY, USA, 2013.

Box, J. E., X. Fettweis, J. C. Stroeve, M. Tedesco, D. K. Hall, and K. Steffen, Greenland ice sheet albedo feedback: Thermodynamics and atmospheric drivers, *Cryosphere*, *6*(4), 821–839, doi:10.5194/tc-6-821-2012, 2012.

Braconnot, P., C. Marzin, L. Gregoire, E. Mosquet, and O. Marti, Monsoon response to changes in Earth's orbital parameters: Comparisons between simulations of the Eemian and of the Holocene, *Climate of the Past*, *4*, 281–294, 2008.

Braconnot, P., S. P. Harrison, B. Otto-Bliesner, A. Abe-Ouchi, J. Jungclaus, and J.-Y. Peterschmitt, The Paleoclimate Modeling Intercomparison Project contribution to CMIP5, *CLIVAR Exchanges*, *16*(56), 15–19, 2011.

Braconnot, P., S. P. Harrison, M. Kageyama, P. J. Bartlein, V. Masson-Delmotte, A. Abe-Ouchi, B. L. Otto-Bliesner, and Y. Zhao, Evaluation of climate models using palaeoclimatic data, *Nature Climate Change*, *2*(6), 417–424, doi:10.1038/nclimate1456, 2012.

Braconnot, P., et al., Results of PMIP2 coupled simulations of the Mid-Holocene and Last Glacial Maximum - Part 1: experiments and large-scale features, *Climate of the Past*, *3*(2), 261–277, doi:10.5194/cp-3-261-2007, 2007.

Budikova, D., Role of Arctic sea ice in global atmospheric circulation: A review, *Global and Planetary Change*, *68*(3), 149–163, doi:10.1016/j.gloplacha.2009.04.001, 2009.

Caldeira, K., and I. Cvijanovic, Estimating the Contribution of Sea Ice Response to Climate Sensitivity in a Climate Model, *Journal of Climate*, *27*(22), 8597–8607, doi:10.1175/JCLI-D-14-00042.1, 2014.

CAPE-Last Interglacial Project Members, Last Interglacial Arctic warmth confirms polar amplification of climate change, *Quaternary Science Reviews*, *25*(13-14), 1383–1400, doi:10.1016/j.quascirev.2006.01.033, 2006.

Capron, E., et al., Temporal and spatial structure of multi-millennial temperature changes at high latitudes during the Last Interglacial, *Quaternary Science Reviews*, *103*, 116–133, doi:10.1016/j.quascirev.2014.08.018, 2014.

Chen, Q. S., D. H. Bromwich, and L. Bai, Precipitation over Greenland retrieved by a dynamic method and its relation to cyclonic activity, *Journal of Climate*, *10*(5), 839–870, doi:10.1175/1520-0442(1997)010<0839:POGRBA>2.0.CO;2, 1997.

Chiang, J. C. H., and C. M. Bitz, Influence of high latitude ice cover on the marine Intertropical Convergence Zone, *Climate Dynamics*, *25*(5), 477–496, doi:10.1007/s00382-005-0040-5, 2005.

Chiang, J. C. H., W. Cheng, and C. M. Bitz, Fast teleconnections to the tropical Atlantic sector from Atlantic thermohaline adjustment, *Geophysical Research Letters*, *35*(7), doi:10.1029/2008GL033292, 2008.

Chung, C. E., and P. Räisänen, Origin of the Arctic warming in climate models, *Geophysical Research Letters*, *38*(21), doi:10.1029/2011GL049816, 2011.

CLIMAP Project Members, The last interglacial ocean, *Quaternary Research*, *21*(2), 123–224, doi:10.1016/0033-5894(84)90098-X, 1984.

Cohen, J., J. Jones, J. C. Furtado, and E. Tziperman, Warm Arctic, cold continents: A common pattern related to Arctic sea ice melt, snow advance, and extreme winter weather, *Oceanography*, *26*, 150–160, 2013.

Collins, W. D., et al., Description of the NCAR Community Atmosphere Model (CAM 3.0), *Tech. Rep. June*, NCAR, Boulder, Colorado USA, 2004.

Colville, E. J., A. E. Carlson, B. L. Beard, R. G. Hatfield, J. S. Stoner, A. V. Reyes, and D. J. Ullman, Sr-Nd-Pb Isotope Evidence for Ice-Sheet Presence on Southern Greenland During the Last Interglacial, *Science*, *333*(6042), 620–623, doi:10.1126/science.1204673, 2011.

Coumou, D., V. Petoukhov, S. Rahmstorf, S. Petri, and H. J. Schellnhuber, Quasi-resonant circulation regimes and hemispheric synchronization of extreme weather in boreal summer, *Proceedings of the National Academy of Sciences*, *111*(34), 12,331–12,336, doi:10.1073/pnas.1412797111, 2014.

Crucifix, M., and M.-F. Loutre, Transient simulations over the last interglacial period (126-115 kyr BP): feedback and forcing analysis, *Climate Dynamics*, *19*(5-6), 417–433, doi:10.1007/s00382-002-0234-z, 2002.

Crucifix, M., M.-F. Loutre, and A. Berger, The Climate Response to the Astronomical Forcing, *Space Science Reviews*, *125*(1-4), 213–226, doi:10.1007/s11214-006-9058-1, 2007.

Cubasch, U., E. Zorita, F. Kaspar, J. F. Gonzalez-Rouco, H. V. Storch, and K. Prömmel, Simulation of the role of solar and orbital forcing on climate, *Advances in Space Research*, *37*(8), 1629–1634, doi:10.1016/j.asr.2005.04.076, 2006.

Cuffey, K. M., and S. J. Marshall, Substantial contribution to sea-level rise during the last interglacial from the Greenland ice sheet, *Nature*, *404*(6778), 591–4, doi:10.1038/35007053, 2000.

Cunningham, S. A., et al., Temporal Variability of the Atlantic Meridional Overturning Circulation at 26.5°N, *Science*, *317*(August), 935–938, 2007.

Cvijanovic, I., and K. Caldeira, Atmospheric impacts of sea ice decline in CO2 induced global warming, *Climate Dynamics*, *44*(5-6), 1173–1186, doi:10.1007/s00382-015-2489-1, 2015.

Cvijanovic, I., and J. C. H. Chiang, Global energy budget changes to high latitude North Atlantic cooling and the tropical ITCZ response, *Climate Dynamics*, *40*(5-6), 1435–1452, doi:10.1007/s00382-012-1482-1, 2013.

Danabasoglu, G., and P. R. Gent, Equilibrium Climate Sensitivity: Is It Accurate to Use a Slab Ocean Model?, *Journal of Climate*, *22*(9), 2494–2499, doi:10.1175/2008JCLI2596.1, 2009.

Dansgaard, W., H. B. Clausen, N. Gundestrup, C. U. Hammer, S. J. Johnsen, M. Kristinsdottir, and N. Reeh, A New Greenland Deep Ice Core, *Science*, *218*(4579), 1273–1277, 1982.

Davini, P., U. Fladrich, L. Filippi, J. von Hardenberg, and R. Döscher, *EC-Earth 3.1 Extended Release Notes*, 19 pp., 2014.

Davini, P., J. von Hardenberg, L. Filippi, and A. Provenzale, Impact of Greenland orography on the Atlantic Meridional Overturning Circulation, *Geophysical Research Letters*, *42*(3), 871–879, doi:10.1002/2014GL062668, 2015.

de Noblet, N., P. Braconnot, S. Joussaume, and V. Masson, Sensitivity of simulated Asian and African summer monsoons to orbitally induced variations in insolation 126, 115 and 6 kBP, *Climate Dynamics*, *12*, 589–603, doi:10.1007/s003820050130, 1996.

Deser, C., On the teleconnectivity of the "Arctic Oscillation", *Geophysical Research Letters*, *27*(6), 779–782, doi:10.1029/1999GL010945, 2000.

Deser, C., G. Magnusdottir, R. Saravanan, and A. Phillips, The Effects of North Atlantic SST and Sea Ice Anomalies on the Winter Circulation in CCM3. Part II: Direct and Indirect Components of the Response, *Journal of Climate*, *17*(5), 877–889, 2004.

Deser, C., R. Tomas, M. A. Alexander, and D. Lawrence, The Seasonal Atmospheric Response to Projected Arctic Sea Ice Loss in the Late Twenty-First Century, *Journal of Climate*, *23*(2), 333–351, doi:10.1175/2009JCLI3053.1, 2010.

Deser, C., R. A. Tomas, and L. Sun, The Role of Ocean–Atmosphere Coupling in the Zonal-Mean Atmospheric Response to Arctic Sea Ice Loss, *Journal of Climate*, *28*(6), 2168–2186, doi:10.1175/JCLI-D-14-00325.1, 2015.

Deser, C., L. Sun, R. A. Tomas, and J. Screen, Does ocean-coupling matter for the northern extra-tropical response to projected Arctic sea ice loss?, *Geophysical Research Letters*, pp. 2149–2157, doi:10.1002/2016GL067792, 2016.

Dong, B., R. T. Sutton, and T. Woollings, Changes of interannual NAO variability in response to greenhouse gases forcing, *Climate Dynamics*, *37*, 1621–1641, doi:10.1007/s00382-010-0936-6, 2011.

Dutton, A., and K. Lambeck, Ice volume and sea level during the last interglacial., *Science*, *337*(6091), 216–219, doi:10.1126/science.1205749, 2012.

Dutton, A., A. E. Carlson, A. J. Long, G. A. Milne, P. U. Clark, R. DeConto, B. P. Horton, S. Rahmstorf, and M. E. Raymo, Sea-level rise due to polar ice-sheet mass loss during past warm periods, *Science*, *349*(6244), doi:10.1126/science.aaa4019, 2015.

Edwards, M., T. Hamilton, S. Elias, N. Bigelow, and A. Krumhardt, Interglacial Extension of the Boreal Forest Limit in the Noatak Valley, Northwest Alaska: Evidence from an Exhumed River-Cut Bluff and Debris Apron, *Arctic, Antarctic, and Alpine Research*, *35*(4), 460–468, doi:10.1657/1523-0430(2003)035[0460:IEOTBF]2.0.CO;2, 2003.

Efron, B., and G. Gong, A leisurely look at the bootstrap, the jackknife, and cross-validation, *The American Statistician*, *37*(1), 36–48, doi:10.2307/2685844, 1983.

European Centre for Medium-Range Weather Forecasts, CY36R1 Official IFS Documentation, `https://software.ecmwf.int/wiki/display/IFS/CY36R1+Official+IFS+Documentation`, accessed: 2016-03-09, 2010.

Fischer, N., and J. H. Jungclaus, Effects of orbital forcing on atmosphere and ocean heat transports in Holocene and Eemian climate simulations with a comprehensive Earth system model, *Climate of the Past*, *6*(2), 155–168, doi:10.5194/cp-6-155-2010, 2010.

Flato, G., et al., Evaluation of Climate Models, in *Climate Change 2013: The Physical Science Basis. Contribution of Working Group I to the Fifth Assessment Report of the Intergovernmental Panel on Climate Change*, edited by T. F. Stocker, D. Qin, G.-K. Plattner, M. Tignor, S. K. Allen, J. Boschung, A. Nauels, Y. Xia, V. Bex, and P. M. Midgley, pp. 741–866, Cambridge University Press, doi:10.1017/CBO9781107415324.020, 2013.

Francis, J. A., and E. Hunter, Changes in the fabric of the Arctic's greenhouse blanket, *Environmental Research Letters*, *2*(4), 045,011, doi:10.1088/1748-9326/2/4/045011, 2007.

Francis, J. A., and S. J. Vavrus, Evidence linking Arctic amplification to extreme weather in mid-latitudes, *Geophysical Research Letters*, *39*(6), doi:10.1029/2012GL051000, 2012.

Francis, J. A., and S. J. Vavrus, Evidence for a wavier jet stream in response to rapid Arctic warming, *Environmental Research Letters*, *10*(1), 014,005, doi:10.1088/1748-9326/10/1/014005, 2015.

Ganopolski, A., and S. Rahmstorf, Rapid changes of glacial climate simulated in a coupled climate model, *Nature*, *409*, 153–158, 2001.

Gent, P. R., et al., The Community Climate System Model Version 4, *Journal of Climate*, *24*(19), 4973–4991, doi:10.1175/2011JCLI4083.1, 2011.

Gerdes, R., Atmospheric response to changes in Arctic sea ice thickness, *Geophysical Research Letters*, *33*(18), doi:10.1029/2006GL027146, 2006.

Gingele, F. X., P. M. Müller, and R. R. Schneider, Orbital forcing of freshwater input in the Zaire Fan area - Clay mineral evidence from the last 200 kyr, *Palaeogeography, Palaeoclimatology, Palaeoecology*, *138*(1-4), 17–26, doi:10.1016/S0031-0182(97)00121-1, 1998.

Govin, A., V. Varma, and M. Prange, Astronomically forced variations in western African rainfall (20N-20S) during the Last Interglacial Period, *Geophysical Research Letters*, pp. 799–804, doi:10.1002/2013GL058954, 2014.

Govin, A., et al., Persistent influence of ice sheet melting on high northern latitude climate during the early Last Interglacial, *Climate of the Past*, *8*(2), 483–507, doi:10.5194/cp-8-483-2012, 2012.

Govin, A., et al., Sequence of events from the onset to the demise of the Last Interglacial: Evaluating strengths and limitations of chronologies used in climatic archives, *Quaternary Science Reviews*, *129*, 1–36, doi:10.1016/j.quascirev.2015.09.018, 2015.

Graversen, R. G., and M. Burtu, Arctic amplification enhanced by latent energy transport of atmospheric planetary waves, *Quarterly Journal of the Royal Meteorological Society*, *In Press*, 2016.

Graversen, R. G., and M. Wang, Polar amplification in a coupled climate model with locked albedo, *Climate Dynamics*, *33*(5), 629–643, doi:10.1007/s00382-009-0535-6, 2009.

Graversen, R. G., T. Mauritsen, M. Tjernström, E. Källén, and G. Svensson, Vertical structure of recent Arctic warming., *Nature*, *451*(7174), 53–56, doi:10.1038/nature06502, 2008.

Greeves, C. Z., V. D. Pope, R. A. Stratton, and G. M. Martin, Representation of Northern Hemisphere winter storm tracks in climate models, *Climate Dynamics*, *28*, 683–702, doi:10.1007/s00382-006-0205-x, 2007.

GRIP members, Climate instability during the last interglacial period recorded in the GRIP ice core, *Nature*, *364*, 203–207, 1993.

Gröger, M., E. Maier-Reimer, U. Mikolajewicz, G. Schurgers, M. Vizcaíno, and A. M. E. Winguth, Changes in the hydrological cycle, ocean circulation, and carbon/nutrient cycling during the last interglacial and glacial transition, *Paleoceanography*, *22*(4), doi:10.1029/2006PA001375, 2007.

Grootes, P. M., M. Stuiver, J. W. C. White, S. J. Johnsen, and J. Jouzel, Comparison of oxygen isotope records from the GISP2 and GRIP Greenland ice cores, *Nature*, *366*(6455), 552–554, doi:10.1038/366552a0, 1993.

Hakuba, M. Z., D. Folini, M. Wild, and C. Schär, Impact of Greenland's topographic height on precipitation and snow accumulation in idealized simulations, *Journal of Geophysical Research Atmospheres*, *117*(9), 1–15, doi:10.1029/2011JD017052, 2012.

Hall, A., The Role of Surface Albedo Feedback in Climate, *Journal of Climate*, *17*(7), 1550–1568, 2004.

Hansen, J., and L. Nazarenko, Soot climate forcing via snow and ice albedos, *Proceedings of the National Academy of Sciences of the United States of America*, *101*(2), 423–428, 2004.

Harrison, S. P., J. E. Kutzbach, I. C. Prentice, P. J. Behling, and M. T. Sykes, The response of northern hemisphere extratropical climate and vegetation to orbitally in-

duced changes in insolation during the last interglaciation, *Quaternary Research*, *43*, 174–184, 1995.

Hays, J. D., J. Imbrie, and N. J. Shackleton, Variations in the Earth's Orbit: Pacemaker of the Ice Ages, *Science*, *194*(4270), 1121–1132, 1976.

Hazeleger, W., et al., EC-Earth: A Seamless Earth-System Prediction Approach in Action, *Bulletin of the American Meteorological Society*, *91*(10), 1357–1363, doi:10.1175/2010BAMS2877.1, 2010.

Hazeleger, W., et al., EC-Earth V2.2: description and validation of a new seamless earth system prediction model, *Climate Dynamics*, *39*(11), 2611–2629, doi:10.1007/s00382-011-1228-5, 2012.

Helsen, M. M., W. J. van de Berg, R. S. W. van de Wal, M. R. van den Broeke, and J. Oerlemans, Coupled regional climate–ice-sheet simulation shows limited Greenland ice loss during the Eemian, *Climate of the Past*, *9*(4), 1773–1788, doi:10.5194/cp-9-1773-2013, 2013.

Herold, N., Q. Z. Yin, M. P. Karami, and A. Berger, Modelling the climatic diversity of the warm interglacials, *Quaternary Science Reviews*, *56*, 126–141, doi:10.1016/j.quascirev.2012.08.020, 2012.

Hillaire-Marcel, C., A. de Vernal, G. Bilodeau, and A. J. Weaver, Absence of deep-water formation in the Labrador Sea during the last interglacial period., *Nature*, *410*(6832), 1073–7, doi:10.1038/35074059, 2001.

Hilmer, M., and T. Jung, Evidence for a recent change in the link between the North Atlantic Oscillation and Arctic sea ice export, *Geophysical Research Letters*, *27*(7), 989–992, 2000.

Holden, P. B., N. R. Edwards, E. W. Wolff, N. J. Lang, J. S. Singarayer, P. J. Valdes, and T. F. Stocker, Interhemispheric coupling, the West Antarctic Ice Sheet and warm Antarctic interglacials, *Climate of the Past*, *6*(4), 431–443, doi:10.5194/cp-6-431-2010, 2010.

Holland, M. M., and C. M. Bitz, Polar amplification of climate change in coupled models, *Climate Dynamics*, *21*(3-4), 221–232, doi:10.1007/s00382-003-0332-6, 2003.

Holland, M. M., M. C. Serreze, and J. Stroeve, The sea ice mass budget of the Arctic and its future change as simulated by coupled climate models, *Climate Dynamics*, *34*(2), 185–200, doi:10.1007/s00382-008-0493-4, 2010.

Holton, J. R., and G. J. Hakim, *An introduction to Dynamic Meteorology*, fifth edit ed., 532 pp., Elsevier Inc., 2013.

Hu, Z. Z., and Z. Wu, The intensification and shift of the annual North Atlantic Oscillation in a global warming scenario simulation, *Tellus, Series A: Dynamic Meteorology and Oceanography*, *56*, 112–124, doi:10.1111/j.1600-0870.2004.00050.x, 2004.

Hunke, E. C., and W. H. Lipscomb, CICE: The Los Alamos Sea Ice Model. Documentation and Software User's Manual. Version 4.0, *Tech. rep.*, T-3 Fluid Dynamics Group, Los Alamos National Laboratory, Tech. Rep. LA-CC-06-012, 2008.

Hurrell, J. W., Decadal trends in the North Atlantic Oscillation NAO: Regional temperatures and precipitation, *Science*, *269*, 676–679, 1995.

Hurrell, J. W., and C. Deser, North Atlantic climate variability: The role of the North Atlantic Oscillation, *Journal of Marine Systems*, *79*(3-4), 231–244, doi:10.1016/j.jmarsys.2009.11.002, 2010.

Hurrell, J. W., and National Center for Atmospheric Research Staff (Eds.), The Climate Data Guide: Hurrell North Atlantic Oscillation (NAO) Index (PC-based), 2015.

Hurrell, J. W., J. J. Hack, B. A. Boville, D. L. Williamson, and J. T. Kiehl, The Dynamical Simulation of the NCAR Community Climate Model Version 3 (CCM3), *Journal of Climate*, *11*(6), 1207–1236, doi:10.1175/1520-0442(1998)011<1207:TDSOTN>2.0.CO;2, 1998.

Hurrell, J. W., Y. Kushnir, G. Ottersen, and M. Visbeck, An Overview of the North Atlantic Oscillation, in *The North Atlantic Oscillation: Climatic Significance and Environmental Impact*, edited by J. W. Hurrell, Y. Kushnir, G. Ottersen, and M. Visbeck, doi:doi:10.1029/134GM01, 2003.

Huybers, P., Early Pleistocene Glacial Cycles and the Integrated Summer Insolation Forcing, *Science*, *313*, 508–511, 2006.

Huybers, P., and C. Wunsch, Obliquity pacing of the late Pleistocene glacial terminations, *Nature*, *434*, 491–494, doi:10.1038/nature03349.1.2.3.4.5.6.Luiten, 2005.

Imbrie, J., et al., On the structure and origin of major glaciation cycles. 2. The 100,000-year cycle, *Paleoceanography*, *8*(6), 699–735, 1993.

Jaiser, R., K. Dethloff, D. Handorf, A. Rinke, and J. Cohen, Impact of sea ice cover changes on the Northern Hemisphere atmospheric winter circulation, *Tellus A*, *64*, 1–11, doi:10.3402/tellusa.v64i0.11595, 2012.

Johnsen, S. J., H. B. Clausen, W. Dansgaard, N. S. Gundestrup, M. Hansson, P. Jonsson, J. P. Steffensen, and A. E. Sveinbjörnsdottir, A "deep" ice core from East Greenland, *Meddelser om Grønland, Geoscience*, *29*, 3–22, 1992.

Johnsen, S. J., D. Dahl-Jensen, N. Gundestrup, J. P. Steffensen, H. B. Clausen, H. Miller, V. Masson-Delmotte, A. E. Sveinbjörnsdottir, and J. W. C. White, Oxygen isotope and palaeotemperature records from six Greenland ice-core stations: Camp Century, Dye-3, GRIP, GISP2, Renland and NorthGRIP, *Journal of Quaternary Science*, *16*(4), 299–307, doi:10.1002/jqs.622, 2001.

Joussaume, S., and P. Braconnot, Sensitivity of paleoclimate simulation results to season definitions, *Journal of Geophysical Research*, *102*, 1943–1956, 1997.

Jouzel, J., et al., Validity of the temperature reconstruction from water isotopes in ice cores, *Journal of Geophysical Research*, *102*(C12), 26,471–26,487, doi:10.1029/97JC01283, 1997.

Jouzel, J., et al., Orbital and millennial Antarctic climate variability over the past 800,000 years., *Science*, *317*(5839), 793–796, doi:10.1126/science.1141038, 2007.

Jung, T., M. Hilmer, E. Ruprecht, S. Kleppek, S. K. Gulev, and O. Zolina, Characteristics of the recent eastward shift of interannual NAO variability, *Journal of Cli-*

mate, *16*(20), 3371–3382, doi:10.1175/1520-0442(2003)016<3371:COTRES>2.0.CO;2, 2003.

Kaspar, F., T. Spangehl, and U. Cubasch, Northern hemisphere winter storm tracks of the Eemian interglacial and the last glacial inception, *Climate of the Past*, *3*(2), 181–192, doi:10.5194/cp-3-181-2007, 2007.

Kay, J. E., M. M. Holland, C. M. Bitz, E. Blanchard-Wrigglesworth, A. Gettelman, A. Conley, and D. A. Bailey, The Influence of Local Feedbacks and Northward Heat Transport on the Equilibrium Arctic Climate Response to Increased Greenhouse Gas Forcing, *Journal of Climate*, *25*(16), 5433–5450, doi:10.1175/JCLI-D-11-00622.1, 2012.

Khodri, M., G. Ramstein, D. Paillard, J. C. Duplessy, and M. Kageyama, Modelling the climate evolution from the last interglacial to the start of the last glaciation: The role of Arctic Ocean freshwater budget, *Geophysical Research Letters*, *30*(12), doi:10.1029/2003GL017108, 2003.

Kim, S.-J., J. M. Lü, S. Yi, T. Choi, B.-M. Kim, B. Y. Lee, S.-H. Woo, and Y. Kim, Climate response over Asia/Arctic to change in orbital parameters for the last interglacial maximum, *Geosciences Journal*, *14*(2), 173–190, doi:10.1007/s12303-010-0017-1, 2010.

Kopp, R. E., F. J. Simons, J. X. Mitrovica, A. C. Maloof, and M. Oppenheimer, Probabilistic assessment of sea level during the last interglacial stage., *Nature*, *462*(7275), 863–7, doi:10.1038/nature08686, 2009.

Kopp, R. E., F. J. Simons, J. X. Mitrovica, A. C. Maloof, and M. Oppenheimer, A probabilistic assessment of sea level variations within the last interglacial stage, *Geophysical Journal International*, *193*(2), 711–716, doi:10.1093/gji/ggt029, 2013.

Kuhlbrodt, T., A. Griesel, M. Montoya, A. Levermann, M. Hofmann, and S. Rahmstorf, On the driving processes of the Atlantic meridional overturning circulation, *Reviews of Geophysics*, *45*(RG2001), doi:10.1029/2004RG000166, 2007.

Kumar, A., J. Perlwitz, J. Eischeid, X. Quan, T. Xu, T. Zhang, M. Hoerling, B. Jha, and W. Wang, Contribution of sea ice loss to arctic amplification, *Geophysical Research Letters*, *37*(21), doi:10.1029/2010GL045022, 2010.

Kutzbach, J. E., Large-Scale Features of Monthly Mean Northern Hemisphere Anomaly Maps of Sea-Level Pressure, *Monthly Weather Review*, *98*(9), 708–716, doi:10.1175/1520-0493(1970)098<0708:LSFOMM>2.3.CO;2, 1970.

Kvamstø, N. G., P. Skeie, and D. B. Stephenson, Impact of Labrador sea-ice extent on the North Atlantic Oscillation, *International Journal of Climatology*, *24*(5), 603–612, doi:10.1002/joc.1015, 2004.

Kwok, R., and D. A. Rothrock, Decline in Arctic sea ice thickness from submarine and ICESat records: 1958–2008, *Geophysical Research Letters*, *36*(15), doi:10.1029/2009GL039035, 2009.

Landais, A., et al., How warm was Greenland during the last interglacial period?, *Climate of the Past Discussions*, doi:10.5194/cp-2016-28, 2016.

Langebroek, P. M., and K. H. Nisancioglu, Simulating last interglacial climate with NorESM: Role of insolation and greenhouse gases in the timing of peak warmth, *Climate of the Past*, *10*(4), 1305–1318, doi:10.5194/cp-10-1305-2014, 2014.

Langen, P. L., et al., Quantifying Energy and Mass Fluxes Controlling Godthåbsfjord Freshwater Input in a 5-km Simulation (1991–2012), *Journal of Climate*, *28*(9), 3694–3713, doi:10.1175/JCLI-D-14-00271.1, 2015.

Lawrence, D. M., et al., Parameterization improvements and functional and structural advances in Version 4 of the Community Land Model, *Journal of Advances in Modeling Earth Systems*, *3*(3), M03,001, doi:10.1029/2011MS000045, 2011.

Lefebre, F., H. Gallée, J.-P. van Ypersele, and W. Greuell, Modeling of snow and ice melt at ETH Camp (West Greenland): A study of surface albedo, *Journal of Geophysical Research*, *108*(D8, 4231), doi:10.1029/2001JD001160, 2003.

Lhomme, N., G. K. Clarke, and S. J. Marshall, Tracer transport in the Greenland Ice Sheet: constraints on ice cores and glacial history, *Quaternary Science Reviews*, *24*(1-2), 173–194, doi:10.1016/j.quascirev.2004.08.020, 2005.

Li, C., and D. S. Battisti, Reduced Atlantic Storminess during Last Glacial Maximum: Evidence from a Coupled Climate Model, *Journal of Climate*, *21*(14), 3561–3579, doi:10.1175/2007JCLI2166.1, 2008.

Lisiecki, L. E., Links between eccentricity forcing and the 100,000-year glacial cycle, *Nature Geoscience*, *3*(5), 349–352, doi:10.1038/ngeo828, 2010.

Liu, J., J. A. Curry, H. Wang, M. Song, and R. M. Horton, Impact of declining Arctic sea ice on winter snowfall, *Proceedings of the National Academy of Sciences*, *109*(11), 4074–4079, doi:10.1073/pnas.1114910109, 2012.

Liu, Z., S. P. Harrison, J. Kutzbach, and B. Otto-Bliesner, Global monsoons in the mid-Holocene and oceanic feedback, *Climate Dynamics*, *22*(2-3), 157–182, doi:10.1007/s00382-003-0372-y, 2004.

Loutre, M.-F., T. Fichefet, H. Goosse, P. Huybrechts, H. Goelzer, and E. Capron, Factors controlling the last interglacial climate as simulated by LOVECLIM1.3, *Climate of the Past*, *10*, 235–290, doi:10.5194/cp-10-1541-2014, 2014.

Lozhkin, A. V., and P. M. Anderson, The Last Interglaciation in Northeast Sibera, doi:10.1006/qres.1995.1016, 1995.

Lunt, D. J., N. de Noblet-Ducoudré, and S. Charbit, Effects of a melted Greenland ice sheet on climate, vegetation, and the cryosphere, *Climate Dynamics*, *23*(7-8), 679–694, doi:10.1007/s00382-004-0463-4, 2004.

Lunt, D. J., et al., A multi-model assessment of last interglacial temperatures, *Climate of the Past*, *9*(2), 699–717, doi:10.5194/cp-9-699-2013, 2013.

Madec, G., NEMO Ocean Engine (version 3.3). Note du Pôle de modélisation de l'Institut Pierre-Simon Laplace No 27. ISSN No 1288-1619., 2011.

Magnusdottir, G., C. Deser, and R. Saravanan, The effects of North Atlantic SST and sea ice anomalies on the winter circulation in CCM3. Part I: Main features and storm track characteristics of the response, *Journal of Climate*, *17*(5), 857–876, 2004.

Maslanik, J. A., C. Fowler, J. C. Stroeve, S. Drobot, J. Zwally, D. Yi, and W. Emery, A younger, thinner Arctic ice cover: Increased potential for rapid, extensive sea-ice loss, *Geophysical Research Letters*, *34*(24), doi:10.1029/2007GL032043, 2007.

Masson-Delmotte, V., et al., Past and future polar amplification of climate change: climate model intercomparisons and ice-core constraints, *Climate Dynamics*, *26*(5), 513–529, doi:10.1007/s00382-005-0081-9, 2006.

Masson-Delmotte, V., et al., Sensitivity of interglacial Greenland temperature and δ18O: ice core data, orbital and increased CO2 climate simulations, *Climate of the Past*, *7*(3), 1041–1059, doi:10.5194/cp-7-1041-2011, 2011.

Masson-Delmotte, V., et al., Information from Paleoclimate Archives, in *Climate Change 2013: The Physical Science Basis. Contribution of Working Group I to the Fifth Assessment Report of the Intergovernmental Panel on Climate Change*, edited by T. F. Stocker, D. Qin, G.-K. Plattner, M. Tignor, S. K. Allen, J. Boschung, A. Nauels, Y. Xia, V. Bex, and P. M. Midgley, pp. 383–464, Cambridge University Press, doi: 10.1017/CBO9781107415324.013, 2013.

Mauritsen, T., et al., Tuning the climate of a global model, *Journal of Advances in Modeling Earth Systems*, *4*, 1–18, doi:10.1029/2012MS000154, 2012.

McKay, N. P., J. T. Overpeck, and B. L. Otto-Bliesner, The role of ocean thermal expansion in Last Interglacial sea level rise, *Geophysical Research Letters*, *38*(14), doi:10.1029/2011GL048280, 2011.

Meier, W., F. Fetterer, M. Savoie, S. Mallory, R. Duerr, and J. C. Stroeve, NOAA/NSIDC Climate Data Record of Passive Microwave Sea Ice Concentration, Version 2. Boulder, Colorado, USA: National Snow and Ice Data Center, doi: 10.7265/N55M63M1, 2013.

Mercer, J. H., West Antarctic ice sheet and CO2 greenhouse effect: a threat of disaster, *Nature*, *271*(5643), 321–325, doi:10.1038/271321a0, 1978.

Merz, N., A. Born, C. C. Raible, H. Fischer, and T. F. Stocker, Dependence of Eemian Greenland temperature reconstructions on the ice sheet topography, *Climate of the Past*, *10*(3), 1221–1238, doi:10.5194/cp-10-1221-2014, 2014a.

Merz, N., G. Gfeller, A. Born, C. C. Raible, T. F. Stocker, and H. Fischer, Influence of ice sheet topography on Greenland precipitation during the Eemian interglacial, *Journal of Geophysical Research: Atmospheres*, *119*, 10,749–10,768, doi: 10.1002/2014JD021940.Received, 2014b.

Merz, N., A. Born, C. C. Raible, and T. F. Stocker, Warm Greenland during the last interglacial: the role of regional changes in sea ice cover, *Climate of the Past Discussions*, (February), 1–37, doi:10.5194/cp-2016-12, 2016.

Miller, G. H., R. B. Alley, J. Brigham-Grette, J. J. Fitzpatrick, L. Polyak, M. C. Serreze, and J. W. C. White, Arctic amplification: can the past constrain the future?, *Quaternary Science Reviews*, *29*(15-16), 1779–1790, doi:10.1016/j.quascirev.2010.02.008, 2010.

Mitchell, T. D., and P. D. Jones, An improved method of constructing a database of monthly climate observations and associated high-resolution grids, *International Journal of Climatology*, *25*(6), 693–712, doi:10.1002/joc.1181, 2005.

Montoya, M., H. von Storch, and T. J. Crowley, Climate Simulation for 125 kyr BP with a Coupled Ocean–Atmosphere General Circulation Model, *Journal of Climate*, *13*(6), 1057–1072, doi:10.1175/1520-0442(2000)013<1057:CSFKBW>2.0.CO;2, 2000.

Mori, M., M. Watanabe, H. Shiogama, J. Inoue, and M. Kimoto, Robust Arctic sea-ice influence on the frequent Eurasian cold winters in past decades, *Nature Geoscience*, (October), 1–5, doi:10.1038/ngeo2277, 2014.

Muschitiello, F., Q. Zhang, H. S. Sundqvist, F. J. Davies, and H. Renssen, Arctic climate response to the termination of the African Humid Period, *Quaternary Science Reviews*, *125*, 91–97, doi:10.1016/j.quascirev.2015.08.012, 2015.

Neale, R. B., J. Richter, S. Park, P. H. Lauritzen, S. J. Vavrus, P. J. Rasch, and M. Zhang, The Mean Climate of the Community Atmosphere Model (CAM4) in Forced SST and Fully Coupled Experiments, *Journal of Climate*, *26*(14), 5150–5168, doi:10.1175/JCLI-D-12-00236.1, 2013.

Neale, R. B., et al., Description of the NCAR Community Atmosphere Model (CAM 4.0), 2010.

NEEM community members, Eemian interglacial reconstructed from a Greenland folded ice core, *Nature*, *493*(7433), 489–94, doi:10.1038/nature11789, 2013.

Neff, W., G. P. Compo, F. Martin Ralph, and M. D. Shupe, Continental heat anomalies and the extreme melting of the Greenland ice surface in 2012 and 1889, *Journal of Geophysical Research: Atmospheres*, *119*(11), 6520–6536, doi:10.1002/2014JD021470, 2014.

New, M., M. Hulme, and P. Jones, Representing Twentieth-Century Space – Time Climate Variability . Part I : Development of a 1961 – 90 Mean Monthly Terrestrial Climatology, *Journal of Climate*, *12*, 829–856, doi:10.1175/1520-0442(1999)012<0829:RTCSTC>2.0.CO;2, 1999.

NGRIP members, High-resolution record of Northern Hemisphere climate extending into the last interglacial period., *Nature*, *431*(7005), 147–51, doi:10.1038/nature02805, 2004.

Nikolova, I., Q. Yin, A. Berger, U. K. Singh, and M. P. Karami, The last interglacial (Eemian) climate simulated by LOVECLIM and CCSM3, *Climate of the Past*, *9*(4), 1789–1806, doi:10.5194/cp-9-1789-2013, 2013.

Noël, B., X. Fettweis, W. J. van de Berg, M. R. van den Broeke, and M. Erpicum, Sensitivity of Greenland Ice Sheet surface mass balance to perturbations in sea surface temperature and sea ice cover: a study with the regional climate model MAR, *The Cryosphere*, *8*(5), 1871–1883, doi:10.5194/tc-8-1871-2014, 2014.

Nørgaard-Pedersen, N., N. Mikkelsen, S. J. Lassen, Y. Kristoffersen, and E. Sheldon, Reduced sea ice concentrations in the Arctic Ocean during the last interglacial period revealed by sediment cores off northern Greenland, *Paleoceanography*, *22*(1), 1–15, doi:10.1029/2006PA001283, 2007.

Ohmura, A., and N. Reeh, New precipitation and accumulation maps for Greenland, *Journal of Glaciology*, *37*(125), 140–148, 1991.

Otterå, O. H., and H. Drange, Effects of solar irradiance forcing on the ocean circulation and sea-ice in the North Atlantic in an isopycnic coordinate ocean general circulation model, *Tellus, Series A: Dynamic Meteorology and Oceanography*, *56*(2), 154–166, doi:10.1111/j.1600-0870.2004.00046.x, 2004.

Otto-Bliesner, B. L., S. J. Marshall, J. T. Overpeck, G. H. Miller, and A. Hu, Simulating Arctic climate warmth and icefield retreat in the last interglaciation., *Science (New York, N.Y.)*, *311*(5768), 1751–1753, doi:10.1126/science.1120808, 2006.

Otto-Bliesner, B. L., N. Rosenbloom, E. J. Stone, N. P. McKay, D. J. Lunt, E. C. Brady, and J. T. Overpeck, How warm was the last interglacial? New model-data comparisons., *Philosophical transactions. Series A, Mathematical, physical, and engineering sciences*, *371*(2001), doi:10.1098/rsta.2013.0097, 2013.

Outten, S. D., and I. Esau, A link between Arctic sea ice and recent cooling trends over Eurasia, *Climatic Change*, *110*(3-4), 1069–1075, doi:10.1007/s10584-011-0334-z, 2012.

Overland, J., J. A. Francis, R. Hall, E. Hanna, S.-J. Kim, and T. Vihma, The Melting Arctic and Midlatitude Weather Patterns: Are They Connected?, *Journal of Climate*, *28*(20), 7917–7932, doi:10.1175/JCLI-D-14-00822.1, 2015.

Overland, J. E., and M. Wang, Large-scale atmospheric circulation changes are associated with the recent loss of Arctic sea ice, *Tellus A*, *62*(1), 1–9, doi:10.1111/j.1600-0870.2009.00421.x, 2010.

Overpeck, J. T., B. L. Otto-Bliesner, G. H. Miller, D. R. Muhs, R. B. Alley, and J. T. Kiehl, Paleoclimatic evidence for future ice-sheet instability and rapid sea-level rise., *Science (New York, N.Y.)*, *311*(5768), 1747–50, doi:10.1126/science.1115159, 2006.

Pedersen, R. A., I. Cvijanovic, P. L. Langen, and B. M. Vinther, The Impact of Regional Arctic Sea Ice Loss on Atmospheric Circulation and the NAO, *Journal of Climate*, *29*(2), 889–902, doi:10.1175/JCLI-D-15-0315.1, 2016a.

Pedersen, R. A., P. L. Langen, and B. M. Vinther, The last interglacial climate – comparing direct and indirect impacts of insolation changes, *In review, Climate Dynamics*, 2016b.

Pedersen, R. A., P. L. Langen, and B. M. Vinther, Greenland warming during the last interglacial: the relative importance of insolation and oceanic changes, *Climate of the Past Discussions*, pp. 1–20, doi:10.5194/cp-2016-48, 2016c.

Peings, Y., and G. Magnusdottir, Response of the Wintertime Northern Hemisphere Atmospheric Circulation to Current and Projected Arctic Sea Ice Decline: A Numerical Study with CAM5, *Journal of Climate*, *27*(1), 244–264, doi:10.1175/JCLI-D-13-00272.1, 2014.

Peixóto, J. P., and A. H. Oort, Physics of climate, *Reviews of Modern Physics*, *56*(3), 1984.

Perovich, D. K., T. C. Grenfell, B. Light, and P. V. Hobbs, Seasonal evolution of the albedo of multiyear Arctic sea ice, *Journal of Geophysical Research*, *107*(C10), 8044, doi:10.1029/2000JC000438, 2002.

Persson, A., P. L. Langen, P. D. Ditlevsen, and B. M. Vinther, The influence of precipitation weighting on interannual variability of stable water isotopes in Greenland, *Journal of Geophysical Research: Atmospheres*, *116*(20), 1–13, doi:10.1029/2010JD015517, 2011.

Petersen, G. N., J. E. Kristjánsson, and H. Ólafsson, Numerical simulations of Greenland's impact on the Northern Hemisphere winter circulation, *Tellus, Series A: Dynamic Meteorology and Oceanography*, *56*(2), 102–111, doi:10.1111/j.1600-0870.2004.00047.x, 2004.

Peterson, K. A., J. Lu, and R. J. Greatbatch, Evidence of nonlinear dynamics in the eastward shift of the NAO, *Geophysical Research Letters*, *30*(2), 2–5, doi:10.1029/2002GL015585, 2003.

Petit, J. R., et al., Climate and atmospheric history of the past 420,000 years from the Vostok ice core, Antarctica, *Nature*, *399*(6735), 429–436, doi:10.1038/20859, 1999.

Petoukhov, V., and V. A. Semenov, A link between reduced Barents-Kara sea ice and cold winter extremes over northern continents, *Journal of Geophysical Research*, *115*(D21), D21,111, doi:10.1029/2009JD013568, 2010.

PMIP3, Last Interglacial Experimental Design, `https://wiki.lsce.ipsl.fr/pmip3/doku.php/pmip3:design:li:final`, accessed: 2016-01-08, 2010.

Polyakov, I. V., J. E. Walsh, and R. Kwok, Recent changes of Arctic multiyear sea ice coverage and the likely causes, *Bulletin of the American Meteorological Society*, *93*(2), 145–151, doi:10.1175/BAMS-D-11-00070.1, 2012.

Polyakov, I. V., et al., Arctic Ocean Warming Contributes to Reduced Polar Ice Cap, *Journal of Physical Oceanography*, *40*(12), 2743–2756, doi:10.1175/2010JPO4339.1, 2010.

Quiquet, A., C. Ritz, H. J. Punge, and D. Salas y Mélia, Greenland ice sheet contribution to sea level rise during the last interglacial period: a modelling study driven and constrained by ice core data, *Climate of the Past*, *9*(1), 353–366, doi:10.5194/cp-9-353-2013, 2013.

Rasmussen, T. L., D. W. Oppo, E. Thomsen, and S. J. Lehman, Deep sea records from the southeast Labrador Sea: Ocean circulation changes and ice-rafting events during the last 160,000 years, *Paleoceanography*, *18*(1), doi:10.1029/2001PA000736, 2003.

Rayner, N. A., D. E. Parker, E. B. Horton, C. K. Folland, L. V. Alexander, D. P. Rowell, E. C. Kent, and A. Kaplan, Global analyses of sea surface temperature, sea ice, and night marine air temperature since the late nineteenth century, *Journal of Geophysical Research*, *108*(D14), doi:10.1029/2002JD002670, 2003.

Rinke, A., K. Dethloff, W. Dorn, D. Handorf, and J. C. Moore, Simulated Arctic atmospheric feedbacks associated with late summer sea ice anomalies, *Journal of Geophysical Research: Atmospheres*, *118*(14), 7698–7714, doi:10.1002/jgrd.50584, 2013.

Robinson, A., R. Calov, and A. Ganopolski, Greenland ice sheet model parameters constrained using simulations of the Eemian Interglacial, *Climate of the Past*, *7*(2), 381–396, doi:10.5194/cp-7-381-2011, 2011.

Rossignol-Strick, M., Mediterranean Quaternary sapropels, an immediate response of the African monsoon to variation of insolation, *Palaeogeography, Palaeoclimatology, Palaeoecology*, *49*(3-4), 237–263, doi:10.1016/0031-0182(85)90056-2, 1985.

Schuenemann, K. C., J. J. Cassano, and J. Finnis, Synoptic Forcing of Precipitation over Greenland: Climatology for 1961–99, *Journal of Hydrometeorology*, *10*(1), 60–78, doi:10.1175/2008JHM1014.1, 2009.

Schurgers, G., U. Mikolajewicz, M. Gröger, E. Maier-Reimer, M. Vizcaíno, and A. M. E. Winguth, The effect of land surface changes on Eemian climate, *Climate Dynamics*, *29*(4), 357–373, doi:10.1007/s00382-007-0237-x, 2007.

Screen, J. A., and I. Simmonds, Increasing fall-winter energy loss from the Arctic Ocean and its role in Arctic temperature amplification, *Geophysical Research Letters*, *37*(16), doi:10.1029/2010GL044136, 2010a.

Screen, J. A., and I. Simmonds, The central role of diminishing sea ice in recent Arctic temperature amplification, *Nature*, *464*(7293), 1334–1337, doi:10.1038/nature09051, 2010b.

Screen, J. A., and I. Simmonds, Exploring links between Arctic amplification and mid-latitude weather, *Geophysical Research Letters*, *40*(January), 959–964, doi:10.1002/GRL.50174, 2013.

Screen, J. A., and I. Simmonds, Amplified mid-latitude planetary waves favour particular regional weather extremes, *Nature Climate Change*, *4*(8), 704–709, doi:10.1038/nclimate2271, 2014.

Screen, J. A., C. Deser, and I. Simmonds, Local and remote controls on observed Arctic warming, *Geophysical Research Letters*, *39*(10), doi:10.1029/2012GL051598, 2012.

Screen, J. A., I. Simmonds, C. Deser, and R. Tomas, The Atmospheric Response to Three Decades of Observed Arctic Sea Ice Loss, *Journal of Climate*, *26*(4), 1230–1248, doi:10.1175/JCLI-D-12-00063.1, 2013.

Screen, J. A., C. Deser, and L. Sun, Projected changes in regional climate extremes arising from Arctic sea ice loss, *Environmental Research Letters*, *10*(8), 084,006, doi:10.1088/1748-9326/10/8/084006, 2015.

Seierstad, I. A., and J. Bader, Impact of a projected future Arctic Sea Ice reduction on extratropical storminess and the NAO, *Climate Dynamics*, *33*(7-8), 937–943, doi:10.1007/s00382-008-0463-x, 2008.

Serreze, M. C., and R. G. Barry, *The Arctic Climate System*, 385 pp., Cambridge University Press, 2005.

Serreze, M. C., and R. G. Barry, Processes and impacts of Arctic amplification: A research synthesis, *Global and Planetary Change*, *77*(1-2), 85–96, doi:10.1016/j.gloplacha.2011.03.004, 2011.

Serreze, M. C., R. C. Schnell, and J. D. Kahl, Low-level temperature inversions of the Eurasian Arctic and comparisons with Soviet drifting station data, *Journal of Climate*, 1992.

Serreze, M. C., A. P. Barrett, J. C. Stroeve, D. N. Kindig, and M. M. Holland, The emergence of surface-based Arctic amplification, *The Cryosphere*, *3*(1), 11–19, 2009.

Serreze, M. C., A. P. Barrett, and J. J. Cassano, Circulation and surface controls on the lower tropospheric air temperature field of the Arctic, *Journal of Geophysical Research*, *116*(D7), D07,104, doi:10.1029/2010JD015127, 2011.

Serreze, M. C., et al., The large-scale freshwater cycle of the Arctic, *Journal of Geophysical Research*, *111*(C11010), doi:10.1029/2005JC003424, 2006.

Sewall, J. O., Precipitation Shifts over Western North America as a Result of Declining Arctic Sea Ice Cover: The Coupled System Response, *Earth Interactions*, *9*(26), 1–23, doi:10.1175/EI171.1, 2005.

Shindell, D., and G. Faluvegi, Climate response to regional radiative forcing during the twentieth century, *Nature Geoscience*, *2*(4), 294–300, doi:10.1038/ngeo473, 2009.

Sime, L. C., E. W. Wolff, K. I. C. Oliver, and J. C. Tindall, Evidence for warmer interglacials in East Antarctic ice cores, *Nature*, *462*(7271), 342–345, doi:10.1038/nature08564, 2009.

Sime, L. C., C. Risi, J. C. Tindall, J. Sjolte, E. W. Wolff, V. Masson-Delmotte, and E. Capron, Warm climate isotopic simulations: what do we learn about interglacial signals in Greenland ice cores?, *Quaternary Science Reviews*, *67*, 59–80, doi:10.1016/j.quascirev.2013.01.009, 2013.

Smith, R., et al., The Parallel Ocean Program (POP) reference manual: Ocean component of the Community Climate System Model (CCSM) and Community Earth System Model (CESM), *Tech. rep.*, 2010.

Solignac, S., A. De Vernal, and C. Hillaire-Marcel, Holocene sea-surface conditions in the North Atlantic - Contrasted trends and regimes in the western and eastern sectors (Labrador Sea vs. Iceland Basin), *Quaternary Science Reviews*, *23*(3-4), 319–334, doi:10.1016/j.quascirev.2003.06.003, 2004.

Steen-Larsen, H. C., et al., Understanding the climatic signal in the water stable isotope records from the NEEM shallow firn/ice cores in northwest Greenland, *Journal of Geophysical Research Atmospheres*, *116*(6), 1–20, doi:10.1029/2010JD014311, 2011.

Steffen, K., and J. Box, Surface climatology of the Greenland Ice Sheet: Greenland Climate Network 1995-1999, *Journal of Geophysical Research: Atmospheres*, *106*(D24), 33,951–33,964, doi:10.1029/2001JD900161, 2001.

Steig, E. J., P. M. Grootes, and M. Stuiver, Seasonal Precipitation Timing and Ice Core Records, *Science*, *266*(5192), 1885–1886, doi:10.1126/science.266.5192.1885, 1994.

Stenni, B., et al., The deuterium excess records of EPICA Dome C and Dronning Maud Land ice cores (East Antarctica), *Quaternary Science Reviews*, *29*(1-2), 146–159, doi:10.1016/j.quascirev.2009.10.009, 2010.

Sterl, A., et al., A look at the ocean in the EC-Earth climate model, *Climate Dynamics*, *39*(11), 2631–2657, doi:10.1007/s00382-011-1239-2, 2012.

Stommel, H. M., Thermohaline Convection with Two Stable Regimes of Flow, *Tellus*, *13*(2), 224–230, doi:10.1111/j.2153-3490.1961.tb00079.x, 1961.

Stone, E. J., D. J. Lunt, J. D. Annan, and J. C. Hargreaves, Quantification of the Greenland ice sheet contribution to Last Interglacial sea level rise, *Climate of the Past*, *9*(2), 621–639, doi:10.5194/cp-9-621-2013, 2013.

Stouffer, R. J., et al., Investigating the Causes of the Response of the Thermohaline Circulation to Past and Future Climate Changes, *Journal of Climate*, *19*(8), 1365–1387, doi:10.1175/JCLI3689.1, 2006.

Stroeve, J. C., V. M. Kattsov, A. P. Barrett, M. C. Serreze, T. Pavlova, M. M. Holland, and W. N. Meier, Trends in Arctic sea ice extent from CMIP5, CMIP3 and observations, *Geophysical Research Letters*, *39*(16), doi:10.1029/2012GL052676, 2012a.

Stroeve, J. C., M. C. Serreze, M. M. Holland, J. E. Kay, J. Malanik, and A. P. Barrett, The Arctic's rapidly shrinking sea ice cover: a research synthesis, *Climatic Change*, *110*(3-4), 1005–1027, doi:10.1007/s10584-011-0101-1, 2012b.

Stroeve, J. C., A. P. Barrett, M. C. Serreze, and A. Schweiger, Using records from submarine, aircraft and satellites to evaluate climate model simulations of Arctic sea ice thickness, *Cryosphere*, *8*(5), 1839–1854, doi:10.5194/tc-8-1839-2014, 2014.

Strong, C., and G. Magnusdottir, Dependence of NAO variability on coupling with sea ice, *Climate Dynamics*, *36*(9-10), 1681–1689, doi:10.1007/s00382-010-0752-z, 2010.

Swann, A. L., I. Y. Fung, S. Levis, G. B. Bonan, and S. C. Doney, Changes in Arctic vegetation amplify high-latitude warming through the greenhouse effect, *Proceedings of the National Academy of Sciences*, *107*(4), 1295–1300, doi:10.1073/pnas.0913846107, 2010.

Swingedouw, D., J. Mignot, P. Braconnot, E. Mosquet, M. Kageyama, and R. Alkama, Impact of Freshwater Release in the North Atlantic under Different Climate Conditions in an OAGCM, *Journal of Climate*, *22*(23), 6377–6403, doi:10.1175/2009JCLI3028.1, 2009.

Swingedouw, D., C. B. Rodehacke, E. Behrens, M. Menary, S. M. Olsen, Y. Gao, U. Mikolajewicz, J. Mignot, and A. Biastoch, Decadal fingerprints of freshwater discharge around Greenland in a multi-model ensemble, *Climate Dynamics*, *41*(3-4), 695–720, doi:10.1007/s00382-012-1479-9, 2013.

Tang, Q., X. Zhang, X. Yang, and J. A. Francis, Cold winter extremes in northern continents linked to Arctic sea ice loss, *Environmental Research Letters*, *8*(1), doi:10.1088/1748-9326/8/1/014036, 2013.

Tuenter, E., S. L. Weber, F. J. Hilgen, and L. J. Lourens, Sea-ice feedbacks on the climatic response to precession and obliquity forcing, *Geophysical Research Letters*, *32*(24), doi:10.1029/2005GL024122, 2005.

Turney, C. S. M., and R. T. Jones, Does the Agulhas Current amplify global temperatures during super-interglacials?, *Journal of Quaternary Science*, *25*(6), 839–843, doi:10.1002/jqs.1423, 2010.

Tzedakis, P. C., D. Raynaud, J. F. McManus, A. Berger, V. Brovkin, and T. Kiefer, Interglacial diversity, *Nature Geoscience*, *2*(11), 751–755, doi:10.1038/ngeo660, 2009.

Ulbrich, U., and M. Christoph, A shift of the NAO and increasing storm track activity over Europe due to anthropogenic greenhouse gas forcing, *Climate Dynamics*, *15*, 551–559, doi:10.1007/s003820050299, 1999.

van As, D., et al., Darkening of the Greenland ice sheet due to the meltalbedo feedback observed at PROMICE weather stations, *Geological Survey of Denmark and Greenland Bulletin*, (28), 69–72, 2013.

van de Berg, W. J., M. R. van den Broeke, J. Ettema, E. van Meijgaard, and F. Kaspar, Significant contribution of insolation to Eemian melting of the Greenland ice sheet, *Nature Geoscience*, *4*(10), 679–683, doi:10.1038/ngeo1245, 2011.

van den Broeke, M. R., C. J. P. P. Smeets, and R. S. W. van de Wal, The seasonal cycle and interannual variability of surface energy balance and melt in the ablation zone of the west Greenland ice sheet, *The Cryosphere*, *5*(2), 377–390, doi:10.5194/tc-5-377-2011, 2011.

Vancoppenolle, M., T. Fichefet, H. Goosse, S. Bouillon, G. Madec, and M. A. M. Maqueda, Simulating the mass balance and salinity of Arctic and Antarctic sea ice. 1. Model description and validation, *Ocean Modelling*, *27*(1-2), 33–53, doi:10.1016/j.ocemod.2008.10.005, 2009.

Vaughan, D. G., et al., Observations: Cryosphere, in *Climate Change 2013: The Physical Science Basis. Contribution of Working Group I to the Fifth Assessment Report of the Intergovernmental Panel on Climate Change*, edited by T. F. Stocker, D. Qin, G.-K. Plattner, M. Tignor, S. K. Allen, J. Boschung, A. Nauels, Y. Xia, V. Bex, and P. M. Midgley, chap. 4, Cambridge University Press, Cambridge, United Kingdom and New York, NY, USA, 2013.

Vavrus, S. J., D. Waliser, A. Schweiger, and J. A. Francis, Simulations of 20th and 21st century Arctic cloud amount in the global climate models assessed in the IPCC AR4, *Climate Dynamics*, *33*(7-8), 1099–1115, doi:10.1007/s00382-008-0475-6, 2008.

Velichko, A. A., O. K. Borisova, and E. M. Zelikson, Paradoxes of the Last Interglacial climate: Reconstruction of the northern Eurasia climate based on palaeofloristic data, *Boreas*, *37*(1), 1–19, doi:10.1111/j.1502-3885.2007.00001.x, 2008.

Vihma, T., Effects of Arctic Sea Ice Decline on Weather and Climate: A Review, *Surveys in Geophysics*, *35*(5), 1175–1214, doi:10.1007/s10712-014-9284-0, 2014.

Vinther, B. M., et al., Holocene thinning of the Greenland ice sheet, *Nature*, *461*(7262), 385–8, doi:10.1038/nature08355, 2009.

Vionnet, V., E. Brun, S. Morin, A. Boone, S. Faroux, P. Le Moigne, E. Martin, and J.-M. Willemet, The detailed snowpack scheme Crocus and its implementation in SURFEX v7.2, *Geoscientific Model Development*, *5*(3), 773–791, doi:10.5194/gmd-5-773-2012, 2012.

von Storch, H., and F. W. Zwiers, *Statistical Analysis in Climate Research*, Cambridge University Press, Cambridge, United Kingdom and New York, NY, USA, 2001.

Wallace, J. M., I. M. Held, D. W. J. Thompson, K. E. Trenberth, and J. E. Walsh, Global Warming and Winter Weather, *Science*, *343*(February), 729–730, 2014.

Wang, Y.-H., G. Magnusdottir, H. Stern, X. Tian, and Y. Yu, Uncertainty Estimates of the EOF-Derived North Atlantic Oscillation, *Journal of Climate*, *27*(3), 1290–1301, doi:10.1175/JCLI-D-13-00230.1, 2014.

Wanner, H., S. Brönnimann, C. Casty, D. Gyalistras, J. Luterbacher, C. Schmutz, D. B. Stephenson, and E. Xoplaki, North Atlantic Oscillation - concepts and studies, *Surveys in Geophysics*, *22*(1984), 321–381, 2001.

Warren, S. G., Optical Properties of Snow, *Reviews of Geophysics and Space Physics*, *20*(1), 67–89, 1982.

Weertman, J., Milankovitch solar radiation variations and ice age ice sheet sizes, *Nature*, *261*, 17–20, 1976.

Willerslev, E., et al., Ancient biomolecules from deep ice cores reveal a forested southern Greenland., *Science*, *317*(5834), 111–114, doi:10.1126/science.1141758, 2007.

Winsor, K., A. E. Carlson, G. P. Klinkhammer, J. S. Stoner, and R. G. Hatfield, Evolution of the northeast Labrador Sea during the last interglaciation, *Geochemistry, Geophysics, Geosystems*, *13*(11), doi:10.1029/2012GC004263, 2012.

Yang, S., and J. H. Christensen, Arctic sea ice reduction and European cold winters in CMIP5 climate change experiments, *Geophysical Research Letters*, *39*(20), doi:10.1029/2012GL053338, 2012.

Yin, Q. Z., and A. Berger, Individual contribution of insolation and CO2 to the interglacial climates of the past 800,000 years, *Climate Dynamics*, *38*(3-4), 709–724, doi:10.1007/s00382-011-1013-5, 2012.

Zhang, Q., Implementing the orbital forcing in IFS (EC-Earth 3), *Tech. rep.*, Stockholm University, 2013.

Zhang, Y., D. J. Seidel, J.-C. Golaz, C. Deser, and R. A. Tomas, Climatological Characteristics of Arctic and Antarctic Surface-Based Inversions, *Journal of Climate*, *24*(19), 5167–5186, doi:10.1175/2011JCLI4004.1, 2011.

Zuo, Z., and J. Oerlemans, Modelling albedo and specific balance of the Greenland ice sheet: calculations for the Søndre Strømfjord transect, *Journal of Glaciology*, *42*(141), 305–317, 1996.

List of Abbreviations

AGCM	Atmospheric General Circulation Model (atmosphere-only)
AMOC	Atlantic Meridional Overturning Circulation
ARC	CESM simulation with Arctic-wide sea ice reduction
ARC+CO2	CESM simulation with Arctic-wide sea ice reduction and CO_2 doubling
ATL	CESM simulation with sea ice reduction in the Atlantic sector
CESM	Community Earth System Model (National Center for Atmospheric Research)
CO2	CESM simulation with pre-industrial (CTRL) sea ice and CO_2 doubling
CTRL	CESM control simulation with pre-industrial sea ice conditions
DJF	December-January-February (i.e. winter)
dNEEM	Depositional site for the Eemian ice in the NEEM ice core
DOM	Data Ocean Model
DSE	Dry Static Energy (Atmospheric heat transport)
EMIC	Earth-System Models of Intermediate Complexity
EOF	Empirical Orthogonal Function
GCM	General Circulation Model
GHG	Greenhouse Gas
GrIS	The Greenland ice sheet
IFS	Integrated Forecasting Model, atmospheric component of EC-Earth
iL+oL	EC-Earth AGCM simulation with Eemian insolation and sea surface conditions
iL+oP	EC-Earth AGCM simulation with Eemian insolation and pre-industrial sea surface conditions
iP+oL	EC-Earth AGCM simulation with pre-industrial insolation and Eemian sea surface conditions

iP+oP	EC-Earth AGCM control simulation with pre-industrial insolation and sea surface conditions
iP+oP-ice	EC-Earth AGCM control simulation with pre-industrial insolation and sea surface temperatures combined with Eemian sea ice conditions
JJA	June-July-August (i.e. summer)
LIG	EC-Earth Last Interglacial (Eemian) simulation
LIM	Louvain-la-Neuve Sea Ice Model, sea ice model in EC-Earth
MAM	March-April-May (i.e. spring)
MHT	(Atmospheric) Meridional Heat Transport
NAO	North Atlantic Oscillation
NEEM	North Greenland Eemian Ice Drilling (*NEEM community members*, 2013)
NEMO	Ocean model component of EC-Earth
PAC	CESM simulation with sea ice reduction in the Pacific sector
PI	EC-Earth pre-industrial control climate simulation
SFC	Surface
SIC	Sea ice concentration
SMB	Surface Mass Balance
SOM	Slab Ocean Model
SON	September-October-November (i.e. autumn/fall)
SSS	Sea Surface Salinity
SST	Sea Surface Temperature
TEKE	Transient Eddy Kinetic Energy
TOA	Top of the atmosphere

List of Tables

List of Figures